Energy in Earth's Magnetosphere

by

Austin Brenner

A dissertation submitted in partial fulfillment
of the requirements for the degree of
Doctor of Philosophy
(Aerospace Engineering)
in The University of Michigan
2023

Doctoral Committee:

Professor Tuija Pulkkinen, Co-Chair
Professor Tamas I. Gombosi, Co-Chair
Professor Ken Powell
Dr. David Sibeck, NASA Goddard Space Flight Center

Austin Brenner

aubr@umich.edu

ORCID iD: 0000-0002-2059-354X

ACKNOWLEDGEMENTS

This PhD journey would not have been possible without the incredible mentorship and professional guidance through these last 5 years from my advisor Tuija. I'm extremely grateful for the support and opportunities that you provided. Thank you to my committee members Tuija Pulkkinen, Tamas Gombosi, Ken Powell, and David Sibeck for your continued attention to this work and valuable feedback in the yearly meetings along the way. Special thank you to Tamas for helping a lost grad student, trying to figure out what to do after leaving his research lab. I am so thankful for finding a new home in the CLaSP department and the GEM community and this would not have happened without your good will.

I'm extremely fortunate to benefit from the decades of research put into the space plasma simulation tools included in the Space Weather Modeling Framework. Thank you to all those past, present, and future, that enable fantastic research by developing and sharing these valuable research tool.

Huge thanks to the Dream Team. Qusai, your mentorship was invaluable; I will continue to spread the good word of VIM and will never forget: "don't mess up". Shannon, thank you for struggling with me in the Tecplot trenches and inspiring productive and challenging conversations inside and outside the office. And of course thank you to Matti and Sanjay for your encouragement and big smiles every day regardless of the circumstances. Connor and Vivian, you're both going to do great! Keep the morale in check and remember that you're surrounded by peers and mentors that can help you out, all you need to do is ask.

Big thanks to everyone in the MITHRAS group meetings throughout the years. I really enjoyed getting to share news (sticker-worthy or otherwise) and eat treats while discussing everything from ionospheric conductance to types of cookies.

Thank you to my partner Leanne and our sweet, fluffy, friendly, and gregarious cat Pudge, you both made our house and Ann Arbor feel like home. Your emotional support has been vital throughout the many ups and downs of grad school. I can wholeheartedly say that the last 5 years have been some of the best moments of my life, and that's a huge part because of you and my friends. Whether it was studying for quals a million years ago with the Keeners, having a porch sit with Thomas, waiting for wort to chill with Tom, having family dinner and watching cursed TV with the whole Beakes crew, catching up with a drink at Bill's, or hosting a party with everyone to all get together, it was always a good time thank you all. And finally, thank you to my family for your unwavering support.

TABLE OF CONTENTS

LIST OF FIGURES

Figure

LIST OF TABLES

Table

ABSTRACT

The space environment dominated by Earth's magnetic field is the magnetosphere; this environment is carved from the surrounding solar wind, but under the right conditions the solar wind is able to directly interact with the planet. When this occurs, energy enters the magnetosphere system, which results in magnetic perturbations that can be hazardous for large infrastructure on the planet's surface. This dissertation focuses on the large scale energy coupling processes between the solar wind and magnetosphere by using simulation tools. The first chapter provides motivation, introduction, and background, with brief history of magnetopsheric research. The second chapter outlines in detail the development of the methodology that is used throughout the rest of the work. The new magnetopause surface identification uses a state variable of magnetic topology combined with the plasma β^* variable (representing the ratio of thermal and kinetic to magnetic pressure). These two variables combine to feed an isosurface detection algorithm which swiftly and consistently identifies the magnetopause surface, with superior coverage of the magnetosphere cusps compared with other methods. Chapters 3 is an analysis of a real storm event focusing first on energy transport at the magnetopause. The real event of February 2014 is analyzed, first with observations and empirical models, then with the new magnetopause detection of simulation output. It is found that the energy transport at the magnetopause is a balance of magnetic energy injection through the open topology lobes, and energy escape of thermal and kinetic energy through the closed topology region of the magnetopause. Additionally, it was determined that the magnetopause surface motion contributes significantly to net energy transport. Chapter 4 is a second real

event study in which the magnetosphere is dissected, defining internal magnetospheric boundaries according to magnetic topology. Similar to chapter 3, the event is studied using observation and energy transport analysis of simulation output. For this work the magnetopause and magnetosphere interior are split by magnetic topology and day/night magnetic mapping. Two energy circulation paths are found. Externally energy enters through the open topology lobes, and exits through the closed topology magnetopause. Internally a recirculating energy pathway is uncovered sending magnetic energy from the dayside closed region back through the cusp to the lobes where it joins the injected energy from the solar wind, heading toward the nightside closed region in the tail. The results of chapter 4 fully quantify the classic Dungey cycle in terms of magnetosphere energy transport at Earth. Chapter 5 shows the preliminary results from a parameter study using 96 cases of two hour steady solar wind conditions. Strong internal magnetosphere energy dynamics are found, as evident by the significant changes in the total energy content of the magnetosphere, despite the input conditions being steady. This internal energy change makes it challenging to attribute the classic input-output style solar wind magnetosphere coupling function relationship. Chapter 6 concludes with an overview of the findings and contributions and outlines ongoing and future work. The major contributions are 1. magnetopause detection algorithms and energy analysis techniques, 2. improved understanding of magnetopause energy transport for real storm conditions, 3. quantification of the Dungey cycle, and 4. illustration of the complexity and challenges associated with attributing input-output coupling functions.

CHAPTER I

Introduction and Background

1.1 Motivation

Outer space is dangerous and certainly not empty. The space environment around our planet is growing exponentially more important as we continue to send critical and expensive technology as well as an increasing number of human lives out into orbit, where they are exposed to the many perils of space.

The humans and technology existing above Earth's atmosphere are not exclusively at risk. Geomagnetic storms, which can rapidly perturb the planets magnetic field, can induce currents in any large, electrically conducting medium on the planets surface. Examples includes power infrastructure, deep sea cables, and even the ground itself depending on the local geological makeup. Because of this severe space weather has been identified as the only pan-national natural disaster along side global pandemic (*FEMA*, 2019).

A major challenge to this type of threat is the short time in which it develops; an eruption on the solar surface could launch energetic particles and a coronal mass ejection that could reach our planet in a matter minutes. In order to gauge the worst case scenario for an extreme space weather event we have to better understand how energy makes its way from the interplanetary space environment into our planet's magnetosphere.

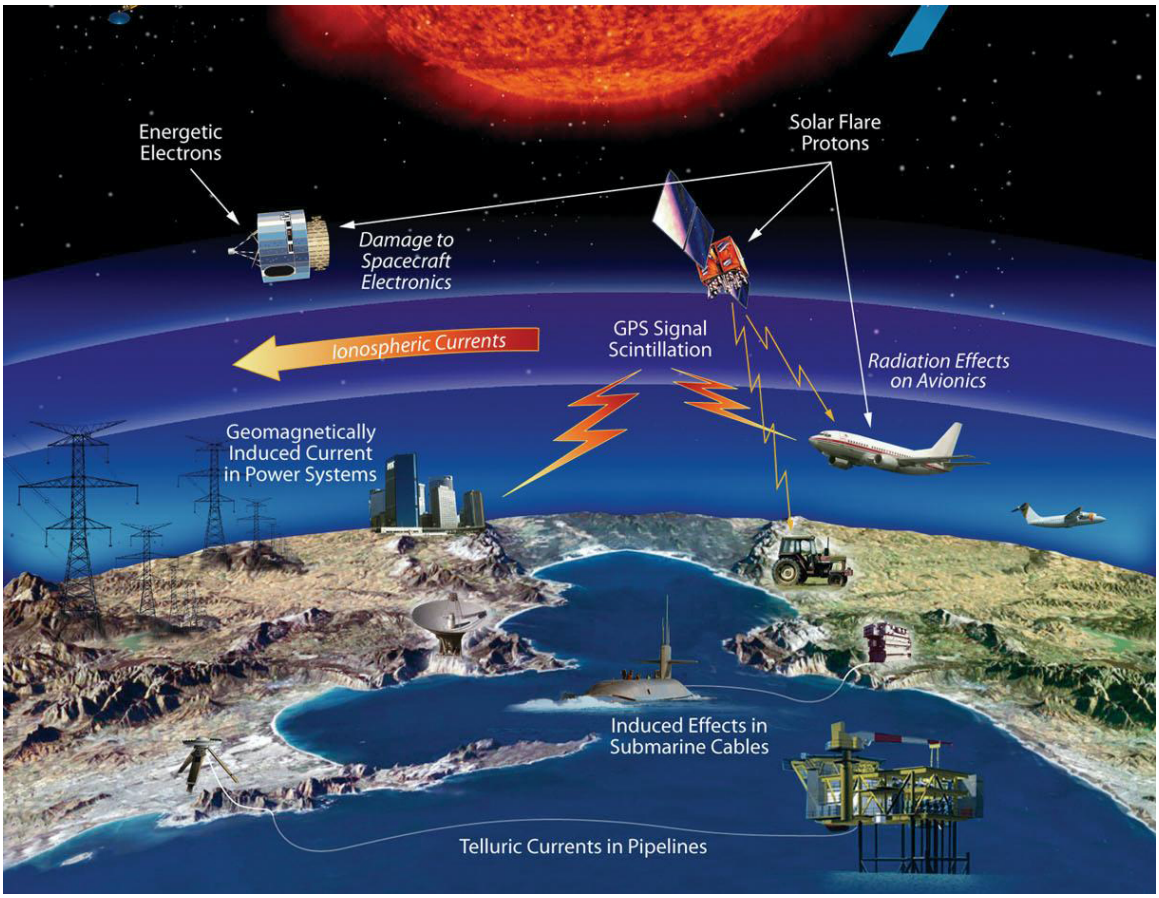

Figure 1.1: Diagram highlighting some of the major types of systems and infrastructure that can be affected by severe space weather. Credit: NASA

If we can better quantify and explain how energy couples into the magnetosphere then we can understand what scenarios would be most dangerous and what kinds of thresholds necessitate a full blown emergency response. In this thesis I seek to develop the tools and answer some fundamental questions about the relationship between the driving solar wind conditions and the amount of energy that enters and moves through Earth's space environment.

1.2 Space Physics and Storm Dynamics

1.2.1 Plasma Regimes

1.2.1.1 What is a Plasma?

Plasma is sometimes referred to as the fourth state of matter, and can be thought of as a gas that responds to electric and magnetic fields. Consider a simple gas as a collection of particles that are moving in random directions with some velocity, and experience collisions like billiard balls colliding into each other on a pool table. The temperature of this gas represents the collective random motion of the gas and as the collisions occur they redistribute momentum and energy until the system is in an equilibrium state known as Local Thermodynamic Equilibrium (LTE).

A plasma is formed when enough of the particles in the gas are charged, in order for the particles to become charged they undergo an ionization reaction. Continuing with the billiard ball example, when a collision between particles is violent enough the particles can undergo a chemical reaction by which an outer valence electron is stripped from the neutral particle. This type of reaction is called an ionization reaction and takes energy out of the random thermal motion of the gas in exchange for creating a positively charged ion and a negatively charged electron.

Once a sufficient number of particles are charged the gas (now plasma) experiences forces from electric and magnetic fields that are externally applied as well as those

within from the motion of charged particles. The external fields exert the Lorentz force on each particle $q(\mathbf{E} + \mathbf{u} \times \mathbf{B})$ where q is the particle charge, $\mathbf{E}$ is the electric field, $\mathbf{u}$ is the particle velocity, and $\mathbf{B}$ is the magnetic field. External electric and magnetic fields can cause the particles to drift together, or for ions and electrons to drift separately.

Internally the charged particles experience the electric and magnetic forces from themselves, which act similarly to the simple gas collisions, but with more collective behavior. Unlike a simple collision, which mostly involves two particles at a time, the internal self generated electric and magnetic fields within a plasma involve many particles because the electromagnetic fields radiate information at the speed of light in all directions, faster than the random motion of the particles. In the same way that collisions in a gas led to LTE, the charged particles in plasma will self orient to minimize the internal electromagnetic forces such that the fields are screened out at a certain distance from a given particle. This distance is known as the Debye length, and depends on properties of the plasma. Because of this screening of fields, for lengths of interest beyond the Debye length the plasma can be considered quasi-neutral, meaning there is no net charge density.

The most important thing that defines a plasma is the presence of charged particles, which fundamentally changes its relationship to electromagnetic fields. In space, plasma is the most abundant form of matter.

1.2.1.2 The MagnetoHydroDynamic Limit

I will now provide a brief introduction to an important limiting case for plasma known as the Magnetohydrodynamic (MHD) limit.

To describe the behavior of a plasma, we could track each particle individually. This becomes intractable quite quickly, for the space environment around Earth there could easily be as many as 10^{33} particles, not considering the high density region near

the planets exobase and ionosphere!

Instead of describing each particle individually, we can represent all of the particles in a small neighborhood by the distribution of particles with different velocities. This distribution in velocity space, at a given point in physical space, and time yields a 7 dimensional system. From this distribution we can calculate the so called moments of the distribution to recover familiar macroscopic properties, such as density, bulk velocity, temperature, pressure, etc.

To describe this 7D system we can use the Boltzmann equation, given in equation 1.1. F is the distribution of particles in time, physical space $\mathbf{r}$, and velocity space $\mathbf{v}$; $\mathbf{a}$ is the acceleration that contains the various forces acting on the particles, and δF is a collision operator, which represents discrete changes in the particle distribution due to collisions or other effects.

$$\frac{\partial F(t,\mathbf{r},\mathbf{v})}{\partial t} + (\mathbf{v}\cdot\nabla)F(t,\mathbf{r},\mathbf{v}) + (\mathbf{a}\cdot\nabla_v)\,F(t,\mathbf{r},\mathbf{v}) = \frac{\delta F(t,\mathbf{r},\mathbf{v})}{\delta t} \tag{1.1}$$

The forces acting on the particles contain electromagnetic fields, so to describe those fields we need to include Maxwell's equations in combination with our Boltzmann equation. As you can see, we definitely would like to make some simplifying assumptions from here in order to make solving this equation a bit easier.

To get these equations to a simpler form, we first omit the collision operator. In Earth's space environment the time between particle collisions is many orders of magnitude higher than any other time scale of interest so we can safely assume our system is collisionless. There could be electromagnetic contributions to this operator as well, but we're going to ignore those too.

The next major assumption is that the particle distributions actually follow a fixed distribution in velocity space. In other words we enforce thermodynamic equilibrium on our system. Recall that the primary way that thermodynamic equilibrium

is achieved is through collisions, but in our system we don't have collisions so we are assuming our thermodynamic equilibrium was achieved elsewhere (in our case the solar surface and the ionosphere have much denser plasma, which do experience collisions, but let's not think about the LTE approximation too much right now). With these assumptions we now have distribution functions for each species, and this distribution is fixed in terms of local thermodynamic equilibrium.

Our last major assumption is to extend the quasi neutrality property of most plasma (no net charge outside of a sphere with radius of the Debye length) to fully treat the ions and electrons together as a single fluid. Fluid now referring to the point after we have taken the moments of the distribution function to obtain macroscopic properties. This has many important consequences as it prohibits electrons from fully separating from the ions. In the regular quasi-neutral case ions and electrons can counter-stream and remain entirely neutral. Like two trains passing each other, at any point in time and space the two trains are at the same linear position but are moving with opposite velocities. Lastly we blend in Maxwell's equations to achieve a version of Ohms law that combines both the fluid and electromagnetic effects. With all of these we have the single fluid MHD equations (equations 1.2-1.5). ρ_m is the mass density of the single fluid plasma simplified to be the ion mass density, $\mathbf{u}$ is the plasma bulk velocity, P is the thermal pressure, $\mathbf{g}$ is gravitational acceleration, $\mathbf{j}$ is the current density, $\bar{\sigma}$ is the electrical conductivity of the plasma, and $\mathbf{h}$ is the heat flow.

$$\frac{\partial \rho_m}{\partial t} + \nabla \cdot (\rho_m \mathbf{u}) = 0 \tag{1.2}$$

$$\rho_m \frac{\partial \mathbf{u}}{\partial t} + \rho_m (\mathbf{u} \cdot \nabla)\mathbf{u} + (\nabla \cdot P) - \rho_m \mathbf{g} - \rho \mathbf{E} - \mathbf{j} \times \mathbf{B} = \mathbf{0} \tag{1.3}$$

$$\frac{3}{2}\frac{\partial p}{\partial t} + \frac{3}{2}\nabla \cdot (p\mathbf{u}) + (P \cdot \nabla) \cdot \mathbf{u} + (\nabla \cdot \mathbf{h}) = (\mathbf{j} - \rho \mathbf{u}) \cdot (\mathbf{E} + \mathbf{u} \times \mathbf{B}) \tag{1.4}$$

$$\mathbf{j} = \bar{\sigma}_0(\mathbf{E} + \mathbf{u} \times \mathbf{B}) - \frac{\bar{\sigma}_0}{en_\mathrm{e}}\mathbf{j} \times \mathbf{B} + \frac{\bar{\sigma}_0}{en_\mathrm{e}}\nabla p_\mathrm{e} \tag{1.5}$$

$$\nabla \times \mathbf{E} = -\frac{\partial \mathbf{B}}{\partial t} \tag{1.6}$$

The single fluid MHD limit assumptions hold very well for most of the space environment around Earth, and the Ohms law in equation 1.5 can even be further simplified to achieve the ideal MHD equations. In the ideal limit the contributions from the electron pressure P_e are assumed to be negligible, and the plasma resistivity $\eta = \frac{1}{\bar{\sigma}\mu_0}$ is set to 0, in other words the plasma is treated as having infinite conductivity. The plasma resistivity η is also the diffusion coefficient of the magnetic field, so when it is set to 0, the magnetic field is then frozen into the plasma.

The ideal MHD limit is a great place to build your intuition around the plasma behavior in near Earth space, but there are crucial caveats for certain situations where the ideal MHD limit cannot be applied.

1.2.1.3 Non-MHD Effects

The most important condition where the ideal MHD limit fails is near reconnection zones, as sketched in figure 1.2. One of the primary assumptions was that the conductivity was infinite, and the magnetic diffusion was 0, but when anti-parallel magnetic fields are forced close together, the magnetic field strength drops significantly and the particles in the plasma can "forget" their magnetic origins and experience magnetic diffusion. This de-magnetization occurs first for the ions in a zone referred to as the ion diffusion region (IDR), and later for the electrons in a much smaller region known as the electron diffusion region (EDR).

Magnetic reconnection is able to alter the magnetic topology of a plasma and is responsible for much of the interaction that occurs between the solar wind and Earth's magnetosphere. This is why controlling magnetic diffusion and reconnection physics is important when simulating space plasma.

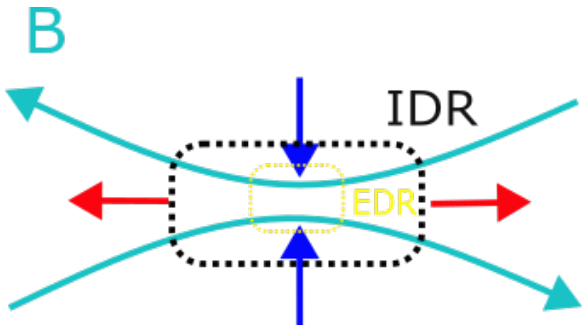

Figure 1.2: Diagram of magnetic reconnection in two dimensions. Cyan lines indicate magnetic field that is about to undergo reconnection. Blue arrows indicate low temperature plasma inflow and Red arrows indicate high temperature plasma outflow. IDR and EDR indicate the ion and electron diffusion regions where the species become unmagnetized.

Coincidentally, numerical ideal MHD models with no modifications contain a proxy for magnetic reconnection in the form of numerical diffusion. Numerical diffusion occurs in any finite volume numerical solution when higher than first order accuracy is desired. This is because in order to keep the solution stable by limiting the total variation (Total Variation Diminishing, TVD scheme) a limiter is applied that avoids creating new local extrema, but forces artificial diffusion to occur in order to maintain the conservation laws. When this artificial diffusion occurs in the magnetic field part of the solution it behaves exactly like the physical property of resistivity η.

Another condition where not even numerical ideal MHD can capture the physical phenomena is with counter-streaming species and ion populations. When a charge insensitive external force is applied perpendicular to the magnetic field that is frozen into the plasma, the ions and electrons are sent on drift paths in opposite directions. The plasma remains quasi-neutral, but there is net current density that develops proportional to the sum of the counter streaming drift velocities ($\mathbf{J} = \sum_{i^+,e^-} qn\mathbf{u}$, where q is the particle charge, n is the number density, and u is the particle velocity). This case cannot be treated consistently without allowing the ions and electrons to separate. Similarly, if two populations of ions (eg. oxygen and hydrogen, or even

cold hydrogen and hot hydrogen), each in LTE, move into the same physical space they will not automatically redistribute into a new LTE state, because the plasma is collisionless. These two populations can then counter-stream with two separate bulk velocities much like the ion-electron case.

1.2.2 Geomagnetic Storm and Substorm

1.2.2.1 Geomagnetic Storm

When there is a comprehensive disturbance to the Earth's dipole magnetic field, we describe it as a geomagnetic storm. During a storm the environment that Earth's dipole field dominates, known as the magnetosphere, becomes highly perturbed by allowing mass, momentum, and energy from the surrounding solar wind to enter the system. In addition, mass, momentum, and energy can be extracted from the planets atmosphere via a polar wind, which can further perturb the system.

Figure 1.3 shows a diagram of the magnetosphere with various current systems inside of it. Many of these current systems exists all the time due to the steady solar wind in interplanetary space, but during a storm the currents are enhanced leading to perturbations in Earth's dipole field.

The total magnetic perturbation at any point in space can be calculated using the Biot-Savart law (equation 6.5), and is proportional to the magnitude of the current perpendicular to the radial position vector and inversely proportional to the radial distance squared. This means currents that are closer to Earth like the ring current are experienced stronger, but changes to any of the current systems in the magnetosphere will cause magnetic perturbations.

In order to measure the strength of a storm, the magnetic perturbation is measured at the planets surface using magnetometers. Based the horizontal magnetic field readings from four magnetometer stations distributed in longitude which are near the magnetic equator, the deviation from the baseline magnetic field reading is averaged

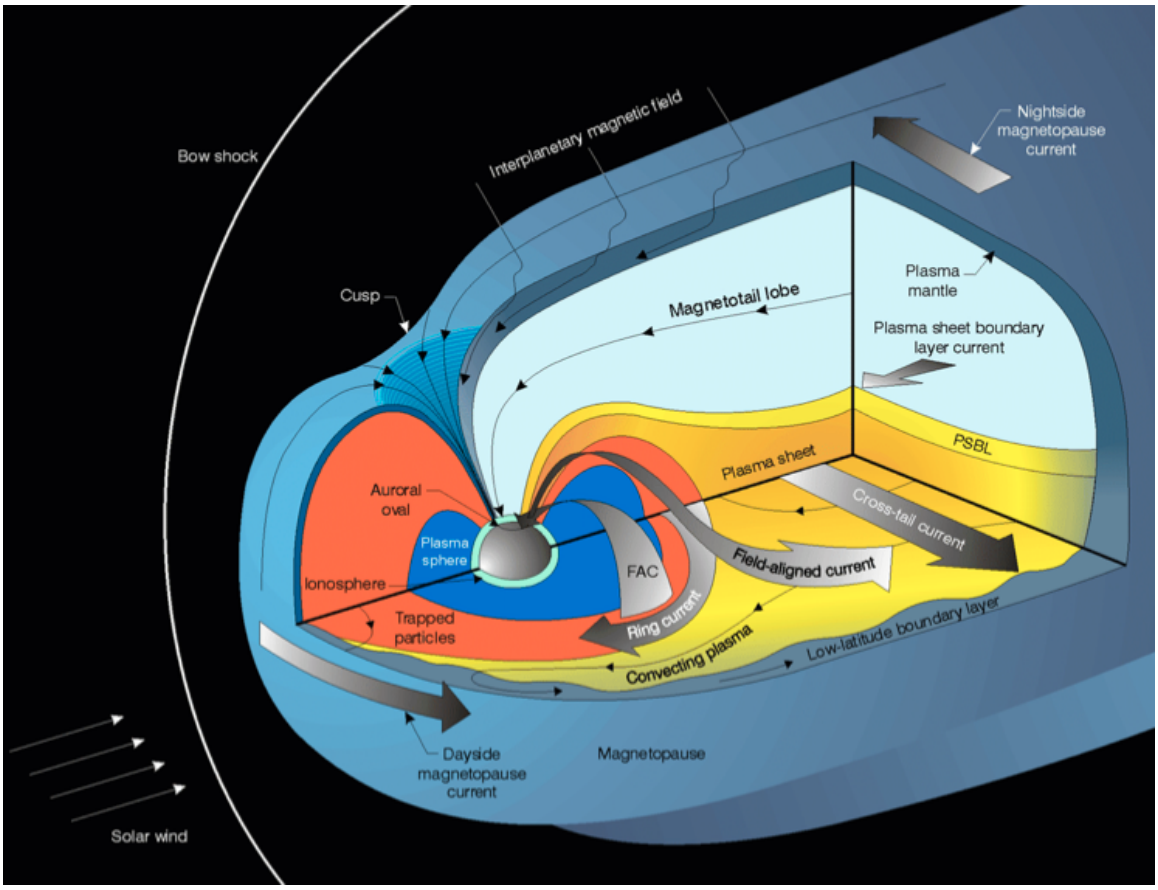

Figure 1.3: Diagram of major current systems in the magneotsphere, the Region 1 and Region 2 field aligned currents connect to the ionosphere. Sourced from *C.J. Pollock et al.*.

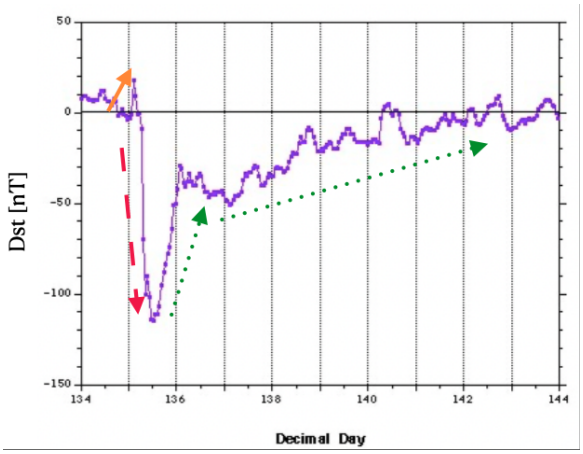

Figure 1.4: Disturbance storm time index (Dst) for a typical geomagnetic storm event. Arrows indicate the three storm phases: orange solid- sudden storm commencement, red dashed- storm main phase, and green dotted- storm recovery phase.

amongst the stations to produce a single value for the effective global perturbation to the dipole. This measure is known as the Disturbance STormtime index (Dst), and has been calculated continuously for several decades.

By looking at the time series of the Dst index, shown in figure 1.4, we can see the major phases of a geomagnetic storm. First is the sudden storm commencement, in which the magnetic perturbation is positive due to high pressure solar wind squeezing the magnetosphere and causing enhancements in the magnetopause current system.

Next is the storm main phase where plasma mass and energy enters the magnetosphere and becomes trapped, leading to the formation and enhancement of the ring current. This phase is marked by a sharp negative decrease in the recorded Dst index.

Lastly there is the recovery phase where the solar wind ceases to directly couple to the magnetosphere, but the internal mass and energy remains trapped. The Dst index for the recovery phase can remain depressed for days as the magnetic perturbation slowly returns to quiet level. There are two primary mechanisms for releasing the trapped plasma that makes up the ring current. The first is through wave particle interactions due to multiple particle populations coexisting in the same spatial region. These interactions scatter the ring current particles, causing them to loose

their perpendicular velocity which is what allows them to bounce between regions of high magnetic field strength. The second mechanism is through charge exchange collisions with the partially neutral atmosphere as the particles bounce toward the planet; this charge exchange yields energetic neutral particles and low energy ions, which do not return to the magnetosphere.

1.2.2.2 Geomagnetic Substorm

As the name suggests, there are also smaller scale events that occur in Earth's magnetosphere known as substorms. Substoms can be triggered by sudden solar wind changes, or by internal triggers but they always release magnetic energy in the tail of the magnetosphere and lead to field aligned currents and particle precipitation into the ionosphere.

The substorm phases can be observed by high latitude (above 60 degrees) magnetometer stations that measure local perturbations due to strong field aligned currents. Because of the field aligned currents come almost directly down to the ionosphere from above, the magnetic perturbation becomes much more localized so one station could measure a strong perturbation while another station measures almost nothing.

The primary field aligned current systems are known as the Region 1 and Region 2 current systems shown in figure 1.5. These current systems connect to the magnetopause currents and cross tail current and then follow the magnetic field, closing in the ionosphere. These field aligned currents are one of the primary ways the ionosphere and magnetosphere are coupled together.

The substorm begins with a growth phase, which builds excess magnetic energy in the magnetosphere lobes and thins the current sheet; this current sheet separates the two lobes. Once the substorm is triggered it is known as substorm onset; reconnection in the tail releases the excess magnetic energy, which begins the substorm expansion phase. In this expansion phase the auroral oval expands due to increased field aligned

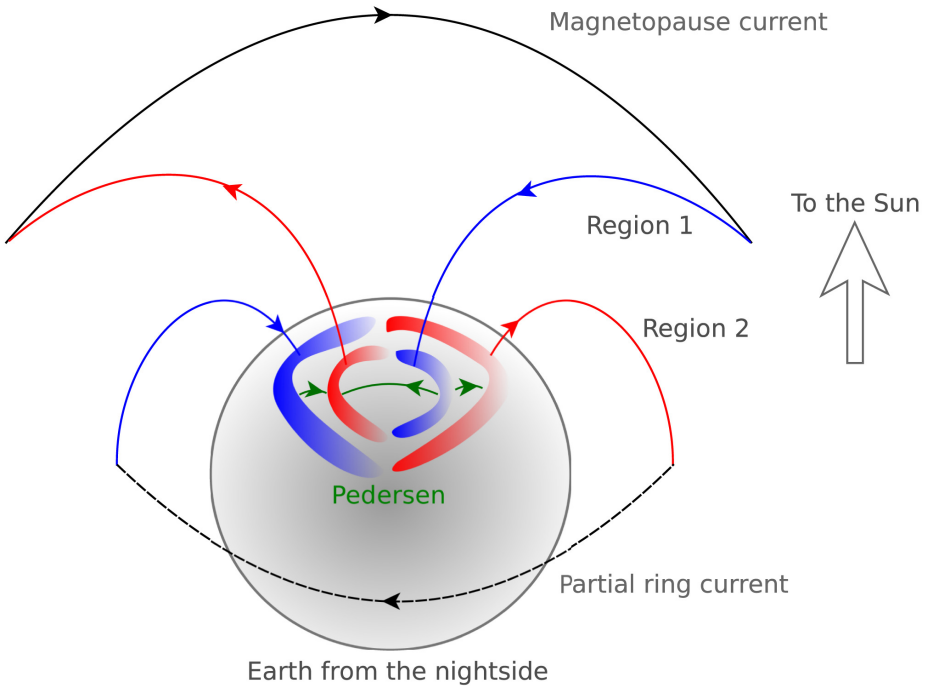

Figure 1.5: Schematic of ionosphere current systems that move couple to the magnetosphere. Figure reproduced from *Carter et al.* (2016).

current deposition of energy into the ionosphere.

The substorm represents a key mechanism by which the magnetosphere can self regulate and contribute to energy transport without the need for strong input signals from the solar wind.

1.2.3 Interplanetary Coronal Mass Ejection

A Coronal Mass Ejection (CME) is a large cloud of plasma with strong magnetic fields that ejects from the solar surface, when it is observed in interplanetary space it is designated as an Interplanetary CME or ICME.

The key features of an ICME are the shock, sheath, and ejecta; each of which are analogous to regions within a magnetosphere (bow shock, magnetosheath, internal magentosphere). Because an ICME is typically traveling much faster than the solar wind around it a shock forms, similar to the bow shock at the magnetosphere, but in Earth's reference frame this shock is traveling near the ICME speed away from the

sun. Just behind the shock is the ICME sheath, again similar to the magnetosheath it contains hotter plasma with large fluctuations in the plasma properties. Finally there is the ejecta where the ICME magnetic field that gives it structure is located. Like a magnetosphere the ejecta has larger magnetic field strength and colder plasma. This cold, magnetized property is equivalent to low plasma β (ratio of thermal to magnetic pressure), and as this magnetic structure slows down to enter the bow shock in front of the magnetosphere it converts it's kinetic energy to heat and even higher field strengths so that the β^* value (ratio of thermal+kinetic to magnetic) becomes comparable to the magnetospheric plasma.

Because the ICME is an interplanetary scale structure many orders of magnitude larger than the magnetosphere the local interaction between the two structures appears as a plane of plasma impinging on the bow shock in front of the magnetosphere. The key properties of this small section of the ICME that determine the coupling with the magnetosphere are the IMF (magnetic field) orientation, dynamic pressure, and solar wind velocity.

1.3 History

1.3.1 1950's to 1990 Discovery of Key Magnetosphere Features and Dynamics

In the 1950's and 60's the regions and boundaries of the magnetosphere were just beginning to be explored, and the dynamics of the system were being studied for the first time. This included the discovery of the solar wind in interplanetary space, the bow shock that surrounds the magnetosphere, and the magnetopause, which isolates the planet's dipole magnetic field.

One of the oldest theories for solar wind magnetosphere coupling and the transport of plasma in the magnetosphere is the Dungey cycle (*Dungey*, 1961), that describes

the motion of the magnetic flux in the magnetosphere during southward IMF. In our case we are looking to describe energy transport rather than magnetic transport but the basic elements should still follow. In the Dungey cycle closed topology changes to open on the dayside and the newly open flux transports downstream where it joins the magnetosphere lobes, there it moves in toward the plasma sheet and reconnects again, moving sunward and completing a cycle that conserves magnetic flux.

Another theory for solar wind magnetosphere coupling was that of *Axford and Hines* (1961), that theorized a viscous like interaction on the flanks of the magnetopause, which would allow for the exchange of momentum and energy from the magnetosheath into the magnetosphere.

Plasma convection is another key driver of energy transport inside of the magnetosphere; the early theory of equatorial plasma convection was established in the 1970's. That is, given an ideal steady state in which the interplanetary magnetic field is not changing with time, the electric field can be considered curl free and therefore projected from the solar wind directly down to the ionosphere. This leads to the Volland Stern model (*Volland*, 1973), (*Stern*, 1975), which predicts the potential pattern in the equatorial magnetosphere based on the combination of the co-rotation potential and the solar wind applied potential. These potentials lead to electric fields that move plasma due to the $\mathbf{E} \times \mathbf{B}$ drift. This drift combined with the gradient and curvature drifts then predicts plasma motion based on particle species, pitch angle, and energy level. Figure 1.6 shows the ion plasma convection pattern for this ideal case. In our analysis we expect to see transport of plasma in a somewhat similar manner with sunward transport within the closed region during the storm interval.

A more quantitative picture of solar wind magnetosphere coupling was proposed by *Akasofu* (1981) twenty years after the previous theories ((*Dungey*, 1961), (*Axford and Hines*, 1961)) that described an energy budget system with energy coming being injected from the solar wind into the magnetosphere and being fully consumed by a

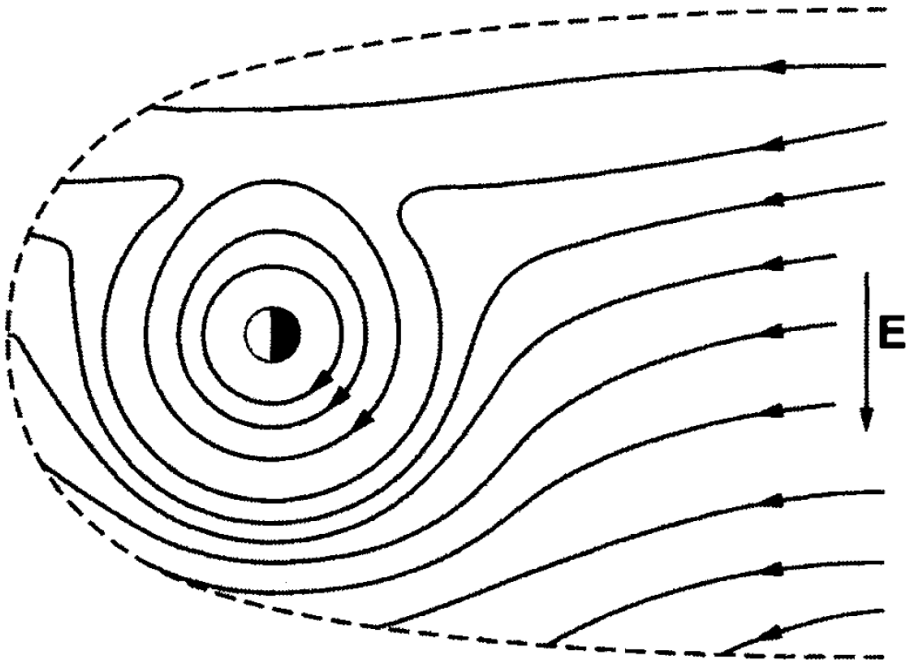

Figure 1.6: Ion plasma drift paths for equatorial magnetosphere given Vollund Stern equipotential lines, adapted from *Gombosi* (1998).

combination of the ring current energy, precipitating auroral flux, and joule heating within the ionosphere. This work gave rise to the first coupling parameter ϵ known as the Akasofu coupling parameter.

1.3.2 1990's and Early 2000's ISTP

Moving ahead to the 1990's there was an international effort to understand the mass, momentum, and energy transport in Earth's magnetosphere called the International Solar-Terrestrial Physics program (ISTP)(*Mish et al.*, 1995). This program led to the launch of many satellites, setup of ground-based observatories, and the creation of important centralized data systems, which paved the way for multi-point observations in order to address the large scientific objective of transport in the magnetosphere. Despite the programs numerous successes, there has yet to be a comprehensive resolution to this question of energy transport in the magnetosphere system. This is because even with both space-based and ground-based observations, it is dif-

ficult to extrapolate the conditions of the entire magnetopause and infer what the global energy transport pattern is. This is where numerical simulations are key to the analyzing the system as a whole.

1.3.3 Previous Investigations Using Simulation

Energy coupling between the solar wind and magnetosphere was first investigated using simulations in 2003 by *Palmroth et al.* (2003), the authors investigating the energy flux through the forward facing boundary of the magnetopause in steady state conditions. Further study by *Palmroth et al.* (2011) and *Pulkkinen et al.* (2008) showed the dependence of the IMF conditions on the energy flux through the magnetopause. Many others ((*Hoilijoki et al.*, 2014), (*Lu et al.*, 2021), (*H. Zhang et al.*, 2023)) have used similar methodology with steady state conditions to explore the relationship between solar wind conditions and energy flux into the magnetosphere.

In this work we build on and expand prior analysis to significantly develop upon the simulated magnetopause definitions, and analyze dynamic solar wind conditions as well as internal boundaries within the magnetosphere to finally attempt to completely address the ISTP's objective of energy transport into and within Earth's magnetosphere.

1.4 Space Weather Modeling Framework

In order to study the transport of energy in Earth's magnetosphere system we need a simulation tool that can model the key aspects of the space environment during storm time. To do this we use the Space Weather Modeling Framework (SWMF) (*Gombosi et al.*, 2021), (*Toth et al.*, 2005).

As the Framework suggests, the SWMF is a flexible grouping of several different models, which can be co-located in physical space and contain different types of physics. For the near earth space environment the SWMF configuration is known

as the Geospace configuration. As mentioned in, the ideal MHD limit works very well in most areas of the magnetosphere so this is how most of the magnetosphere is represented. This MHD model has the Global Magnetosphere (GM) slot in the framework and is filled by the BATS-R-US MHD model (*Toth et al.*, 2005) (*Toth et al.*, 2012).

The other components included in the Geospace configuration are the Ionosphere Electrodynamics (IE) and Inner Magnetosphere (IM), each run with their own non-MHD models. The IE component solves the electrodynamics in the ionosphere by treating the system as a conducting spherical shell with a local conductivity pattern that represents the height integrated conductivity of the ionosphere. The IM component solves the kinetic drift of ions and electrons in the interior of the magnetosphere and overlaps the GM component in space, providing corrections to the MHD macroscopic quantities of density and pressure based on the energy dependent kinetic drifts of the particle populations.

Using the three components together the main features of the solar wind-magnetosphere-ionosphere system are captured and real storm events can be simulated effectively.

CHAPTER II

Fantastic Magnetospheric Boundaries & How to Find Them

2.1 Introduction

The environment in space that is dominated by Earth's planetary magnetic field is known as Earth's Magnetosphere. This region, and the magnetospheres of many other bodies, can be broken down further into smaller regions based on the plasma properties and the dominant phenomena in each region. Between many of these regions exists boundaries that can have finite thickness and their own properties. I will now walk through the major regions and boundaries within Earth's magnetosphere starting from the solar wind, working from the outside in (see figure 2.1).

The Earth's dipole magnetic field carves out a region of space from the surrounding interplanetary space that is dominated by solar wind. This solar wind makes up everything surrounding the limits of the magnetosphere and is comprised of supersonic, super-alfvénic plasma, that carries with it a magnetic field known as the interplanetary magnetic field, or IMF. The solar wind and IMF drive much of the dynamics that occur in the magnetosphere.

Because the solar wind is supersonic and contains its own magnetic field, it hits the Earth's dipole field as one huge obstacle and forms a shock. This bow shock is

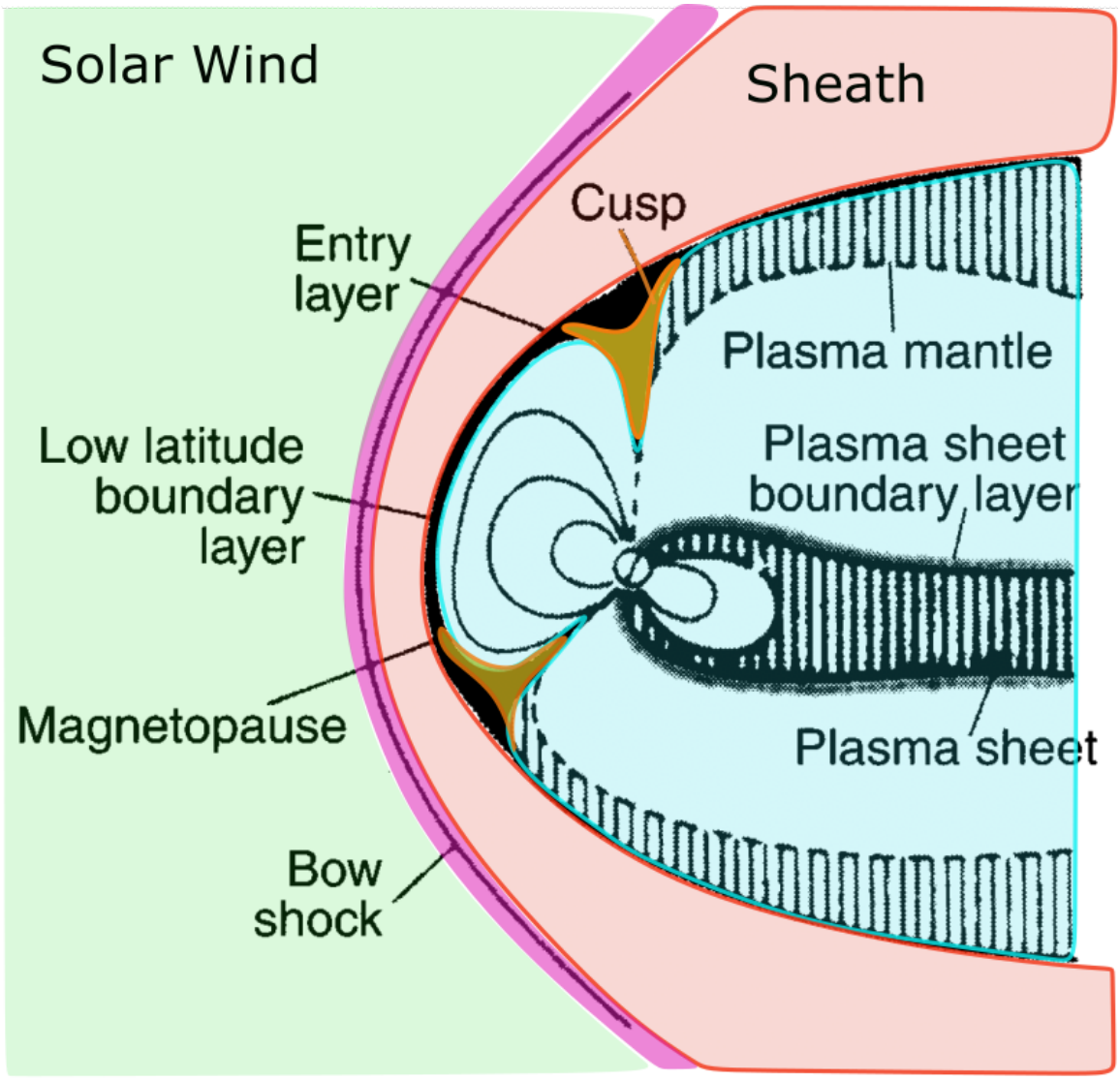

Figure 2.1: Earth's magnetosphere adapted from *Gombosi* (1998)

stationary relative to the planet under steady conditions and facilitates the transition between supersonic flow and subsonic flow closer to the Earth.

As we move in closer we are still in a region that is not considered part of the magnetosphere proper, since the magnetic field is still IMF, albeit with a hotter, slower, shocked solar wind plasma. This region is known as the magnetosheath and is characterized by its unique plasma properties: high temperature and high density. It is also host to many types of plasma waves that can be on the kinetic scale beyond the MHD limit, which makes it more difficult to model with computer simulations.

The inner edge of the magnetosheath is where the magnetosphere officially begins and is known as the magnetopause. The magnetopause is arguably the most important magnetospheric boundary because it makes up the outer edge of space that is magnetically connected to the planets surface. This is important because it means that perturbations to the magnetic field within this boundary will quickly travel along the magnetic field and reach the planet.

Just inside the magnetopause depending on where you look you will find several different transition regions. The first looking near the nose of the magnetopause there is the low latitude boundary layer. As you look higher in latitude this is known as the entry layer. If you continue moving up in latitude approaching the pole there is a null point at the center of a cusp region. Finally going to the other side of the pole there is the plasma mantle between the magnetopause and the lobes.

The distinction of these boundary layers has to do with their magnetic topology and relative position to the magnetosphere's cusp. The cusp is the point at which the sum of the Earth's dipole field and IMF filed along vanishes. Near this point plasma from the solar wind may be able to reach directly down to the planets surface. The way this direct entry occurs or does not occur can differ depending on the solar wind properties.

On the sunward side of the system inside the entry layer and low latitude boundary

layer is part of the closed field region. This is the region that is magnetically connected on both ends to Earth, hence the name closed. The dayside portion of the closed region experiences compression from the solar wind and so is much smaller than the nightside region, with enhanced magnetic field strength. This compressed magnetic field is isolated by electric currents that make up the magnetopause current system.

On the nightside portion of the closed region, rather than being compressed it is stretched out. Near Earth the magnetic field is similar to a dipole field, but becomes more elongated further from the planet at which point it is known as the plasma sheet.

On the edges of the closed field plasma sheet there is a plasma sheet boundary layer, which transitions to the open field lobes. Open field here refers to only connecting magnetically on one end to the planet (for a reasonable distance). If you were to follow a field line in the lobes starting from Earth, it would move through the plasma mantle where it would experience a magnetic rotation, electric field and then join the magnetosheath and eventually the solar wind. The point at which plasma is not longer considered magnetosphere is where it's behavior is no longer influenced by the planets magnetic field.

The electric currents that exist in the plasma mantle and separate the lobes from the magnetosheath are part of what is known as the tail current system. There are several other current system that exist in the magnetosphere and can connect different regions, leading to very complex system behavior (see chapter I, figure 1.3).

In the ionosphere a few boundaries that will be talked about in this dissertation are the so called polar cap, and the auroral oval. The polar cap is the region bounded by the open-closed field line boundary projected down to the ionosphere. The auroral oval is lower latitude than the polar cap and is the region where auroral activity occurs. This is significant because the aurora acts as one of the only plainly visible signatures of magnetospheric activity.

2.2 Empirical Methods

One way of constructing a model of the magnetopause boundary given solar wind conditions is to use spacecraft measurements to infer when the boundary is crossed and use this data to fit an empirical relationship between location and solar wind conditions. Several empirical models like this have been constructed since there has been spacecraft data available to utilize.

In order to obtain usable data for constructing an empirical model, one needs to correctly identify when the magnetopause boundary has been crossed. To do this certain signatures are observed based on the characteristics of plasma between the two regions (magnetosheath and magnetosphere) and fundamental plasma discontinuities.

A plasma discontinuity is a special type of boundary that separates plasma with two distance equilibrium states and is governed by the Rankine-Hugoniot jump conditions. The derivation of these types of jump conditions can be found in every plasma physics textbook, and involves using the MHD conservation equations to step through the possible ways in which mass, momentum, energy, and magnetic field divergence can be conserved given two states that differ in some way. When referring to discontinuities the plane that separates the two regions is used as a reference with normal and tangential referring to across or along this plane.

In the case of the magnetopause there are two types of discontinuities that are found that can be leveraged to find a magnetopause crossing. The first is a tangential discontinuity. In this type the magnetic field and velocity normal to the discontinuity plane is zero for both sides, and all other properties may differ as long as the total pressure acting in the normal direction on each side is maintained. Because B_n and u_n are zero, this balance only includes the sum of thermal pressure and tangential magnetic pressure ($P_{th} + B_T^2/2\mu_0$). The fact that the nose of the magnetopause is a tangential discontinuity should come as no surprise, considering the earlier definition of the magnetopause as a pressure balance between magnetosphere and magnetosheath

plasma. Indeed this is the type of discontinuity found on the closed topology portion of the magnetopause, and when the IMF is northward tangential discontinuities can be found at the lobe boundaries as well.

The second type of discontinuity is a contact discontinuity, in which the magnetic field normal to the discontinuity plane is non-zero but continuous. In some sense this is simply the more generic case of the tangential discontinuity. In this case the tangential velocity, tangential magnetic field, and thermal pressure are continuous as well across the boundary. This discontinuity is found at the lobe boundary, particularly during southward IMF when the magnetosheath magnetic field points with the dipole field downstream. In the case when the normal flow and normal magnetic field are non zero, it is called a rotational discontinuity. In this case both the magnetic field and plasma flow change direction, but not magnitude.

Extending the properties of rotational, tangential and contact discontinuities, one of the most successful and popular magnetopause crossing technique is known as Minimum Variance Analysis. This technique finds the reference frame that isolates the changes in the magnetic field magnitudes in order to infer the possible discontinuity direction. Once this direction is known, based on the change in normal and tangential properties a determination can be made if a certain type of discontinuity was experienced by the satellite. If the satellite experiences a rotational, contact, or tangential discontinuity it is considered a magnetopause crossing.

The NASA Goddard Space Flight Center's Magnetopause Database Website contains a concise summary of much of the following information as well as links to specific crossing data from spacecraft missions (`https://omniweb.gsfc.nasa.gov/ftpbrowser/magnetopause.html`)

In order to complete an empirical model the magnetopause crossing data is fed into a functional form. This functional form is an equation with magnetopause location on one side and some function of solar wind parameters on the other, with coefficients

that are determined by fitting to the data.

Let's look at the popular *J.-H. Shue et al.* (1998) model as an example. This model uses the function form $r = r_0 \left[2/(1 + cos(\theta)\right]^{\alpha}$ with coefficients for the standoff distance and flaring angle r_0 and α that are determined by data. Note that this model outputs the magnetopause location in (r, θ) space where r is a radial distance from the planet and θ is a radial angle moving away from the sun-Earth line. This profile is axisymmetric so it is identical in the XY and XZ planes. To get the standoff distance another equation is solved using the solar wind IMF Bz and dynamic pressure P. The following equations make up the complete model:

$$r = r_0 \left[\frac{2}{1 + cos\,(\theta)}\right]^{\alpha} \tag{2.1}$$

$$r_0 = \left[10.22 + 1.29\text{tanh}\left(0.184\left(B_z + 8.14\right)\right)\right]\left(P\right)^{-\frac{1}{6.6}} \tag{2.2}$$

$$\alpha = \left(0.58 + 0.007B_Z\right)\left[1 + 0.024\text{ln}\left(P\right)\right] \tag{2.3}$$

For the Shue model the 1998 version is an adjustment to the 1997 model, which was based on 553 magnetopause crossings, the majority of this data is sourced from the International Sun-Earth Explorers (ISEE 1 and 2), which had orbits near Zgsm=0 and only to a distance of -10Re in the nightside. Because there is less data in the XZ plane and the model assumes an axisymmetric profile we would expect the results to fit very well near Zgsm=0 and get worse as Zgsm increases.

In addition to the limitation with data availability, the axisymmetric profile fundamentally misses a geometric feature in the magnetospheric cusp. Based on figure 2.1 we can see the cusp geometry of spreading magnetic field lines will create a funnel like shape in the XZ plane that is not present in equatorial plane.

Despite it's limitations, the Shue model is an extremely useful empirical model because of its simplicity, and there are many model variations to choose from if one

Model	Nonaxisymmetric	Dipole Tilt	Analytical Form	Number of Crossings
P96	N	N	Y	6273
KS98	N	N	Y	886
P98	1 point	N	Y	analytical(33)
S98	N	N	Y	553
B00	Y	Y	Y	290
L10	Y	Y	Y	2708
W13	Y	Y	N	15,089
SG15	1 point	Y	Y	1022

Table 2.1: Reproduced from *Samsonov et al.* (2016); Abbreviations of models: PR96 (*Petrinec and Russell*, 1996), KS98 (*Kuznetsov et al.*, 1998), P98 (*Pudovkin et al.*, 1998), S98 (*J.-H. Shue et al.*, 1998), B00 (*Boardsen et al.*, 2000), L10 (*Lin et al.*, 2010), W13 (*Wang et al.*, 2013), and SG15 (*Shukhtina and Gordeev*, 2015)

wants to employ a more complex empirical model. A review paper by *Samsonov et al.* (2016) compares 8 different empirical magnetopause models, these models are listed in table 2.1.

2.3 Tracing Methods

Another type of method for determining the magnetopause location are physics based methods that use simulation results to obtain a solution of the space environment and then find the magnetopause that arises self consistently out of the simulation data. Whereas the empirical methods are able to provide an instantaneous solution of the magnetopause location given a limited set of solar wind conditions, the physics based models require computational resources and time, but can then provide the instantaneous position of the magnetopause including a multitude of feedback effects in addition to the external solar wind conditions.

Given a simulation result that contains the ideal MHD variables at all points in a 3D domain, the state of the art for finding the magnetopause is to use flow field tracing. This technique developed by *Palmroth et al.* has been used in many studies to analyze the transport at the magnetopause ((*Palmroth et al.*, 2003), (*Pulkkinen et al.*, 2008), (*Palmroth et al.*, 2011), (*Wang et al.*, 2014), (*Hoilijoki et al.*, 2014), (*Lu et al.*,

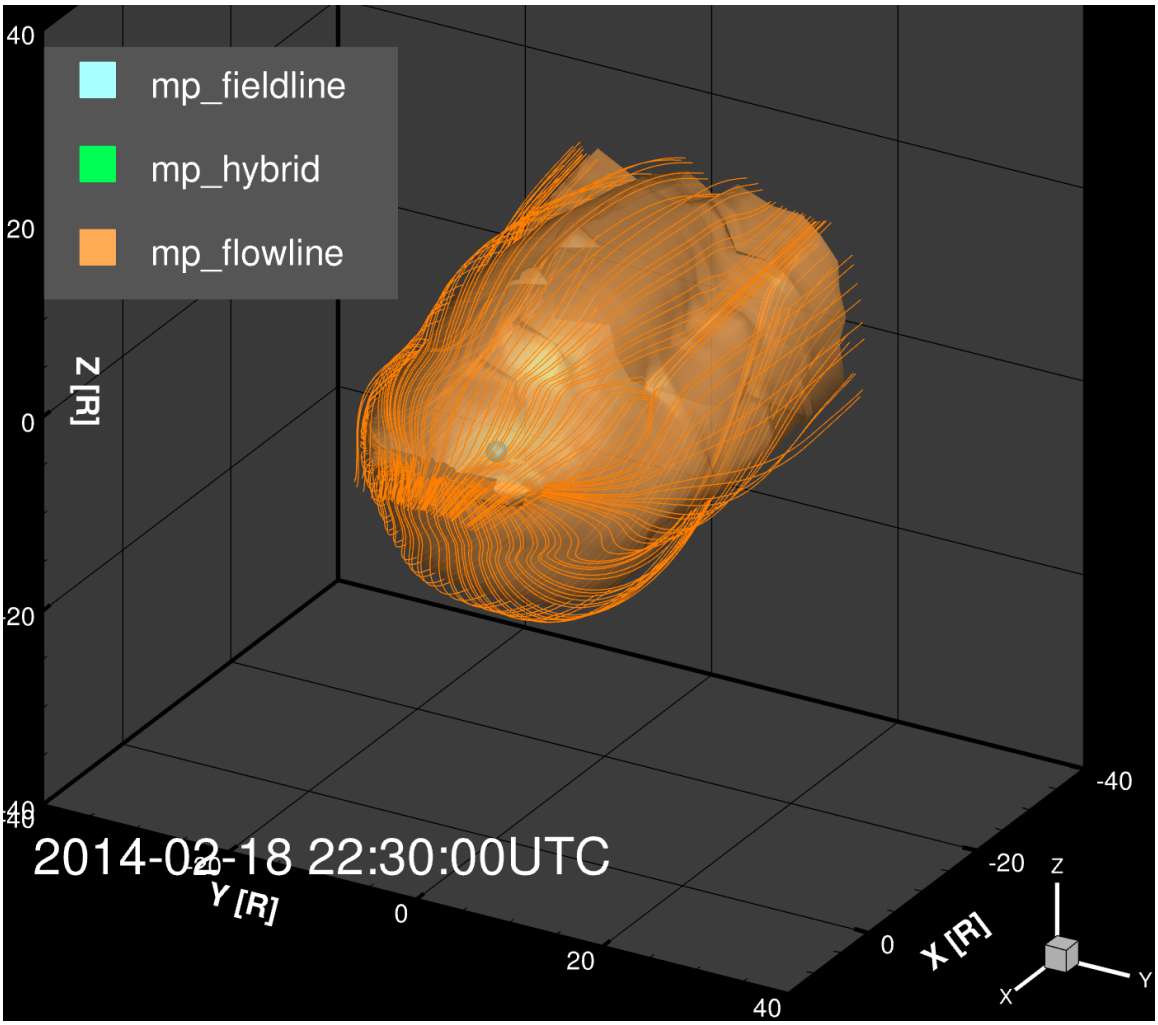

Figure 2.2: Snap shot from SWMF simulation with magnetopause surface identified by tracing the MHD solution flow field (orange traces).

2021), (*H. Zhang et al.*, 2023)) and uses the zero normal velocity characteristic of the plasma discontinuities to identify the magnetopause surface in the simulation output data. Because the magnetopause is often either a tangential or contact discontinuity, by definition there is no flow normal to the discontinuity surface and therefore no flow that penetrates the boundary. So then in order to find this boundary that resists the penetration of flow one can trace the flow field starting from the upstream solar wind and look for the cavity that develops where the flow field is forced to diverge from a straight path after crossing the bow shock. Figure 2.2 illustrates this with a real simulation output data file by simply tracing the flow field.

The full details of the method can be found in *Palmroth et al.* (2003) but to summarize the key steps involved in the flow tracing algorithm:

1. Flow field traces are seeded at a fixed upstream distance
2. The flow lines are ranked by minimum proximity to Earth for each angular position
3. The closest n number of flow lines are omitted
4. The remaining closest m flow lines are averaged to determine the angular radius
5. The surface is constructed by linking the remaining flow line extracted points

The way in which this algorithm is constructed yields important properties for the surface that are somewhat unintuitive; the first of which is that there *can* be flow normal to the boundary of this surface. Because of the closest flow line omissions (step 3), some normal flow is allowed at the boundary. If it were not, the energy flux found at this boundary would be entirely Poynting flux (a full description of energy transport is given in the next chapter). By adjusting the number of omitted flow lines (n in step 3) as well as the range that the remaining field line average is taken (m in step 4) the amount of normal flow allowed can be directly adjusted.

Secondly, near the magnetic cusp the flow field can have large gradients so it can be difficult to capture the funnel shape. Because the gradient of the flow field is large near the cusps when individual traces are omitted and then averaged the result is a surface position that can be moved quite far from the closest approaching flow line. The net effect of this is to smooth the profile near the cusp region, which could have important impacts on the resulting surface normal directions.

In an attempt to improve on this field tracing technique to find the magnetopause, we employed tracing of both the flow field and the magnetic field. Utilizing both fields

may maintain the beneficial properties of the previous technique (almost no normal flow to the boundary) while realizing an improved cusp geometry.

To start, we trace the magnetic field for the portion of the system we believe to contain the magnetopause, seeding all of the field traces in the equatorial plane. We move azimuthally around the equatorial plane using a bisection method to find the field line that is the last point with fully closed magnetic topology. This method is essentially tracking the magnetic topology and yields the closed field line surface that could be constructed by the set of blue points in figure 2.3. This is a useful portion of the magnetopause surface but is incomplete by itself.

Moving off of the equatorial plane we could trace field lines directly from the inner boundary of the simulation domain out to some downstream distance, as illustrated by the red lines from 2.3. Then the equatorial traced lines (blue) and inner boundary traced lines (red) can be merged according to some geometric angle like the GSM XY angle. This yields a nice test case shown in figures 2.3 and 2.4, but only if the open topology field lines behave nicely.

For another test case shown in figure 2.5 we can see that the open topology field lines rejoin the magnetosheath before the downstream cutoff leading to a gross misrepresentation of the magnetopause surface.

From this second example we can see that simple magnetic field line tracing breaks down as the sheath is directly connected to the lobes with magnetic field normal to the surface we are trying to find. Indeed based on the contact discontinuity definition there can be non-zero normal magnetic field at the lobes so there would have to be a criteria for when to stop tracing a lobe magnetic field line.

In an attempt to combine the two techniques the closed field line traced surface is combined with a modified flow field tracing technique. In this hybrid approach the magnetic field is traced as above with a fixed angular width on either side of the positive X axis (+-135^o). Then a similar bisection technique is substituted for steps

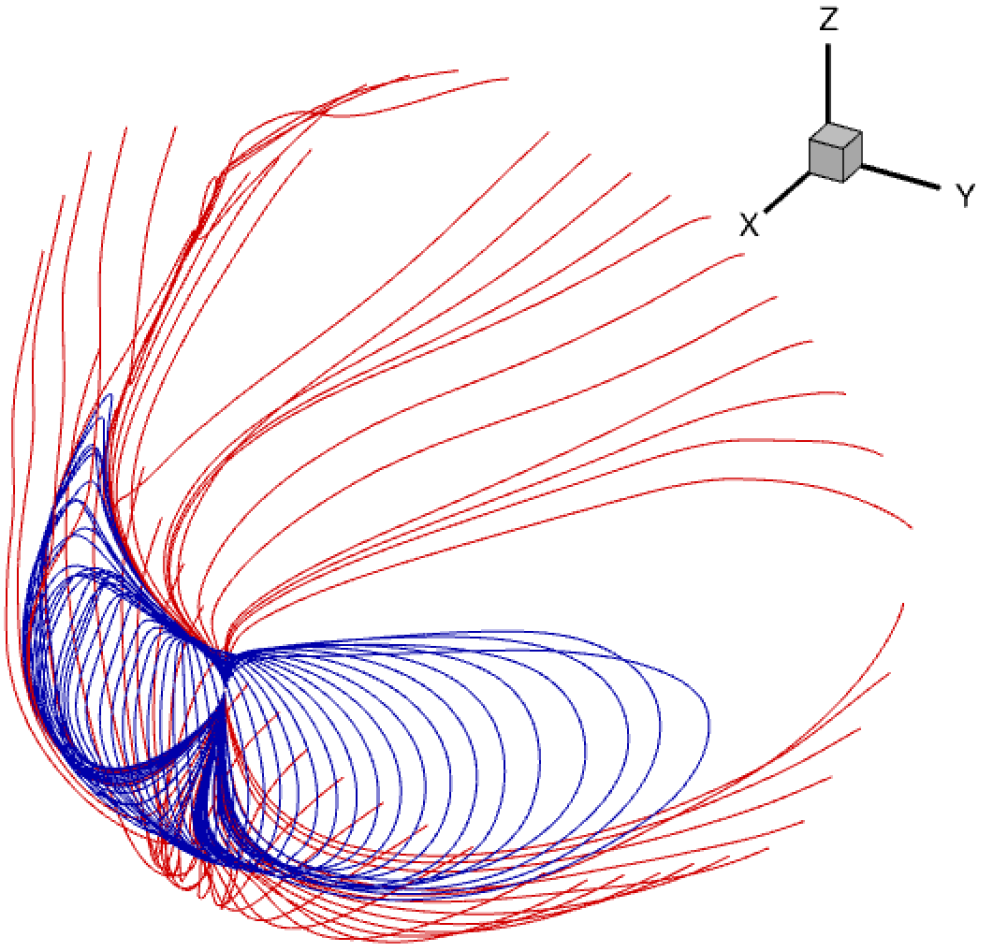

Figure 2.3: Traced magnetic field lines that could be used to construct the magnetopause surface. Blue lines are traced from the equatorial plane to find the last closed-closed field line, red lines are traced from the simulation inner boundary cutoff at a fixed downstream distance.

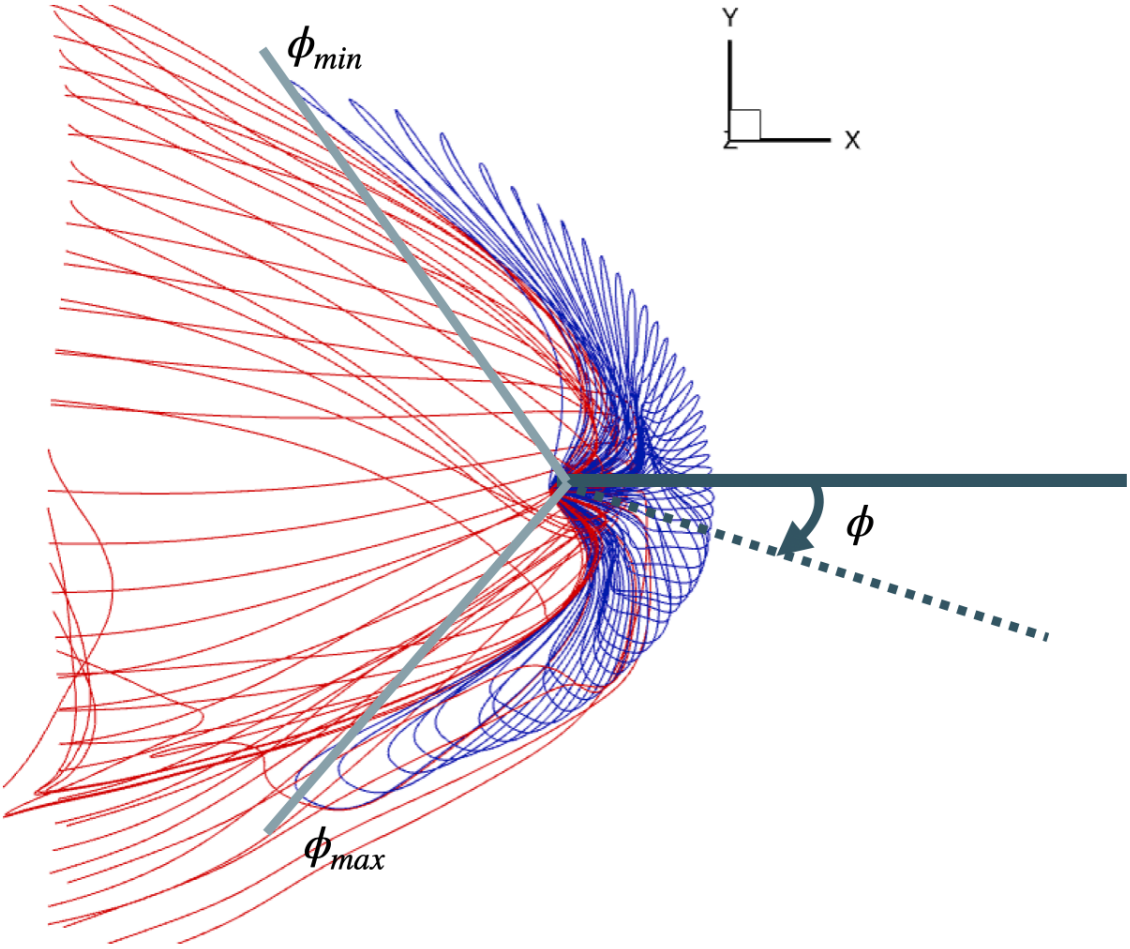

Figure 2.4: Top down view of field line tracing that could be used to find the magnetopause surface. Equatorial traced closed topology field lines (blue) are merged with open topology field lines seeded from the inner boundary (red) according to a merging angle ϕ.

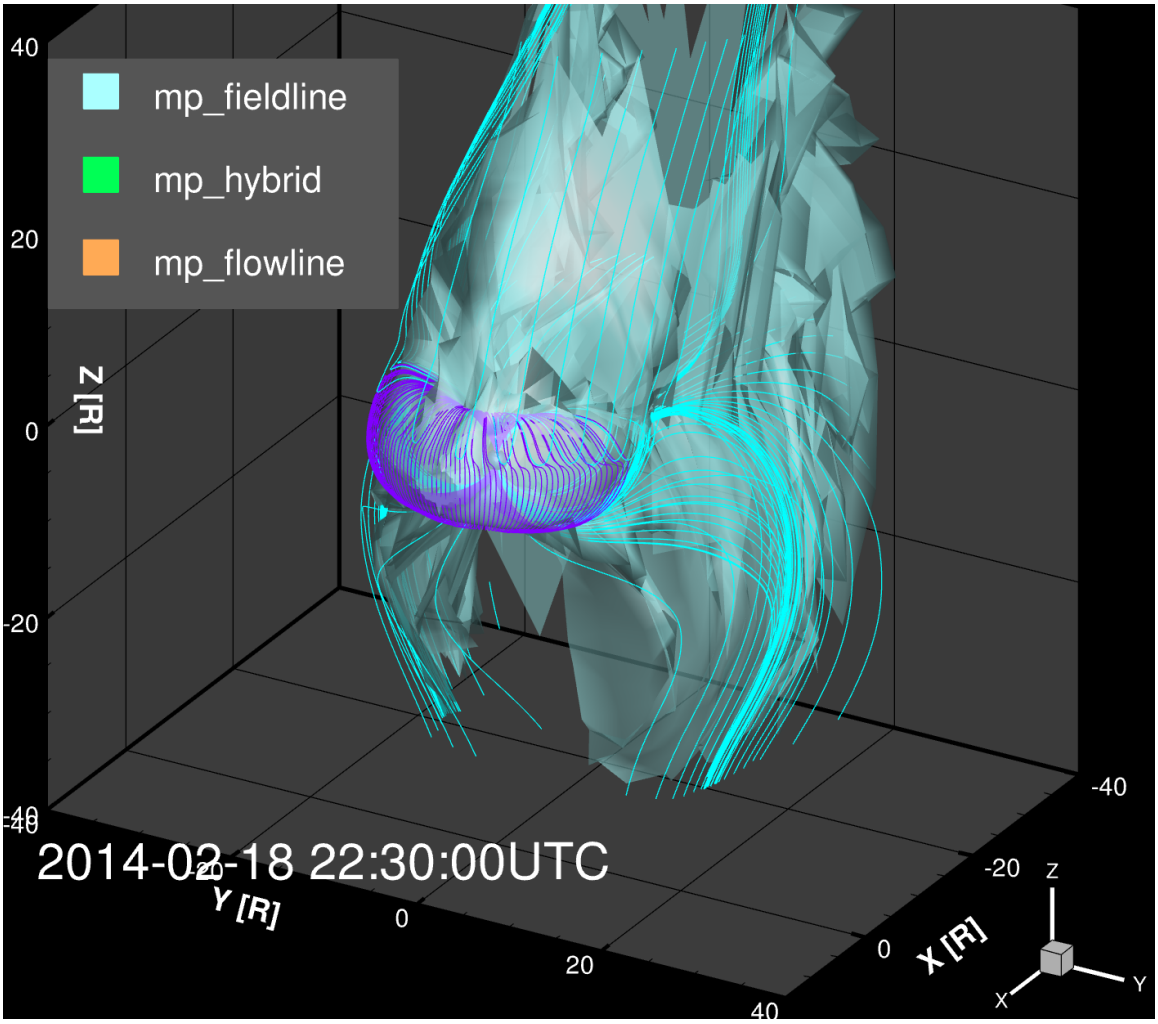

Figure 2.5: Test case from completely field line traced magnetopause algorithm. Purple lines are traced from the equatorial plane with closed topology, cyan lines are traced from the inner boundary with open topology and cutoff at a fixed downstream distance.

2 and 3 of the original flow field search in an attempt to speed up the search process. Finally the combined magnetic field and flow field lines are used together to construct the magnetopause surface.

Combining the closed field line traced surface with a simplified flow field tracing yields a surface like what is shown in figure 2.6; this Frankenstein approach has two major limitations. Firstly the flow field lines are extremely sensitive to the seeding location. Secondly, the cusp geometry becomes extremely pronounced due to the discontinuity between flow field and magnetic field tracing. Where this interfacing happens yields clearly nonphysical results for the surface geometry.

While tracing techniques can be very powerful, the implementation of isosurfaces in the physics based magnetopause model has proved to dramatically improve performance.

2.4 Isosurfaces

Identifying 2D surfaces in 3D space can be efficiently completed using isosurfaces. The isosurface takes a condition, like pressure, from the field values within a domain and finds the surface that contains the field value at that level. The isosurface finds the surface that contains field values of a certain level; for example an isosurface of thermal pressure $P = 1\,[nPa]$ is shown in figure 2.7. Where the hybrid example magnetopause from figure 2.6 takes approximately 30 seconds to generate, the equivalent isosurface can be found in milliseconds.

The isosurface can be found using a variety of algorithms, the most common being the marching cubes (*Lorensen and Cline*, 1987) that is implemented and available through both Tecplot and Paraview visualization software (`https://tecplot.azureedge.net/products/360/current/360_users_manual.pdf`, `https://www.paraview.org/download/`)

The particular isosurface that is of interest for finding the magnetopause is the

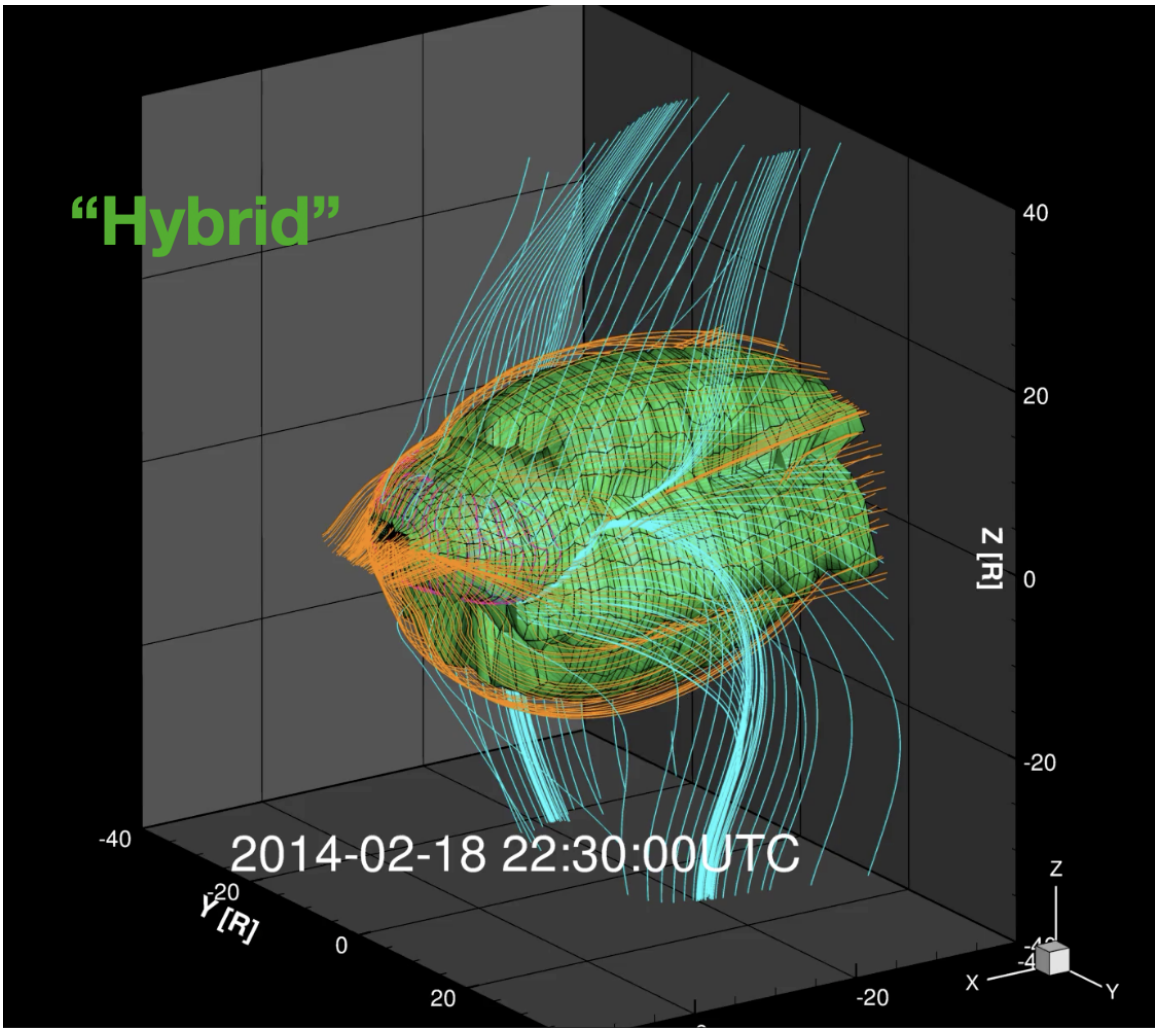

Figure 2.6: Hybrid tracing constructed magnetopause surface. Equatorially seeded closed topology field lines used are shown in magenta, flow field traces seeded from upstream shown in orange, and unused open topology magnetic field traces shown in cyan for comparison with fully field line traced iteration.

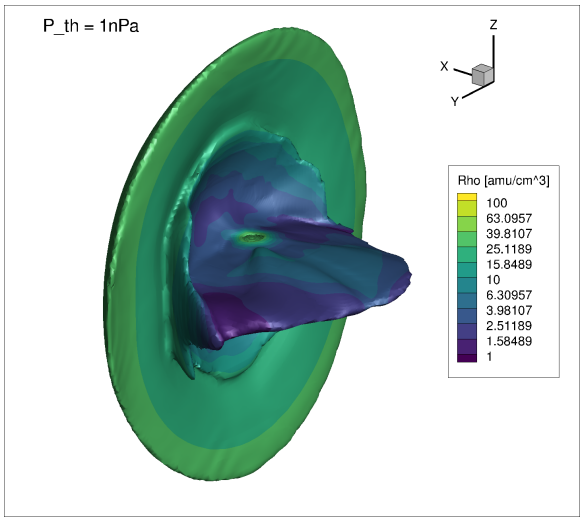

Figure 2.7: Example isosurface of $P_{th} = 1\,[nPa]$.

magnetic topology (labeled Status in SWMF) variable, which encodes the magnetic field tracing information. Magnetic field line tracing is done during simulation run time in order to couple the inner magnetosphere, global magnetosphere, and ionosphere electrodynamics modules, seeding a field line at each cell center. The traced field results are stored based on their magnetic topology value: -1 out of domain, 0 open-open, 1 closed south-open north, 2 open south-closed north, 3 closed-closed.

An important feature of this topology variable is that it is discontinuous, which limits the resolution of the resulting isosurface. Because the algorithm is interpolating the variable results to find the location at which the isosurface value is drawn it will always cut a fraction of a cell size for discontinuous variables. This leads to surfaces with texture proportional to the local cell size, as shown in figure 2.8. This is one limitation when compared with a flow field traced surface that is based on a continuous field.

The discontinuous nature of the topology variable has an upside, which is that it opens up new possibilities in using complex logical expressions. Since the resulting isosurface that includes the topology variable will always be discontinuous, we can use any logical expression (an AND/OR/IF combination) that results in either True

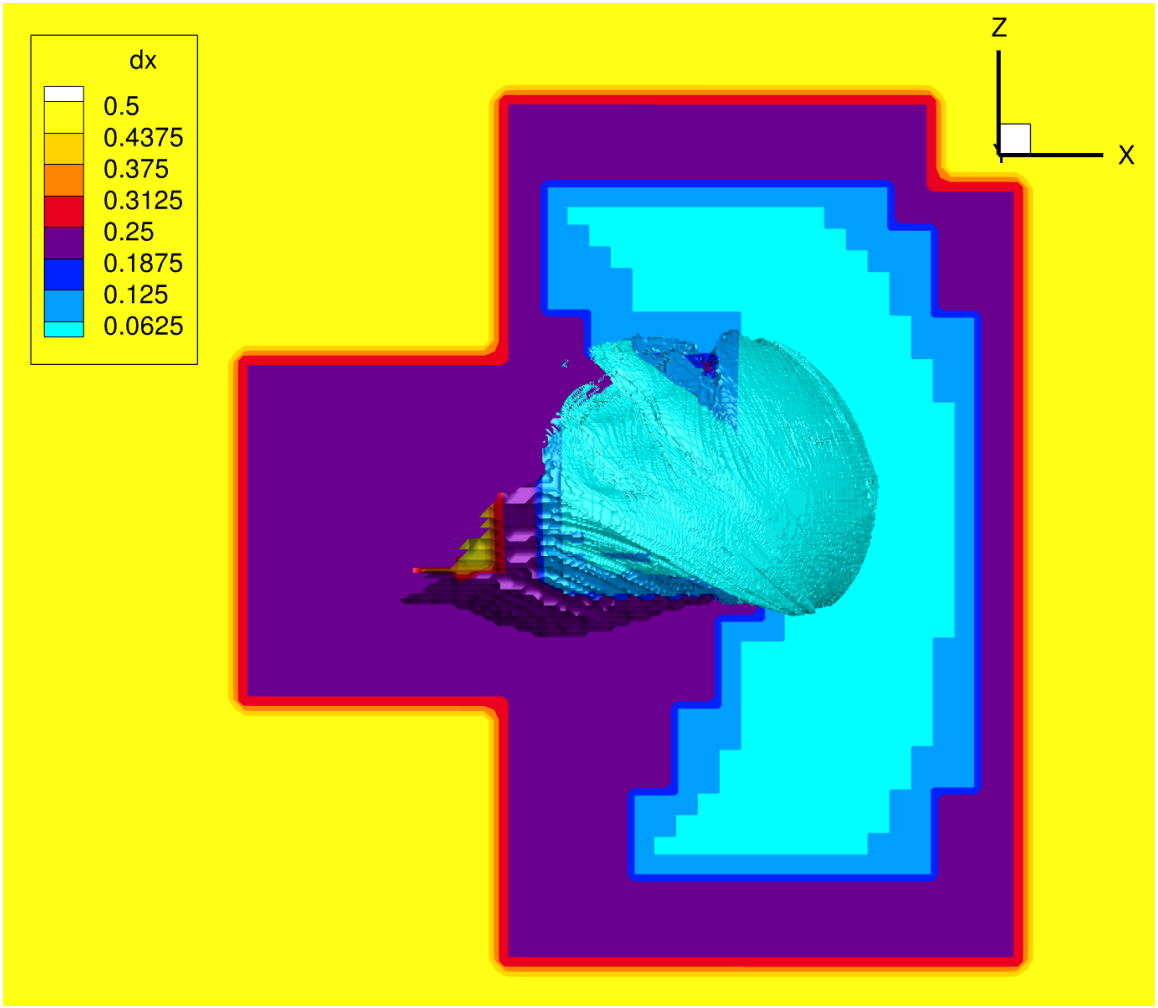

Figure 2.8: Isosurface of magnetic closed-closed topology (Status=3) showing the grid resolution effect on isosurface texture when the isosurface variable is discontinuous.

or False without limiting the isosurface construction any further.

2.5 The Isosurface Magnetopause

We will now define a new magnetopause identification technique using an isosurface defined by logical expressions including the magnetic topology variable. The first condition in the logical expression is that the magnetic topology (Status) is equal to 3 (closed-closed) that is equivalent to tracing the closed field line surface as we did before. We now encounter the same challenge as with magnetic field line tracing in defining the condition that separates the magnetosheath from the lobes.

In order to make this separation we use a modified plasma β variable, β^*, that is a ratio of the thermal and kinetic pressure, to the magnetic pressure. This variable was first introduced in a Martian magnetosphere study (*Xu et al.*, 2016). The theory behind this variable can be seen in the contact and tangential discontinuity definition. Because we are looking for a place where the total pressures are balanced but the pressure contributions (thermal, kinetic, magnetic) jump, this ratio directly highlights that change. Any value between 0.1 and 10 could be used as the specific condition (or even more complicated functions of β^*), but as seen in figure 2.9 the gradient at the interface is extremely sharp so a close match will be found regardless of the particular value.

With $\beta^* < 0.7$ included in our conditions we now have a full coverage of the magnetospheric boundary, but we include additional conditions to have more control and account for edge cases. One type of additional condition is $X_{gsm} > -20$ and $R_{gsm} > 3$. These simple geometric constraints act as a cutoff and enforce an inner boundary for the analysis that may be different from the simulation inner boundary.

Another additional condition is that the topology variable must NOT be equal to 0 (open-open), which represents the sheath or solar wind; this condition can help avoid including low β^* solar wind plasma that is part of the sheath. This occurs particularly

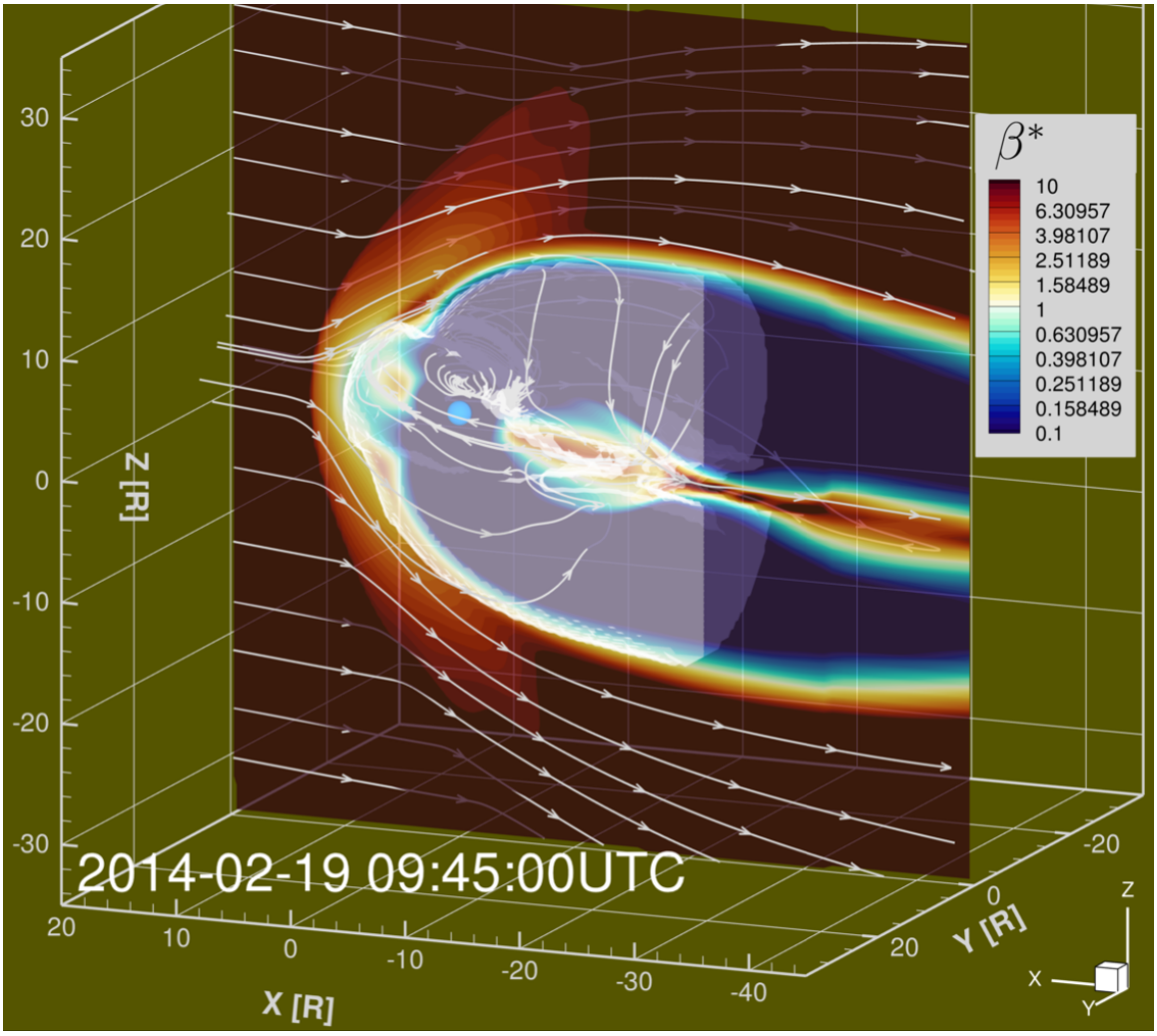

Figure 2.9: Isosurface magnetopause (translucent surface) with XZ slice contoured by β^* the ratio of thermal and dynamic pressure to magnetic pressure. White lines trace the total energy flux **K** field. More details about energy transport is given in chapter III.

during coronal mass ejection events where there is a magnetic cloud ejecta with low mach number that has enhanced magnetic field strength. When it slows near the bow shock nose it can appear as magnetosphere plasma in terms of plasma β and β^*.

This magnetopause has a robust definition because the field tracing is done at every single cell during run time, but it is still sensitive to the tracing details and grid size. If the fast tracing technique (parallelized fast magnetic field tracing details can be found in *De Zeeuw et al.* (2004) and *Glocer et al.* (2009a)) is used or tracing is not done at every output time step the topology variable can yield misleading results.

A major benefit of this magnetopause is the magnetic contour is consistent up to and across the cusp region. Because the magnetic field defines the boundary on the dayside the contour is extremely sharp and the effects of dayside magnetic reconnection are directly observed, as opposed to the flow field traced surface in which there can be some small layer between the last closed field line and the flow field traced magnetopause surface. The cusp geometry likewise is then contoured in a sharper way using the isosurface method, which will improve the local surface normal direction in this region. The cusp region can experience large gradients and contribute significantly to the energy transport process.

In this magnetopause the plasma sheet on the downstream side of the X line is explicitly omitted; this will be a function of the optional tail cutoff parameter and will lead to stronger volume change signals as the tail cutoff distance increases. Because the topology variable is so highly utilized the moment that cells in the plasma sheet become open-open they are removed from the magnetosphere. This will appear as a sudden loss in magnetosphere volume whereas with a less sensitive magnetopause surface one would observe a static energy flux of the X line contents moving downstream.

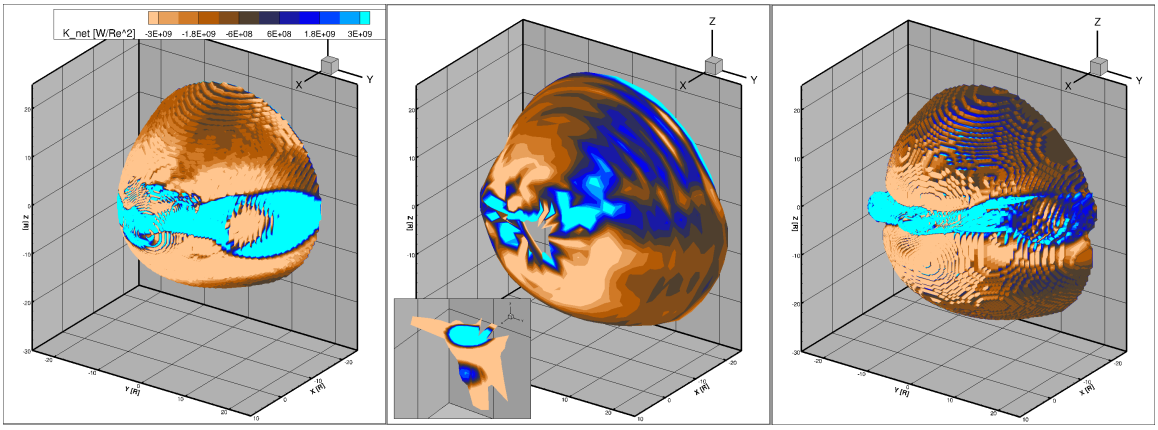

Figure 2.10: Three models for a simulated magnetosphere. Left: Shue 1998 empirical model, middle: flow field traced model, right: isosurface magnetopause model. Surfaces contoured by total energy flux **K**, for more details about energy transport calculations see chapter III. Middle panel surface is ordered zone so normal flux for the nose plane shown in the pop-out.

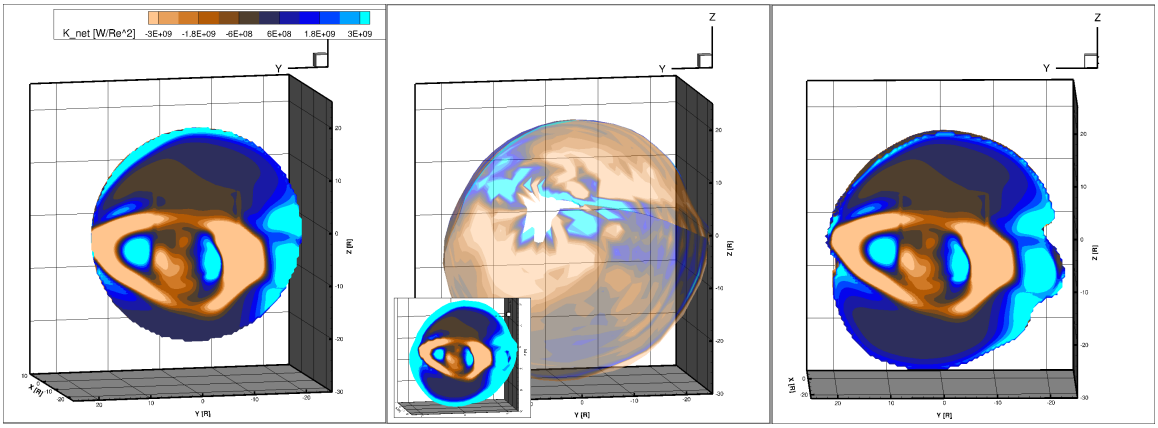

Figure 2.11: Backside view of figure 2.10

2.6 Model Comparisons

Let's now take a look at how an empirical model, a flow traced model, and the isosurface model compare for a snapshot from a simulated storm event. The Shue 1998 model is used with solar wind conditions taken from $+30R_E$. The flow field traced magnetopause uses 200 backward traced stream lines. The isosurface magnetopause uses the fast type field tracing for the topology variable and a β^* threshold of 0.7. Figures 2.10 and 2.11 show each of the three surfaces used in this demonstration.

The results are taken as a snapshot from a real event simulation, described in

detail in chapter III, that occurred on February 19, 2014; this snapshot is of Feb 19, 06:40UT. Just upstream of the bow shock the IMF is B_{xyz} $[5.8, 11.0, -11.4]$ with solar wind dynamic pressure 3.4 nPa, and plasma $\beta = 0.138$.

The first metric we will use to compare is the three magnetopause surfaces is the standoff distance, this is the furthest distance in the X direction where the incoming magnetosheath flow stagnates. The standoff distance for the flow-traced model and isosurface model are identical because the last closed field line was used to fix the maximum extent of the flow-traced model.

Next the magnetopause surfaces are compared by their integrated areas. Changing the surface area is one the most direct ways to impact the surface integration results and so large discrepancies in the area should correspond to large changes in integrated energy transport.

Lastly the surfaces are compared via surface integrated flux values, which takes into account the surface area, location, and orientation. Surface flux if given by $\int_{mp} \mathbf{K} \cdot \mathbf{n} dA$, this flux vector $\mathbf{K}$ is dotted with the surface normal vector $\mathbf{n}$ that points outward from the volume enclosed by the magnetopause surface. More details about the surface flux analysis details is given in chapter III.

The results shown in figure 2.12; while the stand off distances are close all three models differ in their total surface area and integrated total energy flux. For the standoff distances (top bars) of both the Shue model and isosurface magnetopause a logical expression variable was used resulting in an isosurface of a discontinuous function yielding blocky texture and a standoff distance value at a 1/4 Re increments. The differences in surface areas (middle bars) between the flow-traced and isosurface models are small, yet the resulting surface integrated flux (bottom bars) have a 200% difference, which demonstrates the need to carefully determine magnetopause position at each time step.

Clearly the choice of surface definition are critical to the evaluation of the surface

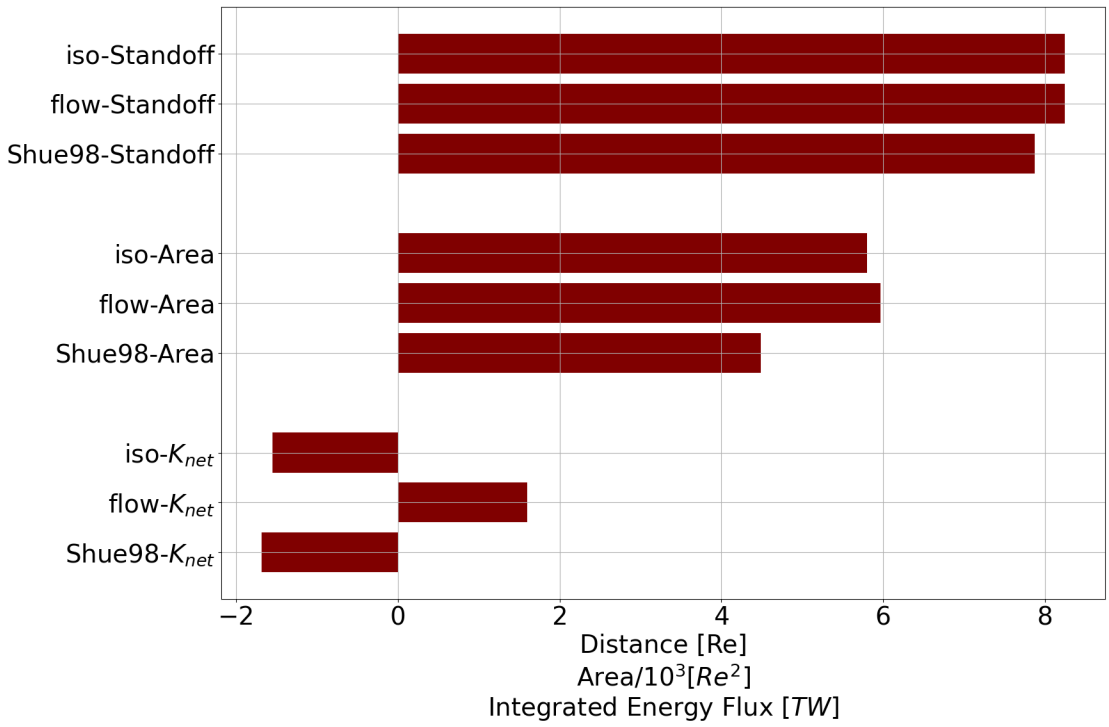

Figure 2.12: Comparison of three simulated magnetopause models. Top three bars compare the magnetopause standoff distance in Re, middle three compare the surface area divided by 10^3 in Re^2, last three panels compare surface integrated total energy flux in TW.

energy transport, which will be the focus in the next chapter. The isosurface magnetopause will was selected based on its speed of calculation, simplicity, and theoretical robustness.

2.7 Ionosphere Boundaries

The ionosphere also has important regions with boundaries between them; two of the most important are the polar cap and the auroral oval, which are critical to the dynamics of the magnetosphere because of the way the two systems are so tightly coupled. Unlike the magnetospheric boundaries the polar cap and auroral oval were not the main focus of the work in this dissertation so only a brief overview is given here. Furthermore, the ionosphere considered here is a simplified height integrated 2D spherical shell.

The polar cap is the projection of the magnetic topology from the magnetosphere down to the ionosphere and is important to magnetosphere-ionosphere coupling because it restricts the plasma flow by only allowing flow to cross the boundary in the portions where the topology is changing (dayside and nightside reconnection zones). For the simulation setup used in this work (SWMF) the ionosphere is modeled as a thin shell so the topology boundary collapses from 3D to 2D.

The ionosphere north and south polar caps can be split into dayside and nightside by cutting the system across the Y_{SM} (solar magnetic) plane. This is the plane that contains the dipole axis and the Y_{GSM} axis. By separating the dayside and nightside polar caps the major reconnection sites (dayside and nightside) effects can be better studied.

The auroral oval is more challenging to define in the simulation results because it relies heavily on particle precipitation that can be difficult to capture using ideal MHD models. The auroral oval is the region in which the aurora are visible and often occurs just below the polar cap in latitude. The visible light created by the aurora is

from excited particles experiencing collisions and releasing some energy as light. This particle excitation comes from precipitating particles from the magnetosphere down to the ionosphere. There can be many types of energy precipitation that can be a product of complex interactions between co-located plasma populations and plasma waves and is a broad and active area of research. The auroral boundary implemented in the SWMF version used in this work is a fixed latitude band that is modulated by the cross polar cap potential value. For more details about the auroral effects on the ionosphere component in SWMF see the original publication for the Ridley Ionosphere Model (RIM) (*Ridley et al.*, 2004) and a more recent publication describing an improved empirical model that governs the conductance in the ionosphere auroral zone (*Mukhopadhyay et al.*, 2020).

CHAPTER III

A Song of Escape and Injection: Energy Transport at the Magnetopause

3.1 Introduction

In this chapter we use the magnetopause definition and identification technique found in the previous chapter to investigate questions of solar wind magnetosphere coupling by looking at the energy transport at the magnetopause surface. First we will cover some background on energy transport definitions and an overview of the science questions, then discuss the published study using a simulation of a real storm event.

Total energy density in the MHD limit is given as the sum of hydrodynamic energy density and magnetic energy density. $U = U_{hydro} + U_{mag} = \left(\frac{1}{2}\rho u^2 + \frac{1}{\gamma+1}P_{th}\right) + \left(\frac{B^2}{2\mu_0}\right)$.

Energy flux is the transport of energy across a surface per unit time and has units of $[W/m^2]$; its type depends on the type of energy being transported. Energy flux that transports magnetic energy is called Poynting flux, while energy flux that transports thermal and kinetic energy is referred to here as hydrodynamic flux. Others sometimes refer to this type of energy flux as mechanical energy flux.

The term hydrodynamic was chosen intentionally to highlight that the energy flux is evaluated in the MagnetoHydroDynamic limit (MHD). The ideal MHD equations

in conservative form are given in in equations 3.1-3.4. From the energy equation (3.3) the machinery of energy flux is evident as a quantity (scalar value) transported by an advector (vector with magnitude and direction). In the case of hydrodynamic flux the quantity is $\left(\frac{1}{2}\rho u^2 + \frac{\gamma}{\gamma-1}P_{th}\right)$ and the advector is $\mathbf{u}$. For Poynting flux there are two components $\left(\frac{B^2}{\mu_0}\right)$ advected with $\mathbf{u}$ and $\left(\frac{\mathbf{B}\cdot\mathbf{u}}{\mu_0}\right)$ advected with $-\mathbf{B}$.

$$\frac{\partial \rho}{\partial t} + \nabla \cdot (\rho \mathbf{u}) = 0 \tag{3.1}$$

$$\frac{\partial (\rho \mathbf{u})}{\partial t} + \nabla \cdot \left(\rho \mathbf{u}\mathbf{u} + P_{th}\overline{I} + \frac{B^2}{2\mu_0}\overline{I} - \frac{\mathbf{B}\mathbf{B}}{\mu_o}\right) = 0 \tag{3.2}$$

$$\frac{\partial}{\partial t}\left(\frac{1}{2}\rho u^2 + \frac{1}{\gamma-1}P_{th} + \frac{B^2}{2\mu_0}\right) + \nabla \cdot \left(\frac{1}{2}\rho u^2 \mathbf{u} + \frac{\gamma}{\gamma-1}P_{th}\mathbf{u} + \frac{(\mathbf{B}\cdot\mathbf{B})\mathbf{u} - \mathbf{B}(\mathbf{B}\cdot\mathbf{u})}{\mu_0}\right) = 0 \tag{3.3}$$

$$\frac{\partial \mathbf{B}}{\partial t} + \nabla \cdot (\mathbf{u}\mathbf{B} - \mathbf{B}\mathbf{u}) = 0 \tag{3.4}$$

The motivating questions for this work are:

- How much energy is transported across the magnetopause for a real event under different storm phases and conditions?
- How does the energy transport vary with regards to magnetopause location and energy flux type?
- How much does the boundary motion play a role in controlling the energy transport process?

Studies prior to this focused on idealized simulation events in which the solar wind conditions are steady or smoothly varying. In this work we focus on a real storm event that will exhibit rapid changes in the solar wind conditions.

3.2 Methodology

Using energy flux in the ideal MHD limit defined earlier we calculate the total energy transported across the magnetopause per unit time by taking the surface integral of the energy flux normal to the boundary.

$$\text{Power}\,[W] = \int\limits_{mp} \mathbf{K} \cdot \mathbf{d}\mathcal{S} = \int\limits_{mp} \mathbf{K} \cdot \mathbf{n} dA \tag{3.5}$$

This energy can then be split by type from Total ($\mathbf{K}$) into hydrodynamic ($\mathbf{H}$) and Poynting ($\mathbf{S}$), and the surface can be split according to a variety of criteria to investigate how power is coupling through the magnetopause surface. The sign convention for the surface normal is to point out away from the interior of the volume enclosed by the magnetopause surface.

Because one of the objectives is to quantify the effect of the boundary motion we must account for the energy transport associated with the moving surface. Using Reynolds transport theorem the time rate of change of the total energy density within the volume enclosed by the magnetopause is:

$$\frac{d}{dt} \int\limits_{\mathcal{V}(t)} U d\mathcal{V} = - \int\limits_{\mathcal{S}(t)} (\mathbf{K} - U\mathbf{q}) \cdot \mathbf{d}\mathcal{S} \tag{3.6}$$

Where $\mathcal{V}(t)$ and $\mathcal{S}(t)$ are the volume enclosed by and the surface of the magnetopause that changes in time. U is the energy density, $\mathbf{K}$ is the energy flux, $\mathbf{q}$ is the local surface element velocity, and $\mathbf{d}\mathcal{S}$ is the surface element vector. From this equation there is the sum of the static and motional portions within the integrand. For the motional portion it is much easier to evaluate the integral by first transforming it back into a volume integral. The surface element velocity is so difficult to determine because there is no 1-1 correspondence between surface elements between timesteps, so calculating a change in surface element position in order to approximate the speed

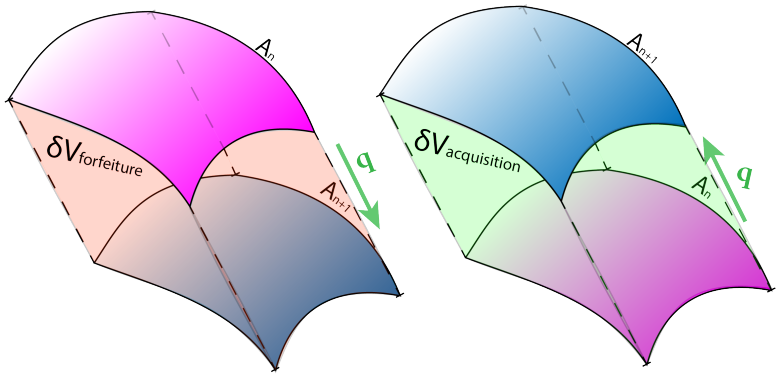

Figure 3.1: Diagram of the volume approximation of surface motion contribution to integrated energy flux. A surface element is shown at time t_n (pink) and time t_{n+1} (blue) with local surface element velocity of $\mathbf{q}$. The expanding surface case is shown on the right, where volume and therefore energy increases ($+\delta V$), which represents flux injection. The reverse is true for the contracting volume case shown on the left.

becomes challenging. The last term in equation 3.6 can be written as:

$$\int_{\mathcal{S}(t)} U\mathbf{q}\cdot\mathbf{d}\mathcal{S} = \int_{d\mathcal{V}/dt} U d\mathcal{V} \approx \frac{1}{\delta t}\int_{\delta\mathcal{V}} U d\mathcal{V} \tag{3.7}$$

which is in essence taking the volume integral of total energy density (U) over the volume differences between the magnetosphere at time t_n and t_{n+1} divided by the time step taken as shown in figure 3.1. This approximation improves with smaller time steps similar to any finite difference approximation of a derivative.

To directly compare the motional contributions for different types of energy the total energy density U can be swapped for the hydrodynamic energy density U_{hydro} or magnetic energy density U_{mag}.

In addition to the static-motional and injection-escape distinctions in integrated energy flux we also investigate the spatial distribution of the energy flux pattern. We do this by splitting the magnetopause into three sectors shown in figure 3.11.

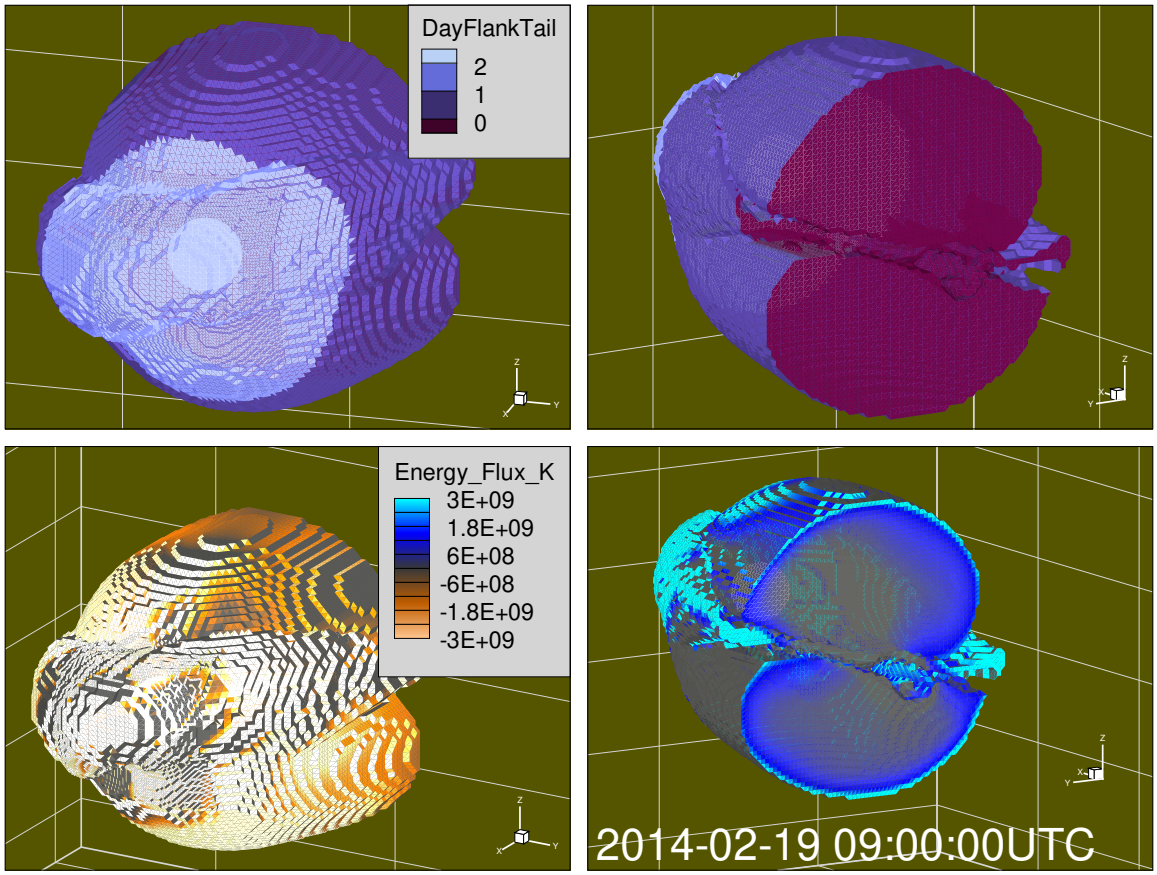

Figure 3.2: Top panels show spatial split of surface integrated flux to investigate the spatial variability. Day: defined as $X > 0$, Tail: defined as $X = X_{min}$ locally, and Flank: defined as the remainder of the magnetopause surface. Bottom panels show energy flux isolated by injection (left) and escape (right).

3.3 Simulation Setup and Quality

The SWMF in Geospace configuration was used for this simulation, with Global Magnetosphere (GM), Inner Magnetosphere (IM), and Ionopshere Electrodynamics (IE) components. For the GM component the BATS-R-US model was used with ideal MHD equations. The grid resolution was fixed with respect to time. PARAM.in commands for the grid resolution are given in table 3.1.

The Rice Convection Model (RCM) and Ridley Ionosphere Model (RIM) were used for the IM and IE components respectively. With the exception of the grid resolution and output settings, there was little variation in the parameter settings from Space Weather Prediction Center (SWPC) operational setup (*Pulkkinen et al.*, 2013).

3.4 Real Event Setup

3.4.1 Solar Wind Conditions

The event studied occurred on February 18-20, 2014 when Earth's magnetosphere was impacted by multiple Interplanetary Coronal Mass Ejections (ICME); these impacts caused several magnetopause motions and large amounts of energy transport, which makes it a good event candidate. The top three panels of Figure 3.3 show the key plasma properties of the incoming solar wind during the ICMEs impacts with yellow shading indicating sheath and green the ejecta of each ICME; each of the three plasma properties is responsible for a different type of effect on the system. The IMF (panel 1) controls the dayside reconnection rate and the primary mode of coupling between the solar wind and magnetosphere, the solar wind velocity (panel 2) controls the total energy transport entering into the system and therefore available to be coupled to the magnetosphere, and the dynamic pressure (panel 3) controls the magnetosphere shape and can have strong effects when there are rapid changes.

#GRIDRESOLUTION	
2.0	Resolution
initial	NameArea
8.0	Resolution
all	NameArea
1	Resolution
box	NameArea
-100.0	xMin
-16.0	yMin
-16.0	zMin
22.0	xMax
16.0	yMax
16.0	zMax
1/4	Resolution
box	NameArea
-20.0	xMin
-8.0	yMin
-8.0	zMin
8.0	xMax
8.0	yMax
8.0	zMax
1/2	Resolution
box	NameArea
-32.0	xMin
-25.0	yMin
-25.0	zMin
20.0	xMax
25.0	yMax
25.0	zMax
1/2	Resolution
paraboloidx	NameArea
20.0	xPosition
0.0	yPosition
0.0	zPosition
-52.0	Height
35.0	Radius
1/8	Resolution
shell0	NameArea
2.5	rMin
3.5	rMax

Table 3.1: Grid resolution parameters for simulated event study.

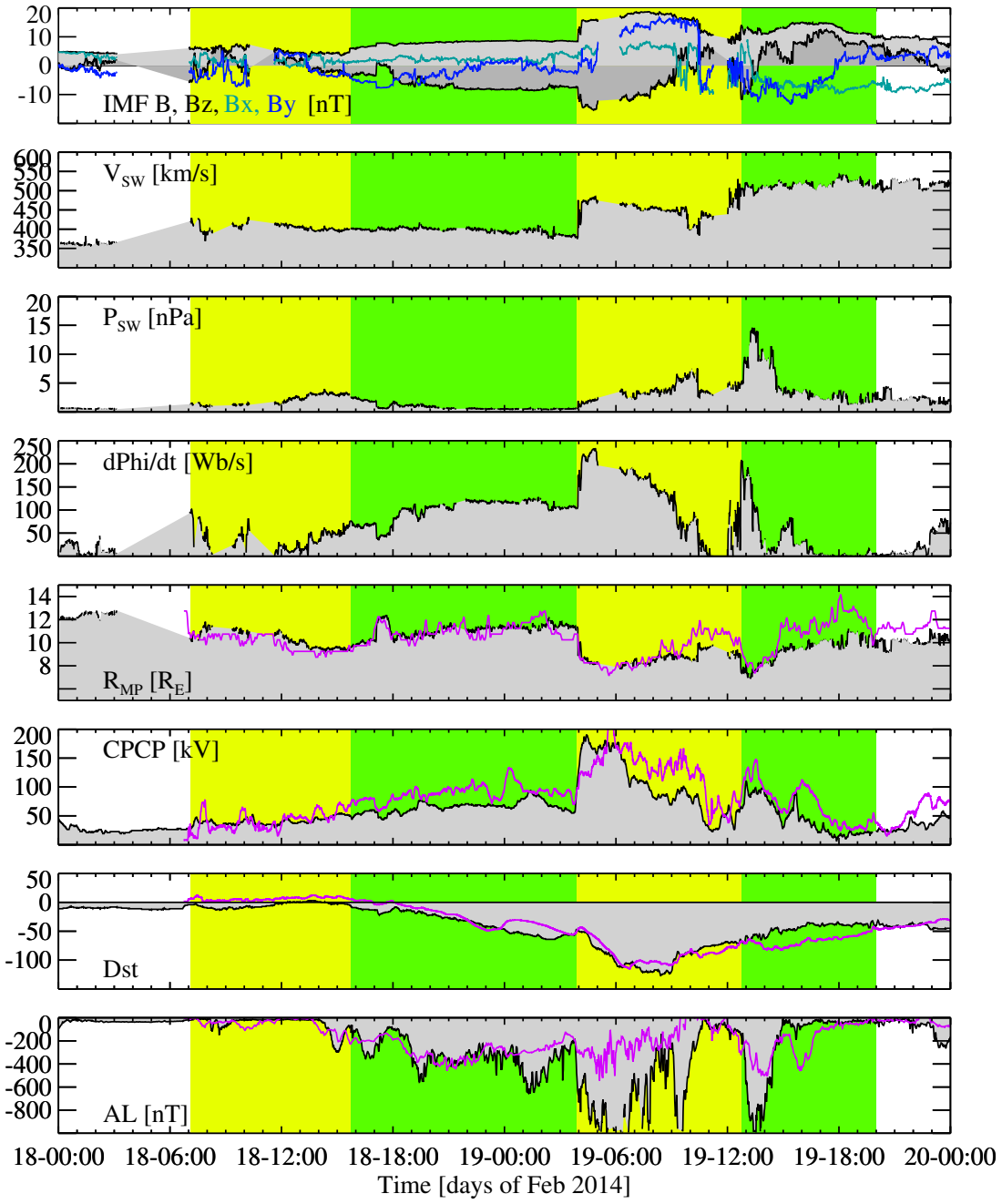

Figure 3.3: From **?**: Solar wind conditions, empirical model results and global indices for Feb2014 multi-ICME impact event.

The IMF orientation is shown in panel 1 with the magnitude shaded as light grey in the background. Classically, the $B_z$component of the IMF is primarily responsible for the rate of dayside reconnection, which re-configures the magnetosphere topology to allow direct mass, momentum, and energy transport. For this event around 15:30UT on Feb 18 with the arrival of the first ICME ejecta (first green patch), the IMF B_z component becomes negative, which begins the main phase of the geomagnetic storm. As the second ICME shock and then sheath hit (second yellow patch) the magnetic field strength increases and the negative B_z component is enhanced leading to increased coupling with the magnetosphere. Towards the end of the second ICME sheath (09:00UT on Feb 19), the B_z component turns positive and remains that way through the second ICME ejecta allowing the magnetosphere to enter it's recovery phase of the storm.

Panels 2 and 3 show the solar wind velocity and dynamic pressure, which remain at steady values until the second ICME shock front (transition from green to yellow). The velocity before this transition is around the nominal value of 400km/s and jumps by about 50km/s during the second ICME sheath and then by another 50 km/s in the second ICME ejecta. This higher velocity (500km/s) yields more total energy in the surrounding solar wind available to couple to the magnetosphere. The dynamic pressure starts low but rises to around 5nPa during the second ICME sheath and then steadily rises until a sharp rises to 12nPa for 3 hours just after the second ICME ejecta starts. We can expect to see a highly compressed magnetopause during this interval.

3.4.2 Empirical Model Results

Next we can examine this storm event by using empirical models that give instant results without the simulation data; the three empirical model results shown in the middle three panels of figure 3.3 are the Newell Coupling function ($d\phi/dt$), Shue mag-

netopause standoff distance (R_{mp}), and Ridley and Kihn Cross Polar Cap Potential (CPCP).

The Newell coupling function is a model for the rate of magnetic flux added to the polar cap due to dayside magnetic reconnection (*Newell et al.*, 2007). This is one form in which energy can couple through the magnetopause so it will make a nice comparison for this study. The coupling function is based on many geomagnetic indices and large sets of data to relate the solar wind conditions to a geomagnetic response and is given by the following formula:

$$\frac{d\Phi_{MP}}{dt} = \alpha \left[u^2 B_T sin^4 \frac{\theta}{2} \right]^{2/3} \tag{3.8}$$

where Φ is the magnetic flux in Webers, u is the solar wind velocity in km/s, $\theta = \tan^{-1}(B_Y/B_Z)$ is the IMF clock angle, and $B_T = (B_Y^2 + B_Z^2)^{1/2}$ is the magnitude of the magnetic field transverse to the X_{GSM} direction. Finally α is a constant factor of $10^3 Wb/s$ used to normalize the model.

The Newell coupling function shown in the fourth panel predicts polar cap flux increase beginning before the start of the main phase of this event due to the B_Y component in the first ICME sheath. This model then predicts the rate of flux addition to remain steady through the first ICME ejecta, peak at the second ICME shock, and then linearly declines through the second half of the second ICME sheath. The model also predicts a peak in magnetic flux addition rate at the same time as the dynamic pressure pulse.

Our next empirical model is the Shue model, discussed in chapter II; from this model just the magnetopause standoff distance is plotted to provide an indication of the magnetopause boundary response. As expected by the definition of the magnetopause as the dynamic pressure increases throughout the event the Shue model predicts standoff distance decrease accordingly. The other input to the Shue model

standoff distance is the IMF B_Z that accounts for the hour long extrusion of the standoff distance at 17:00UT on Feb 18 where B_z is negative.

In the same panel with the Shue standoff distance results we have the simulation determined magnetopause standoff distance plotted in magenta for comparison. Clearly the simulation and the Shue model agree very closely in average values, with more small high frequency variations from the simulation results. More detailed comparisons are made in section 3.6.

The last empirical model employed to evaluate this event was the Ridley and Kihn 2004 Cross Polar Cap Potential (CPCP) model. This model uses the Polar Cap Index (PCI), based on data from a magnetometer station in the northern polar cap (Thule station). The cross polar cap potential value represents the maximum potential difference of any two points in the ionospheric polar cap. The representation of this CPCP model makes for another good 1-1 comparison with the simulation because the thin sphere approximation allows for direct evaluation of the max and min potentials in each hemisphere.

The third to last panel of figure 3.3 shows the CPCP from the empirical model as well as from the simulation; again the empirical model and simulation results match fairly well. The CPCP value has units of kV, which is the same as the units of the Newell coupling function (kWb/s), but physically they represent different things. While the Newell coupling function represents the rate of increase in the polar cap flux due to coupling with the solar wind, the CPCP is a measure of the net rate of change of polar cap flux due to both the dayside reconnection (adding flux) and nightside reconnection (removing flux).

Taking the two results together the empirical models predict that nightside reconnection is always present and relatively steady because the Newell function is larger than the CPCP for most of the event. Particularly at the beginning of the second ICME ejecta when the dynamic pressure increases the difference between the Newell

function and the CPCP grows, which indicates stronger nightside reconnection activity. This is corroborated by the AL index peak around the same time. The AL index results will be discussed in the next section.

3.4.3 Geomagnetic Indices

The last two panels of figure 3.3 show two geomagnetic indices. The first is the SYM-H index, which is a one minute version of the Disturbance Storm Time (Dst) index. Both indices represent the average magnetic perturbation of Earth's dipole field and directly reveals the storm phases. This storm begins its main phase at the first ICME ejecta and peaks while in the second ICME sheath. The second ICME ejecta causes more geomagnetic activity as the SYM-H index does not monotonically increase during recovery.

The SYM-H index can also be measured from the simulation results by taking the Biot-Savart integral of the entire (MHD) domain and determining the effective magnetic perturbation at the origin (XYZ=0). This result from the simulation is plotted in magenta for comparison, it matches the observed SYM-H quite well, which indicates the simulation is capturing the global system behavior.

The second important geomagnetic index shown is the Auroral Electroject Lower (AL) index that measures the extreme minimum magnetic perturbation value amongst the magnetometer stations at high latitudes (above 60 degrees). Typically this extreme value is due to nightside field aligned current pairs which close via a hall current across the ionosphere; these currents signify reconfiguration of the plasma sheet and substorm activity. For this event there is strong AL activity during the end of the storm main phase in the second ICME sheath and a large enhancement during the recovery phase at the beginning of the second ICME ejecta (Feb 19 13:00) occurings at the same time as the dynamic pressure pulse.

The AL index can also be directly evaluated in the simulation by seeding virtual

magnetometer stations and taking the minimum value of those virtual stations. The simulated AL index for this event matches the worst of all the 1-1 comparisons; it exhibits the correct response behaviour but does not reach the deep minimum values of the observed AL. This could be a product of the seeded magnetometer locations, since for this index an equally space longitudinal ring of magnetometers were seeded, rather than the true geographical positions. For signals like AL that are driven by the closure of field aligned currents that can be highly localized, small distances between stations can have large impacts in the received signal because the currents can pass almost directly overhead.

3.5 Boundary Location and Motion Results

A fortunate feature of the February 2014 event is the positioning of satellites that can provide comparison points with the simulation for magnetopause crossings; the satellites used for comparison are the Time History of Events and Macroscale Interactions during Substorms (THEMIS), Geotail, and Cluster satellites. Figure 3.4 shows the spacecraft trajectories in the GSM coordinate system with grey shading indicating the ranges of boundary extremes of the bow shock and magnetopause. To determine the extreme locations for these two boundaries the procedure given by the Satellite Situation Center (SSCWeb, *Kovalick* (2023)) is used. For the magnetopause the Roelof and Sibeck 1993 model (*Roelof and Sibeck*, 1993) is calculated using the solar wind conditions propagated from L1, and for the bow shock a modified version of Fairfield's model (*Donald H. Fairfield and Fairfield*, 1971) with a fixed standoff distance ratio between the magnetopause and bow shock of 1.3. From this figure it is apparent that several magnetopause crossings will be available for comparison between the observed satellite data and the simulation results.

Figures 3.5-3.7 show the time series data of the magnetic field measured by the real satellites and the virtual satellites seeded into the simulation domain; these time

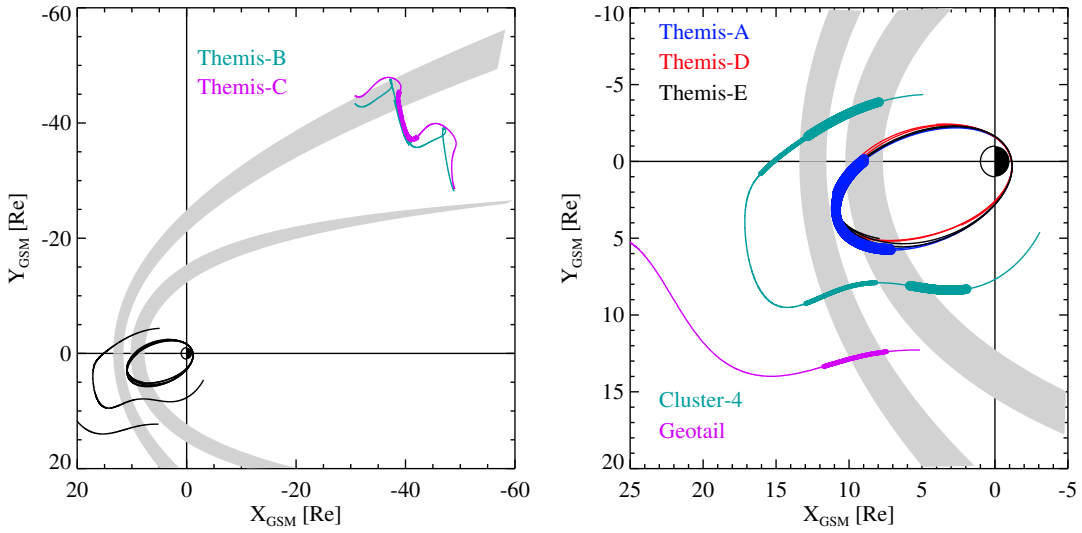

Figure 3.4: Satellite orbits for the spacecraft used for comparison with the simulation during this February 2014 event.

series can reveal the magnetopause crossing locations while providing a continuous comparison between the real and virtual satellites. Key times are marked on the time series; Vertical dashed lines indicate substorm onsets determined by ground magnetometer observations and vertical solid lines indicate sharp changes in the IMF conditions.

Figure 3.5 shows the real and virtual Geotail and Cluster satellites, along with the solar wind magnetic field magnitude plotted again for reference; both satellites spend time in the magnetosheath and the Cluster satellites cross the magnetopause. Geotail starts out in the solar wind moving towards Earth and crosses into magnetosheath around 20:00UT on Feb 19 as indicated by the increase in magnetic field strength above 20nT. Cluster is actually a constellation of 4 satellites but for this event the spacing between the spacecraft was too small compared to the simulation grid resolution for more useful comparisons to be made so only Cluster 4 is used. Cluster 4 begins in the magnetosphere and immediately crosses the magnetopause into the magnetosheath, indicated by the noisy magnetic field strength signal, near 07:00UT on Feb 18. Cluster 4 continues to move out and crosses into the solar

wind around 12:00UT on Feb18. The subsequent magnetic field enhancements in the Cluster 4 timeseries show further bow shock crossings on the outbound path as the magnetopause standoff distance fluctuates, then on the inbound path Cluster 4 passes through the bow shock again as indicated by the strong enhancement in magnetic field strength and its final pass through the magnetopause occurs just after the end of the time series shown.

Figure 3.6 shows the THEMIS B and C probes that are in a lunar orbit for this event, fortunately this orbit still results in bow shock crossings out on the dawn flank. The bow shock crossing is evident in both THEMIS B and C by the fluctuations in magnetic field strength with averages near the IMF values, which is a signature of the foreshock upstream of the bow shock. Later (Feb 19 04:00UT), there is a significant increase of the magnetic field above the IMF value indicating a bow shock crossing into the magnetosheath. Towards the end of the event (Feb 19 14:00UT), the magnetic field strength returns to the IMF level indicating a return to the solar wind, in this case for both virtual spacecraft. This return to the IMF field strength occurs later than the observed signal, which indicates a discrepancy in the simulated bow shock location. This is unsurprising given the coarseness of the grid resolution in this region of the simulation.

The next figure 3.7 shows the THEMIS probes closer to Earth; all three of these space craft experience magnetopause crossings that can be found in the magnetopause crossing database compiled by *F. A. Staples et al.* (*F. A. Staples et al.*, 2020) marked as red vertical lines. Many of these crossings occur in rapid succession, which is a reminder of just how fast the magnetopause can move with respect to the spacecraft that is trying to cross it.

For each of the virtual satellites there is very good agreement with the real satellite magnetic field strength. This close agreement indicates that the bow shock and magnetopause locations observed in the simulation are close to the real boundary

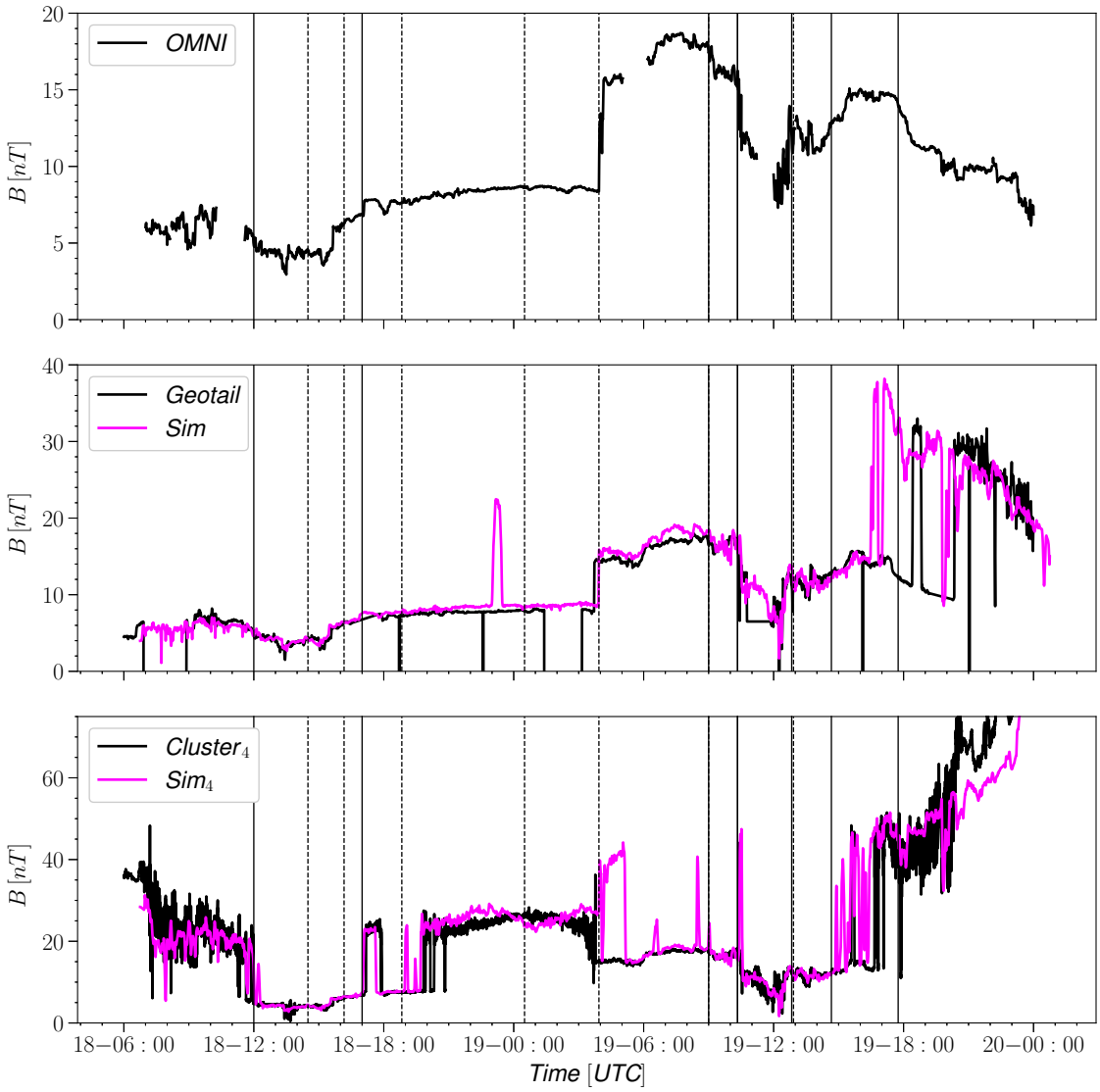

Figure 3.5: Time series of $|B|$ for real and virtual Geotail and Cluster satellites. Vertical lines dashed lines mark substorm onsets; vertical solid lines indicate changes in IMF direction. Solar wind $|B|$ replotted in top panel for reference.

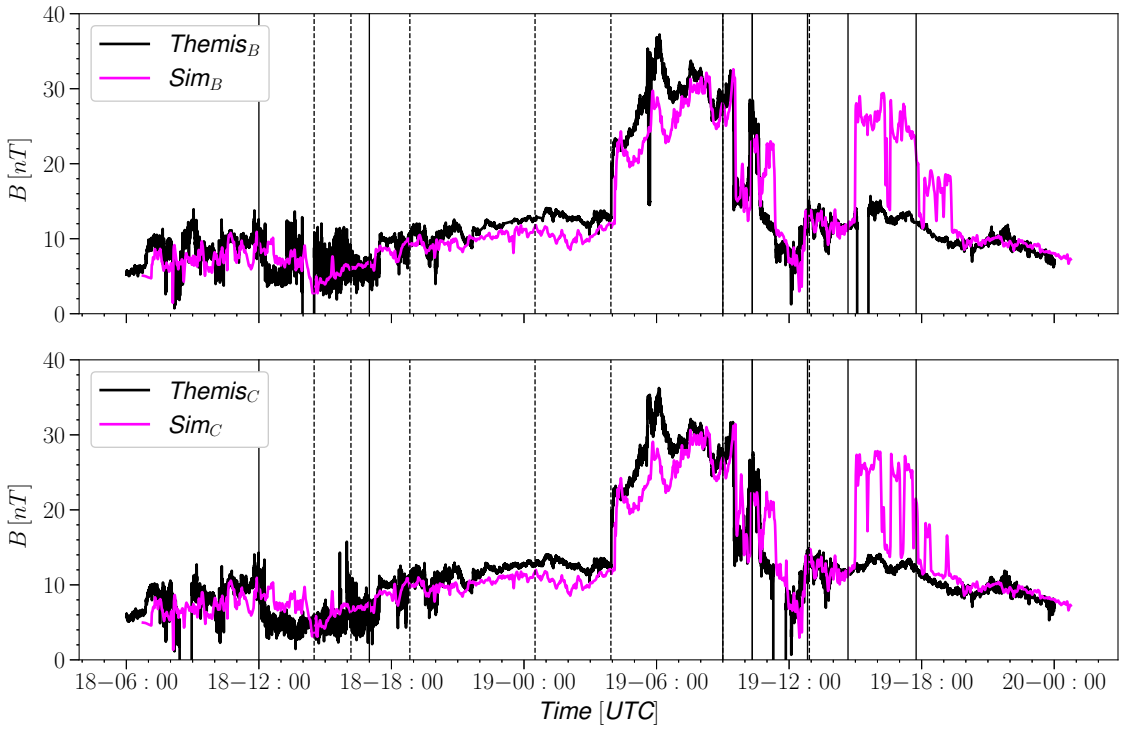

Figure 3.6: Time series of $|B|$ for real and virtual THEMIS outer spacecraft B,C. Vertical lines mark the same times as figure 3.5.

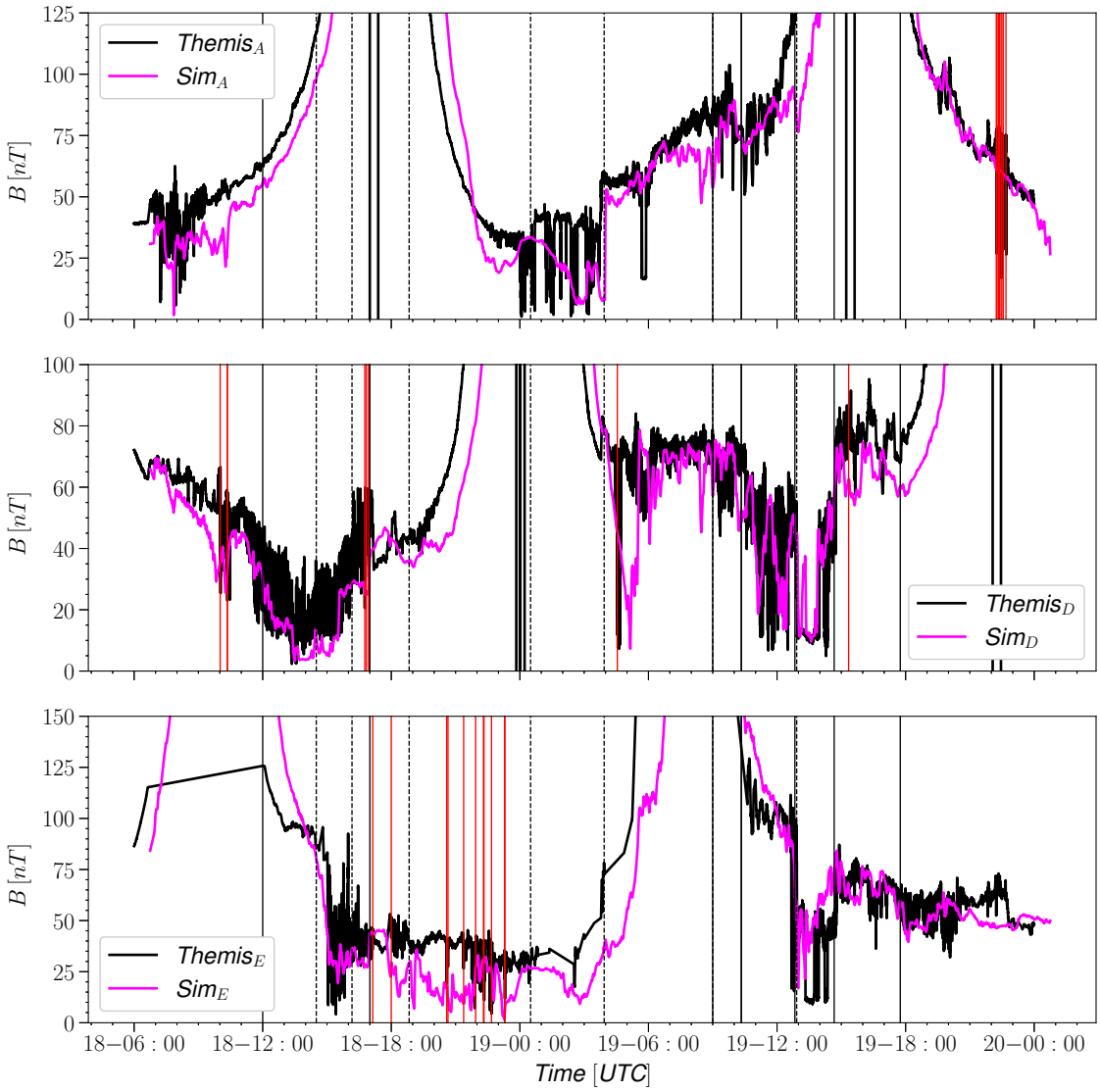

Figure 3.7: Time series of $|B|$ for the real and virtual three interior THEMIS A,D,E spacecraft. Vertical black lines mark the same times as figure 3.5. Vertical red lines indicate magnetopause crossings compiled by *F. A. Staples et al.* (*F. A. Staples et al.*, 2020).

locations. This will be a critical feature given sensitive the energy transport results are to the boundary position. Where the virtual and real satellite magnetic field strengths tend to differ is either away from the inner magnetosphere in the case of the THEMIS B and C probes, or small differences in the timing of the magnetic field strength results. In the limit of the satellite being fixed in place relative to the boundary this amounts to small differences in the boundary motion rather than the overall shape. Most importantly for the cases with verified magnetopause crossings from THEMIS A, D,E we see there is very good agreement in the magnetic field strength during the crossing times.

3.6 Magnetopause Energy transport Results

Now that we broadly understand the Feb 2014 event in terms of solar wind conditions and empirical models, and have shown that the simulated magnetopause boundary is well represented based on the data that is available, we are ready to evaluate the energy transport across the magnetopause boundary. Chapter II covers in great detail how the magnetopause detection algorithm is developed while section 3.2 of this chapter describes the methodology used to conduct the energy transport analysis.

Figure 3.8 shows the total energy transfer through the magnetopause surface including boundary motion effects split by energy injection (negative) and energy escape (positive) with the net transport shown as a fill value that may be either positive or negative; the three panels then further split the results into total energy flux (panel 1), Poynting flux (panel 2), and hydrodynamic flux (panel 3). From the top panel we can see that there is a significant amount of energy both injecting and escaping through the magnetopause surface and thus the net energy transport is only a fraction of what is brought in through the boundary. Figure 3.9 shows the results from a single output file at 05:45UT on February 19 giving the full distribution of energy flux across the cells on the magnetopause surface.

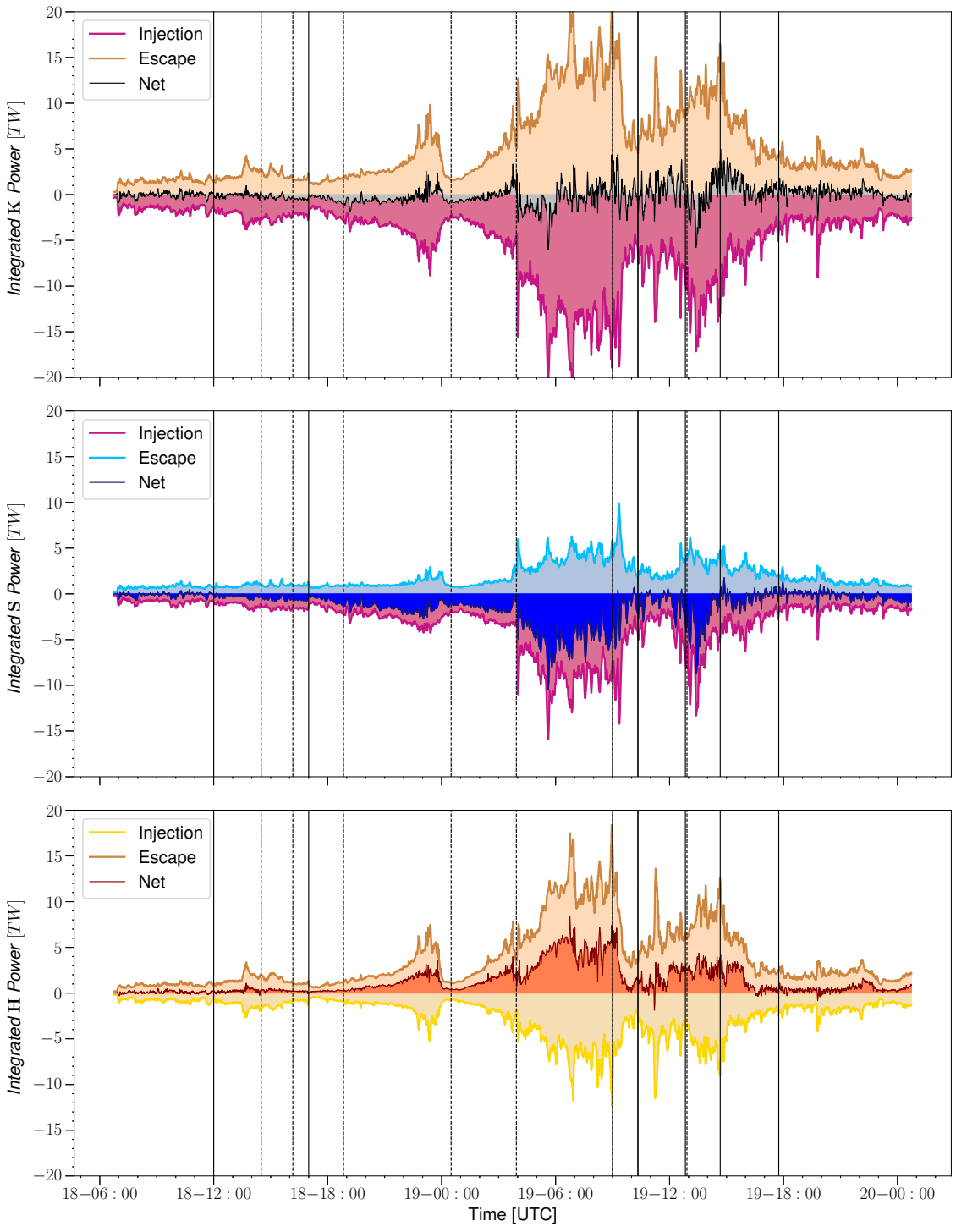

Figure 3.8: Surface integrated energy transport through the magnetopause including boundary motion effects. Positive is energy escape (unit normal points out from enclosed volume) and negative is energy injection, with net values as the sum. Top panel is integrated total energy flux, middle panel is integrated Poynting (magnetic) energy flux, and bottom panel is integrated hydrodynamic (thermal + kinetic) energy flux. Vertical lines mark the same times as figure 3.5.

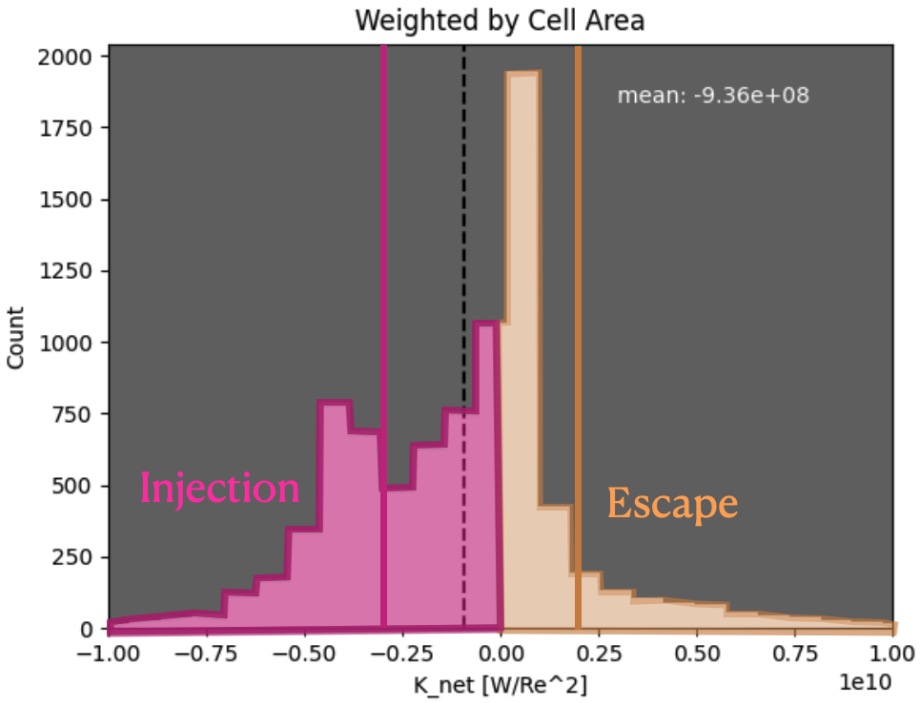

Figure 3.9: Snapshot at Feb 19 - 05:45UT of total energy flux across the magnetopause surface cells showing balance of energy injection and escape.

In terms of energy type we see that during the main phase of the event when most net energy is injected through the magnetopause most of the injected energy is in the form of Poynting flux (panel 2, magnetic energy) while most of the energy escaping the system is hydrodynamic flux (panel 3, thermal and kinetic energy). Additionally we see that both the injections and escapes are enhanced when the incoming solar wind magnetic energy is increased (higher IMF magnetic field strength) and kinetic energy is increased (higher dynamic pressure).

To determine how much of the net energy transport (grey fill panel 1 figure 3.8) is due to the surface motion we next split this motional contribution and plot it along side the total for comparison. This comparison is shown in panel 2 of figure 3.10. Unlike the static energy transport, which exhibits a balance between escape and injection, the motions of the magnetopause although rapidly changing sign has an unbalanced transport. This unbalanced nature means that the boundary motion

contributes significantly to the net energy transport.

To see how the motional net energy transport is affected by the solar wind we compare the time series with the solar wind dynamic pressure in panel 1 of figure 3.10. As the solar wind pressure fluctuations pick up in the second half of this event we see stronger fluctuations in the net motional energy transport as well. While the fluctuation amplitude increases, the large scale signatures in solar wind dynamic pressure are not reflected in the motional energy transport time series, indicating that it is not simply the whole system being squeezed or expanded, which yields the motional energy transport.

While the dynamic pressure alone cannot explain the motional energy transport time series, it is strongly anti-correlated with the integrated magnetosphere volume. Using a simple dimensional argument based on the standoff distance - pressure relationship of the Shue model ($r = P^{-1/6.6}$) the volume and pressure should scale linearly when the volume is raised by a factor of -2.2 ($V^{-2.2} = r^{-6.6} = P$). Performing this calculation yields a Pearson correlation coefficient between the scaled simulated magnetosphere volume and solar wind dynamic pressure of 0.65.

Considering that rapid changes and local deformations in the magnetopause surface could yield motional energy transport we plot the enclosed volume of the simulated magnetosphere along with the volume enclosed by the axisymmetric Shue model magnetopause for comparison. Panel 3 of figure 3.10 shows that for the first 12 hours of the event the simulated magnetosphere volume is smaller than the Shue volume. Then as the two volumes intersect there are two subsequent 3 hour periods of volume expansion and contraction in the simulated magnetosphere. While the volume is increasing there is steady injection of energy due to the motion (panel 2 figure 3.10 magenta curve is negative) and when the volume decreases the motional energy flux reverses.

Investigating the two large volume oscillations closer; there appear to be both

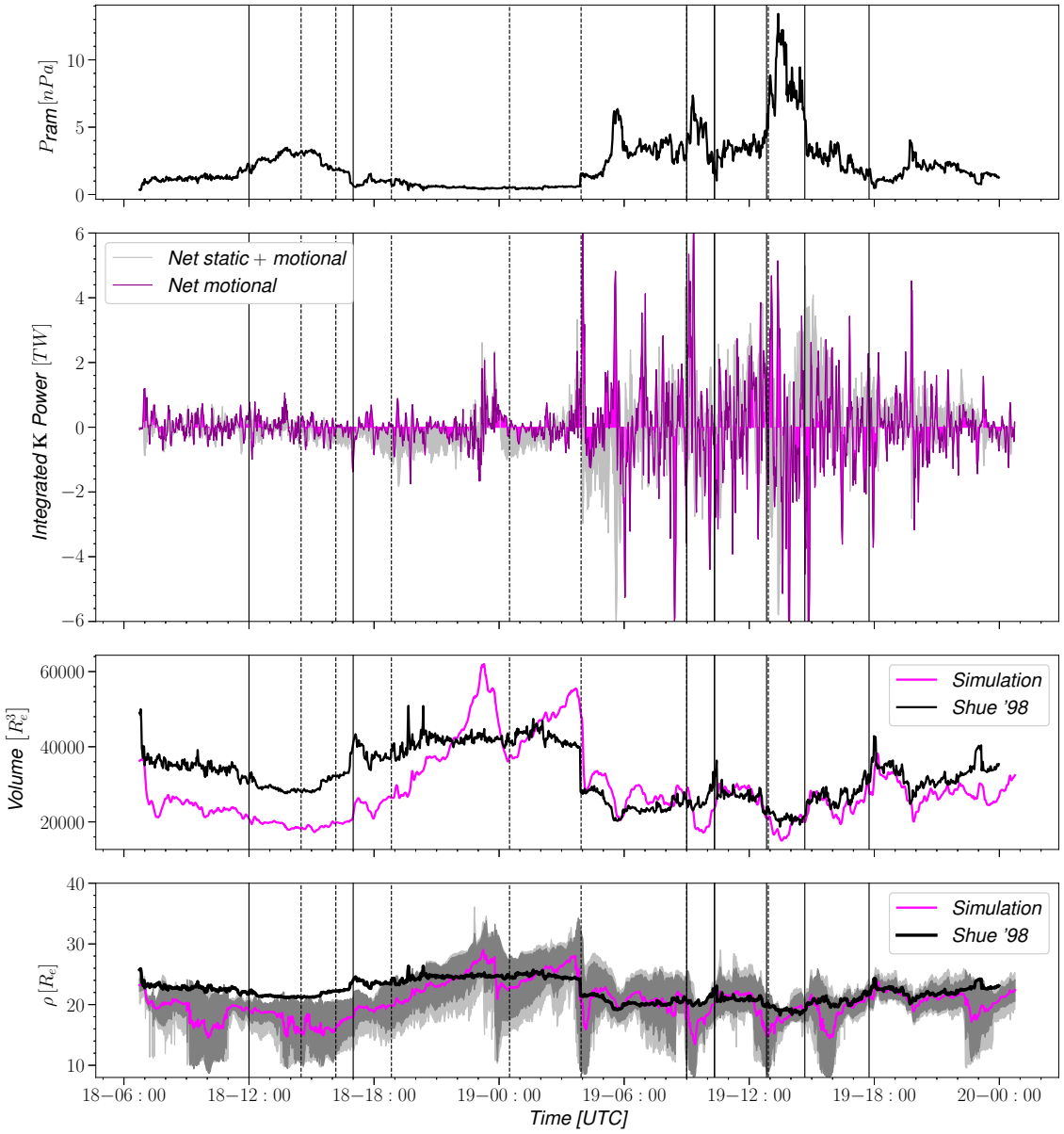

Figure 3.10: Top panel- solar wind dynamic pressure, second panel- magnetopause surface integrated net total energy (grey) compared with surface motion contribution (magenta), third panel- magnetosphere volume enclosed by magnetopause from simulation and Shue 1998 model, and last panel- $X = -10$ distribution of radial distance to the magnetopause in YZ plane with simulation bounds in grey, $+-1.5\sigma$ in dark grey, mean in magenta and Shue 1998 model in black. Vertical lines are the same as previous figures.

external and internal driving mechanisms. The second oscillations sharp volume decrease (Feb 19 04:00UT) corresponds with a sudden increase in IMF magnitude and solar wind dynamic pressure. The first oscillation (Feb 18 22:00UT), on the the other hand, occurs entirely during steady solar wind conditions. This lack of solar wind input signal indicates that the change from increasing to decreasing volume occurs due to an internal triggering mechanism rather than an external driving signal from the solar wind.

In order to study the way in which the simulated magnetopause surface deviates from an axisymmetric profile the last panel of figure 3.10 shows results of the tail cross section at X=-10Re; the radial distance $\rho = \sqrt{Y^2 + Z^2}$ is a single value for the axisymmetric Shue profile and a distribution of values for the simulated magnetopause surface. The average simulated magnetopause ρ is plotted as the magenta curve, the average simulated ρ and the Shue model ρ behave similarly to the volume results. The distribution of ρ values, however, reveals that the simulation magnetopause profile is experiencing local changes that break symmetry as evident by the span of maximum and minimum values (grey shading) and $+-1.5$ standard deviation of values (dark grey shading) being uneven with respect to the mean value.

Because there is simultaneous energy injection and escape there must be spatial variation in the static energy transport through the magnetopause surface; we explore this by plotting the energy transport across Day, Flank, and Tail sectors of the magnetopause. For the results shown in figure 3.11, the Day sector represents everything $X > 0$, the Tail sector is the local X_{min} points with surface normal to the tail cutoff plane. These elements are mostly at $X = -20$ but also include any interior surface due the near tail reconnection line moving with in $20R_e$. The Flank is the remaining surface area on the exterior of the surface between $X = 0$ and $X = -20$. The top three panels of Figure 3.11 represent integrated total flux, Poynting flux, and hydrodynamic flux like figure 3.8, but now instead of injection and escape the

integrated energy flux is represented as stack plots first of the Day transport, then the Flank transport, and finally the Tail transport.

Panel 1 showing the integrated total flux stack by region reveals a clear competition between the Day sector and Flank sector with very small contribution from the Tail sector. For each of the sectors there is contribution to both energy injection (negative stack) and escape (positive stack) indicating that there is flux variation within each of the sector surfaces. We also see a clear change in the stack contributions from the Day sector to the Flank sector around 06:00UT on Feb 19 as the total escaping flux (top positive level) remains steady while the split between Day and Flank changes.

Panels 2 and 3 show the same results now for integrated Poynting flux and Hydrodynamic flux; it is clear from these panels that each of the sectors experience some of each type of energy flux in each direction. The sharp swap from Day to Flank integrated flux escape occurring at 06:00UT on Feb 19 is in the form of hydrodynamic flux based on panel 3. Except this period between 06:00UT and 09:00UT the Day sector contributes more strongly to hydrodynamic energy escape, while the Flank sector contributes more significantly to Poynting flux injection.

Panel 4 presents stacks of the integrated total energy flux for each sector now as a ratio of the total to more clearly show how the relative contributions shift. In this view it is now clear that the Tail sector contributes at most 10% to the integrated energy flux at any point during the event. There are several sharp changes in the relative contribution between the Day and Flank sectors. The first two occur at the same time as the volume oscillations seen in figure 3.10, which indicates that the volume expansion and contractions are occurring in the Flank sector (more surface area = more integrated surface flux). The last major change occurs at 06:00UT along with the entire magnetopause compression. Because the Day Flank cutoff is fixed at X=0, when a global compression is applied the surface area shrinks and is shifted

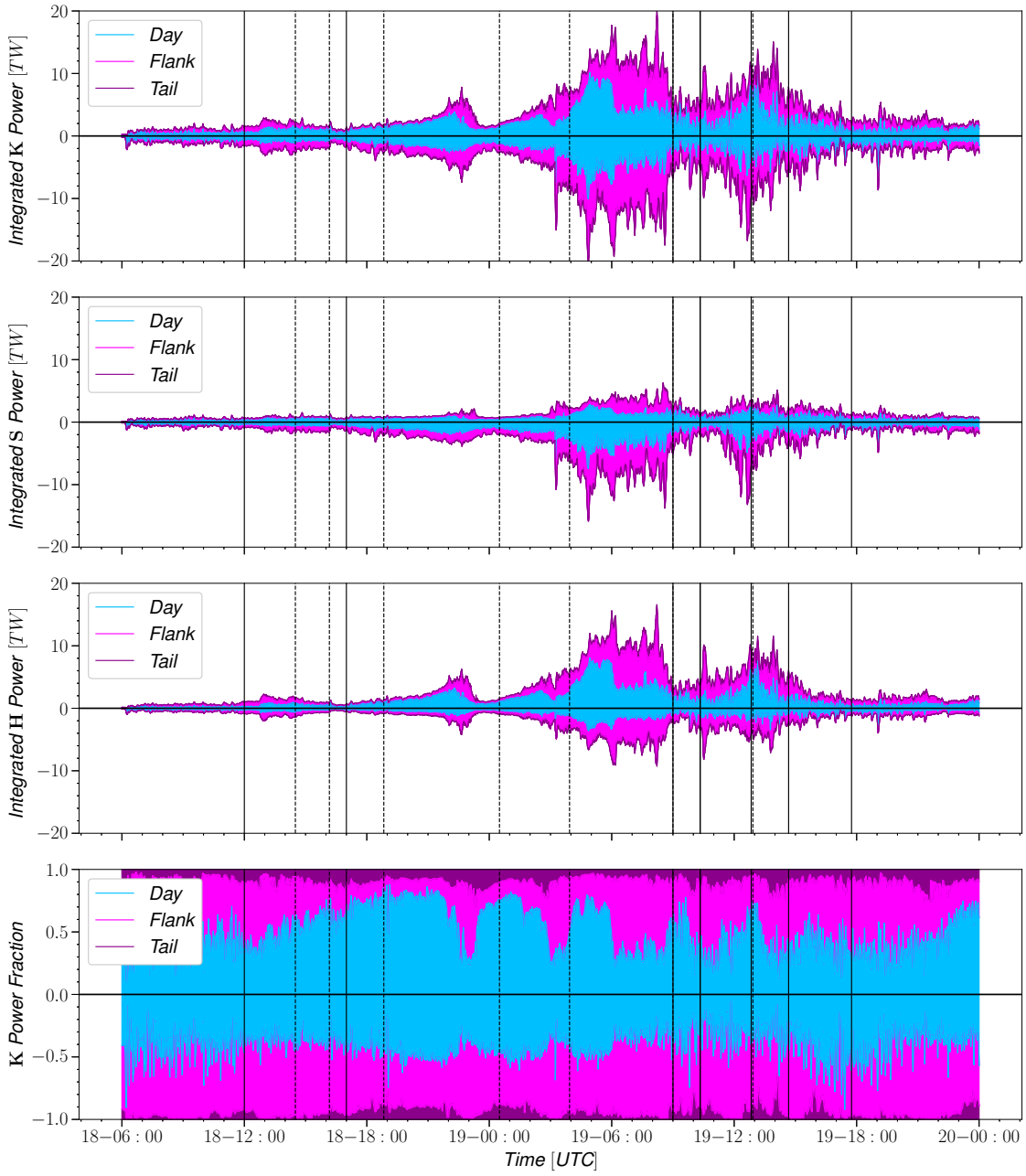

Figure 3.11: Surface integrated energy transport stacked by region. Top panel 1: integrated total energy flux injection and escaped stacked Day, Flank, Tail. Second panel 2: integrated Poynting flux. Third panel 3: integrated hydrodynamic flux. Bottom panel 4: percentile of total for top panel values (integrated total energy flux K).

with the direction of flow so there is a higher proportion of area located past X=0. In addition to the longer lasting periods of high Flank relative contributions, there are also more rapid fluctuations. These fluctuations are on the order of minutes, which is the same timescale at which plasma is advected along the magnetopause surface from +10 to -20 R_e, and may indicate solar wind being advected from the Day to the Flank sector.

3.7 Discussion

This study uses a newly developed magnetopause detection methodology to study a real event using simulation results. First the event is evaluated using observation results (empirical models, geomagnetic indices, and spacecraft data) to baseline the expected behavior of the storm and validate the simulation results where data is available. At this time empirical models and spacecraft data are insufficient to quantify the global energy transport dynamics, although coupling functions like that of *Newell et al.* seek to capture those dynamics using the solar wind conditions alone.

When the energy flux was integrated across the simulated magnetopause surface it was found that there is always a balance of energy being injected and escaping through the system. By type of energy it was found that magnetic energy in the form of integrated Poynting flux was primarily injected while thermal and kinetic energy in the form of integrated hydrodynamic flux was primarily escaping the magnetopause surface. Furthermore it was found that most Poynting flux was being injected in the Flank sector ($X < 0$) while hydrodynamic flux was escaping in the Day sector ($X > 0$).

The Poynting flux transport pattern on the magnetopause surface fits with the textbook magnetic topology shown in chapter II, where open flux in the lobes has magnetic field normal to the magnetopause surface that allows for energy transport in the opposite direction of the magnetic field proportional to $\mathbf{u} \cdot \mathbf{B}$. This portion of

the Poynting flux has the form $\left(-\left(\frac{\mathbf{B}\cdot\mathbf{u}}{\mu_0}\right)\mathbf{B}\right)$.

On the dayside magnetopause where the magnetic topology is closed, there is velocity in the sunward (positive X) direction inside the magnetosphere approaching the dayside magnetopause boundary that transports both types of energy $\left(\left(\frac{1}{2}\rho u^2 + \frac{1}{\gamma+1}P_{th} + \frac{B^2}{\mu_0}\right)\mathbf{u}\right)$. As the sunward edge of the dayside magnetopause closed topology reconnects and is no longer part of the magnetosphere it moves away from the magnetopause surface to join the magnetosheath and travel downstream, this motion must have its velocity component normal to the magnetopause surface point away from the surface. This is because the plasma that has a newly reconnected field line frozen into it experiences curved magnetic field that causes a tension force that seeks to straighten it out, which in this case moves the plasma in the sunward direction. Because of the internal convection inside the magnetosphere and the magnetic tension forces outside the magnetosphere, the plasma velocity is sunward on both sides of the magnetopause boundary (where reconnection is occurring). This sunward velocity explains how hydrodynamic flux is escaping from the magnetopause Day sector.

This same outward flux of energy at the dayside magnetopause can also be visualized from the polar cap using some simple dipole projections of the geometry. For the portion of the polar cap that is actively reconnecting on the dayside the closed field is becoming open field, representing an expansion of the polar cap down to lower latitudes. This additional magnetic flux is therefore transported from the closed field to the open field moving from lower to higher latitude. Considering this same direction projected from the ionosphere down to the equatorial plane it is clearly seen as sunward flow of magnetic flux. Because the flux is frozen into the plasma this will also transport hydrodynamic flux sunward with the bulk velocity.

The results of hydrodynamic energy outflow differ from previous findings ((*Palmroth et al.*, 2003), (*Lu et al.*, 2021), (*H. Zhang et al.*, 2023)) due to the construction of the magnetopause surface. Since the magnetopause surface used in this work is based

on magnetic topology on the dayside the outflow of hydrodynamic flux is seen. With a surface based on the flow field of the plasma a boundary further sunward from the last closed field line will be found that in turn will yield velocities on the surface that point with the magnetosheath flow (anti-sunward). This additional hydrodynamic flux injection through the flow-field defined magnetopause is balanced by the outflow along the enlarged tail cutoff plane as the magnetosheath flow moves past the Earth.

It is important to note that this dayside energy out flow can in fact appear as STATIC outflow in this analysis. While it is true that the physics behind the development of the sunward flow are that of dayside reconnection driven erosion of the closed magnetic topology, the surface location changes extremely little because the magnetopause dayside surface location is determined by pressure balance. If the upstream magnetosheath pressure does not change then the balance point location will remain almost the same. Considering the pressure balance from the magnetosphere side is almost entirely magnetic, the magnetic field will compress until the magnetic pressure reaches the amount required, in this highly compressed state stripping off a small amount of magnetic flux will have only a small change in pressure balance location. Furthermore, as dayside magnetic reconnection continues the internal magnetic pressure becomes supported partially by the increased ring current thermal pressure. Because of these properties the change in the dayside volume between two time steps used to evaluate the motion contribution may not capture any perceptible change.

It may be clear to the reader at this point that the magnetic topology is a key factor in the energy transport process at the magnetopause, unfortunately for this work the surface was not broken down in this way to make a clear comparison. In the next chapter, the energy transport at the magnetopause boundary is studied in relation to the magnetic topology explicitly to test the conclusions drawn from this study.

Finally, an important finding of this study was that the surface motion contri-

bution to the total energy flux needs to be included. Based on the results of figure 3.10 there are significant contributions to the net energy flux due to the motion of the magnetopause boundary, especially at times when the surrounding solar wind environment is at an elevated energy density.

CHAPTER IV

A New Approach: Dissecting the Magnetosphere

4.1 Introduction

In this chapter we expand our analysis to look at energy transport not just at the edges of the magnetosphere through the magnetopause, but within the system and between the two major regions of the magnetosphere: the closed magnetic topology closed region and open magnetic topology lobes. This work has been accepted and is presently in the process of being published (*Brenner et al.*, 2023).

Moving off the equatorial plane another key place to consider for internal magnetosphere energy transport is in the cusp. Throughout recent decades the Cluster spacecraft constellation has made many observations of the magnetic cusp ((*Escoubet et al.*, 1989), (*Lavraud et al.*, 2005a), (*Lavraud et al.*, 2005b)) in particular it was found that the direction of plasma motion at the cusp is dependent on the relative location of the dayside reconnection to the cusp. Figure 4.1 adapted from *Pitout et al.* (2021) illustrates this concept.

A special case of cusp dynamics is the so called dual lobe reconnection, in which both the north and south lobes experience magnetic reconnection during due northward IMF and become closed topology. Work by *Milan et al.* (*Milan et al.*, 2020) has shown evidence for dual lobe reconnection based on ground based observations of the ionosphere.

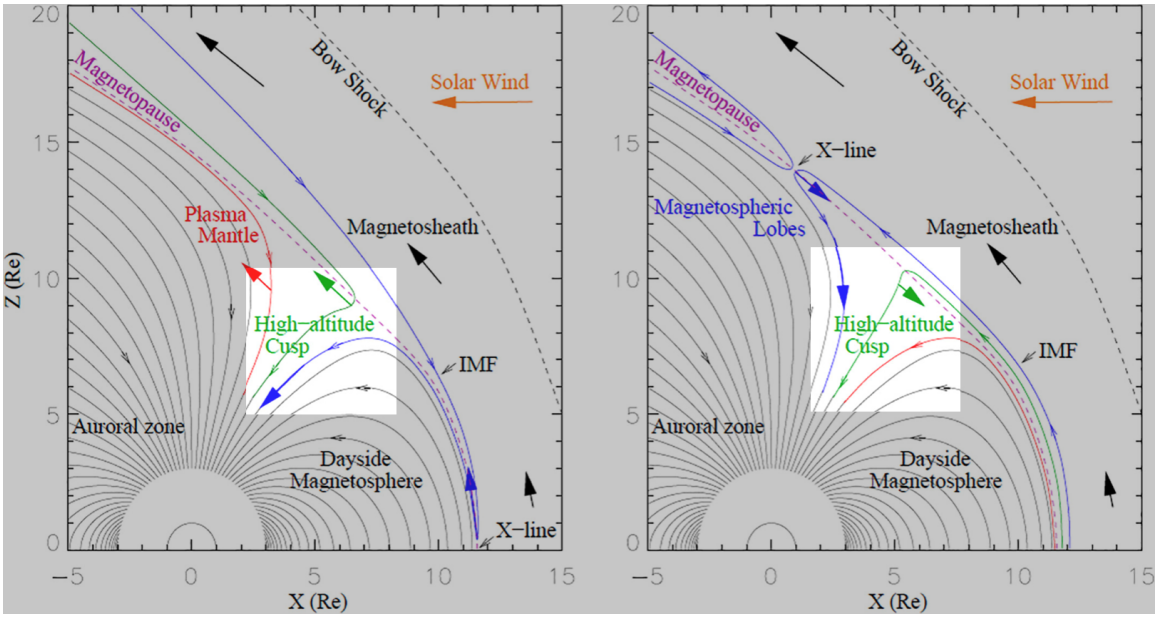

Figure 4.1: Illustration of plasma flow at the cusp during southward IMF (left) and northward IMF (right); as the reconnection line (X-line) moves to the other side of the cusp in the latitudinal direction the flow direction (green arrow) reverses. Figure adapted from *Pitout et al.* (2021).

The last consideration for how we expect energy to transport is with mass flux from the inner boundary. *Glocer et al.* (*Glocer et al.*, 2020) showed results whereby using a polar wind outflow model, much of the mass in the magnetosphere could be populated by flow from the inner boundary. The physical phenomena of polar wind outflow is not directly modeled in the geospace configuration of the space weather modeling framework, but work by *Welling and Liemohn* (*Welling and Liemohn*, 2014) have shown how numerical diffusion from the inner boundary mimics this effect so we expect some energy injection from the inner boundary to the magnetosphere.

4.2 Methodology

The analysis techniques used for this study build on the previous study covered in chapter III, but now with an expanded set of boundaries that focus on looking inside the interior of the magnetosphere. Starting with the same magnetopause definition

from III this boundary separates the magnetosphere from the surrounding magnetosheath and solar wind and forms a closed volume. The only modification made to this magnetosphere definition is to cut out a sphere at $r = 4R_e$. The inner boundary of the simulation goes in to $2.5R_e$ but by keeping the analysis limited to $r > 4R_e$ boundary condition effects are minimized. At this point there are now two interfaces of interest, one that is the magnetopause surface between the magnetosphere and the sheath and the other that is the inner boundary between the magnetosphere and the region that couples to the ionosphere.

With the magnetosphere now defined as the space between the magnetopause and an inner analysis boundary at r=4Re we study internal energy transport by dissecting the magnetosphere according to two types of magnetic topology: open and closed, and the mapped ionospheric longitude dayside and nightside. This splits the magnetosphere volume into 4 regions (closed daymapped, closed nightmapped, open daymapped, open nightmapped) and the magnetopause surface into 4 regions (closed - sheath, lobes - sheath, closed - tail cutoff, lobes - tail cutoff). For simplicity the day-night mapping is not differentiated for the magnetopause or inner boundary interfaces because the transport mechanisms should be identical. The last interface (lobes-closed region), is split according to day or night ionospheric mapping. The dayside mapped portion of this open-closed interface represents the magnetospheric cusp region while the nightside mapped portion represents the plasma sheet boundary layer. Figure 4.2 shows a schematic of the magnetosphere system in the XZ plane with regions and interfaces labelled.

To summarize: cells in the simulation output can belong to one of six regions at any given time. I Exterior, outside the magnetosphere including solar wind and magnetosheath, II daymapped closed field region, III daymapped lobes, IV nightmapped lobes, V nightmapped closed region, and VI Interior outside of the region of analysis. Using these 6 definitions the motional contribution of each surface can be evaluated in

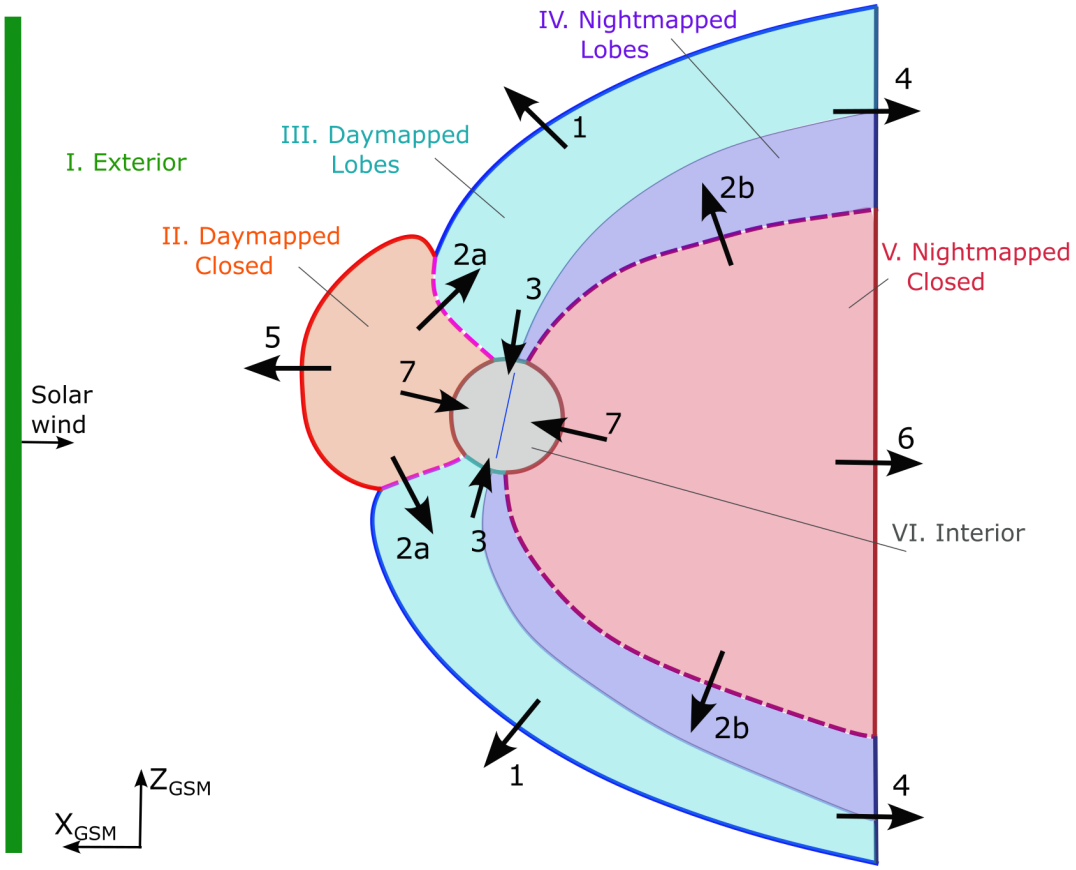

Figure 4.2: Diagram of the magnetosphere in the XZ GSM plane. Six volume regions are labeled with interfaces between them shown with arrows indicating the flux calculation reference direction. For all boundaries except 2a and 2b reference vectors point outward from the the magnetospheric regional volume. For 2a and 2b the vectors point out from the closed region volume (II. and V.).

a similar way to equations 3.6 and 3.7 but generalized to each volume trade between two regions. For example when the dayside closed region is eroded by reconnection a small portion of the daymapped closed region (II) may become Exterior (I) while some volume just outside changes from exterior (I) to either daymapped lobes (III) or nightmapped lobes(IV); this example is sketched in figure 4.3. In this circumstance the volume lost from the daymapped closed region (II) would be considered energy escape through the closed region - sheath interface (+ flux through interface 5) and the volume gained by the day or night mapped lobes (III or IV) is considered energy injection through the lobes - sheath interface (- flux through interface 1).

Figure 4.2 also shows the surface flux vector directions explicitly for clarity. In general the surface fluxes point away from the interior of the bounded volume of interest, but in the case of the internal open-closed interfaces (2a and 2b) the closed region is considered to be the region of interest.

Not pictured in figure 4.2 are two additional interfaces that are defined as the intersection of the $X = 0$ plane with the closed region volume, split into + and - Ygsm. This simple static interface tracks the internal motion of energy as it crosses the $X = 0$ plane on either the dawn side (-Y) or dusk side (+Y), and is used to complete the energy cycle analysis.

Once the volumes and interfaces are determined the energy flux integration analysis is performed in the same way as in chapter 2.6. The energy flux is integrated over the interface surface, accounting for motional effects, and split by direction (injection, escape) and type (Total energy flux, Poynting flux, and Hydrodynamic flux). Additionally the volume integrated energy density is also calculated to understand how energy is stored and passed between regions of the magnetosphere according to equation 4.1 where $\mathcal{V}$ is the regional volume, U is the total energy density, U_{mag} is

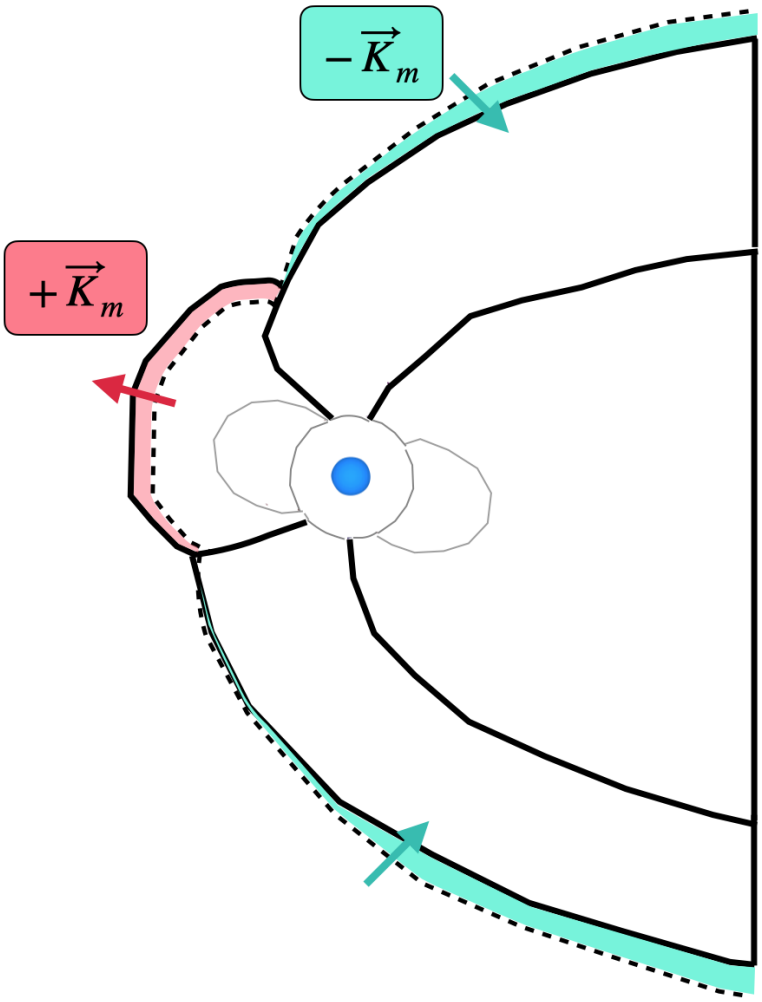

Figure 4.3: Diagram demonstrating motional flux contribution. In this demo reconnection erodes the dayside closed region (II), which is considered + flux ($+\vec{K}_m$) transporting away from the magnetosphere, while the daymapped lobes region (III.) is gaining volume and energy, which is considered - flux ($-\vec{K}_m$) towards the magnetosphere.

magnetic energy, and U_{hydro} is thermal plus kinetic energy.

$$Energy = \int_{\mathcal{V}} U d\mathcal{V} \tag{4.1}$$

4.3 Event Description

The event selected for this study is the well known Starlink event from Feb 2-5 2022, during which 38 commercial satellites from the Starlink constellation were lost due to density upwelling in the thermosphere (*Zhang et al.*, 2022). Because the event is recent we are able to compare our simulation with the latest ground based and space based observational assets.

A unique feature of the Starlink event was its significant impact to human infrastructure despite being a relatively mild storm. The mildness of this storm can be seen in figure 4.4, the top two panels show relevant solar wind parameters and the bottom two show observed geomagnetic indices. Jumping right to panel 3 we see the observed SYM-H index for this event barely reaches -75nT; in storm classification -50nT is considered the minimum threshold to be considered a storm, while the most powerful storms can cause perturbations of more than -300nT. The important feature of this mild storm is not that it caused abnormal conditions in the magnetosphere, but rather that even very typical conditions like this one can have significant impacts on our space technology.

The simulation period for this event last for 40 hours, all time series for this study display time as relative to the end of the storm main phase (t0) with the main phase marked as the shaded interval from -08:00 to 00:00. The storm main phase start corresponds nicely with the southward turning of the IMF (negative Bz), and there is a strong rotation in the IMF By component as well. At the end of the main phase there is a sharp peak in the dynamic pressure shown in panel 2, and the recovery phase (>00:00) is marked by increased plasma β (ratio of thermal to

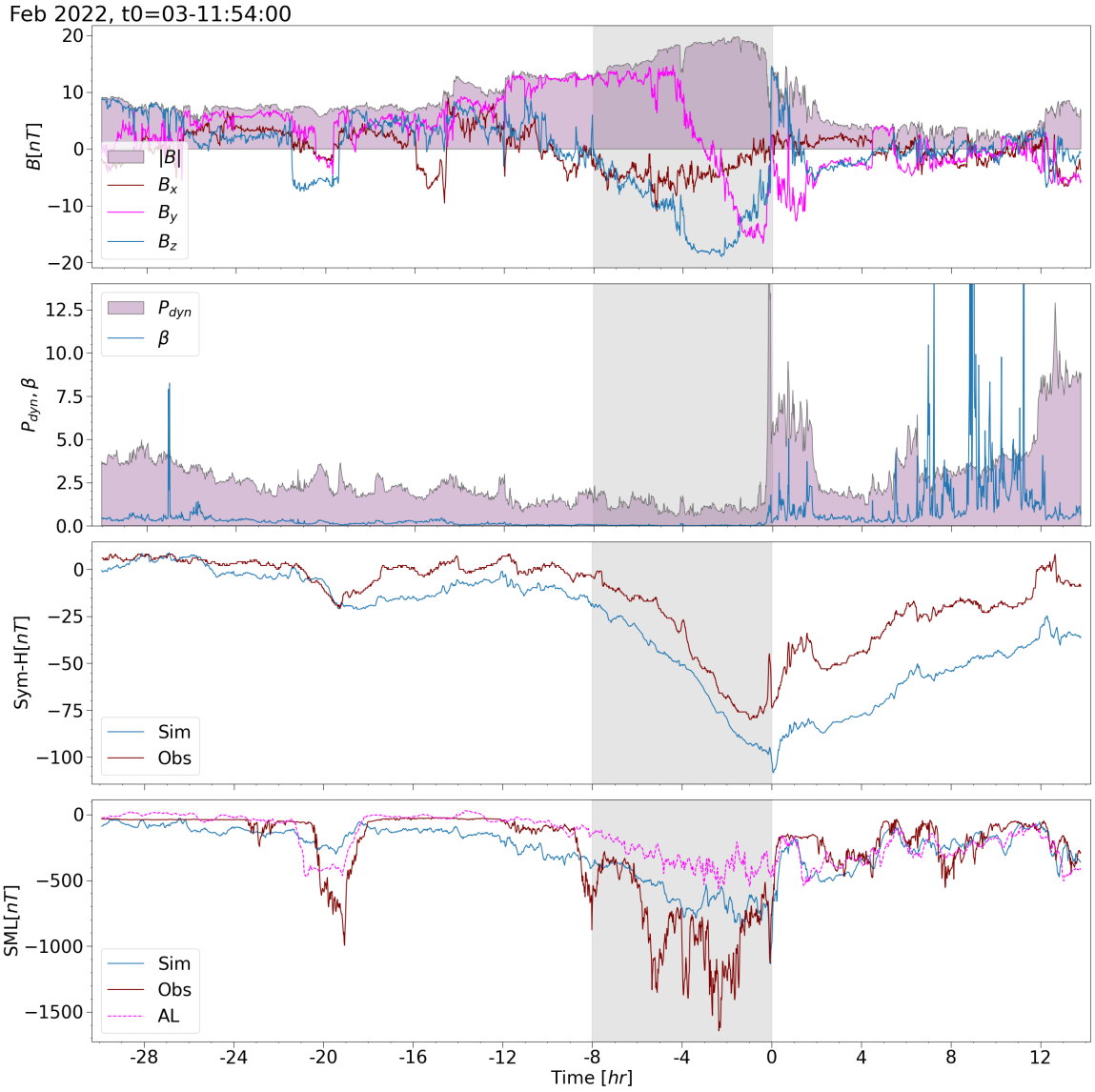

Figure 4.4: Solar wind conditions and geomagnetic indices for Starlink event on February 2-5, 2022, grey shading indicates storm main phase with time axis relative to main phase end. Top panel shows solar wind IMF components and magnitude (filled), second panel shows solar wind dynamic pressure (filled) and plasma β (blue). Third panel shows SYM-H index with simulation results in blue and observations from Omni (`https://omniweb.gsfc.nasa.gov/form/omni_min_def.html`) in red. Bottom panel shows 1-1 comparison of Supermag SML index (blue simulation, red observation) with simulation AL index shown in magenta dashed line for reference to the older electrojet index.

magnetic pressure) above the extremely low β values before and during main phase. This dynamic pressure increase causes an increase in the observed SYM-H index due to the compression of the magnetopause resulting in positive magnetic perturbation.

For this study the Supermag Lower (SML) index is used, which is a variation of the Auroral Electroject Lower (AL) index, using more magnetometer stations it can capture more localized perturbations from the field aligned currents (*Gjerloev*, 2012). During the main phase of this storm (-08:00 to 00:00) there is the highest SML activity, other than the isolated substorm between -21:30 and -18:30.

Next we will compare how the simulation captures the geomagnetic index response and satellite time series data.

4.4 Simulation Setup

For this study we use the Space Weather Modeling Framework in the Geospace configuration (GM-IE-IM components). The Global Magnetosphere model is BATS-R-US in Ideal MHD mode, the Inner Magnetosphere is the Rice Convection Model drift kinetic code (*Toffoletto et al.*, 1996) and the Ionosphere Electrodynamics model is the Ridley Ionosphere Model thin shell potential solver (*Ridley et al.*, 2004).

The updates to the simulation setup compared with chapter III is in the grid resolution and ionospheric conductance model. The finest grid resolution of $1/8R_e$ is expanded to a sphere of radius $8R_e$, and the paraboloid shape to encapsulate the magnetopause is set to $1/2R_e$. The ionospheric conductance determines the relationship between the local conductance and the field aligned currents that come from the Global Magnetosphere component down to the ionosphere grid. The conductance pattern directly impacts the resulting electric potential solution. The update made to this ionospheric conductance relationship is to use the Conductance Model for Extreme Events (CMEE) (*Mukhopadhyay et al.*, 2020). This conductance model is still an empirical fit to observed data, but with an improved set of data that covers

a broader range of conditions.

4.5 Observation comparisons

Like for the study in the previous chapter we use both ground based and space based observations to evaluate the quality of the simulation results; for the ground based comparisons the simulated SYM-H and SML indices are shown in the blue curves of the bottom two panels of figure 4.4. For the SYM-H index the simulation overpredicts the magnetic perturbation, which indicates that there is more energy in the simulated magnetosphere than what is observed. Additionally, there is a sharp discrepancy in the observed and simulation results at the end of main phase (00:00), when the observed SYM-H sharply increases while the simulated SYM-H sharply decreases. We will explore the simulation results around this time in detail when looking at the form of the energy transport results.

For the SML index comparison we see the simulation now underpredicts the SML perturbations, especially during main phase when there are sharp peaks and recoveries. Unlike the simulated AL index, the simulated SML index improves upon the comparison technique by seeding magnetometers at the actual geographical locations in order to make a more 1-1 comparison with the observed data. To illustrate just how different the simulated SML and simulated AL signals can be the AL is plotted for the same event. Clearly the updated simulated index outperforms its predecessor, except in the first isolated substorm (-21:30 to -18:30). The deviation for this isolated substorm indicates that the simulation resolved field aligned currents that caused a perturbation but that the specific location where they appeared was different in space and time than the observed perturbation.

For space based comparisons the Cluster, MMS, and THEMIS spacecraft were used; figure 4.5 shows the orbits for each of the three spacecraft missions with only one of the spacecraft shown for both cluster and MMS (MMS1,Cluster4) and three probes

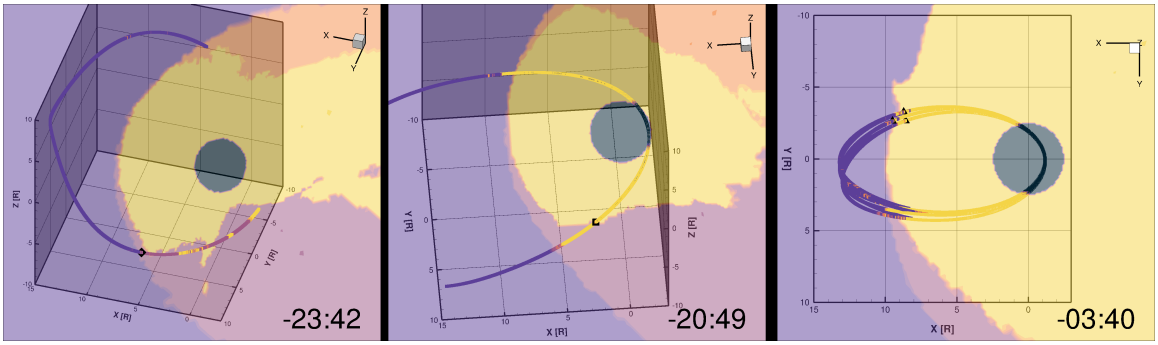

Figure 4.5: Virtual satellite orbits for Cluster (left), MMS (middle), and THEMIS (right) plotted with magnetic topology variable contouring the orbit trajectory. Yellow: closed-closed topology, orange: open-north, and red: open-south. A plane cutting through the orbit is also shown with the contours of same topology variable at the timestamps indicated in each frame (00:00 is the end of main phase on 3 Feb 2022 at 11:54).

shown for THEMIS (A,D,E). The tracks shown are the virtual spacecraft positions traced in the simulation domain for the 40 hour simulation window with a slice through the orbital plane contoured with the simulation topology variable. Purple is open-open, yellow is closed-closed, and the orange and magenta are open-north and closed-south respectively. The orbital tracks are plotted with the same topology variable illustrating the key locations where the virtual satellite changes magnetic topology, which will be the key comparison points for studying the magnetospheric boundaries. (To clarify between the two types of open topology I will refer to north lobe topology as open-north, south lobe topology as open-south, and unconnected topology as open-open).

Figure 4.6 shows the time series of the virtual and observed satellites for each of the five spacecraft; the interval shading indicates the virtual spacecraft magnetic topology again. Now blue is open-north and closed-south, red is closed-closed, and grey is inside the inner boundary (r<2.5Re); unshaded indicates open-open topology.

The top five panels show the IMF Bz and derived Poynting flux while the next five panels show the combined thermal and kinetic pressure along with the derived Hydrodynamic flux; these time series allow for identification of the boundary cross-

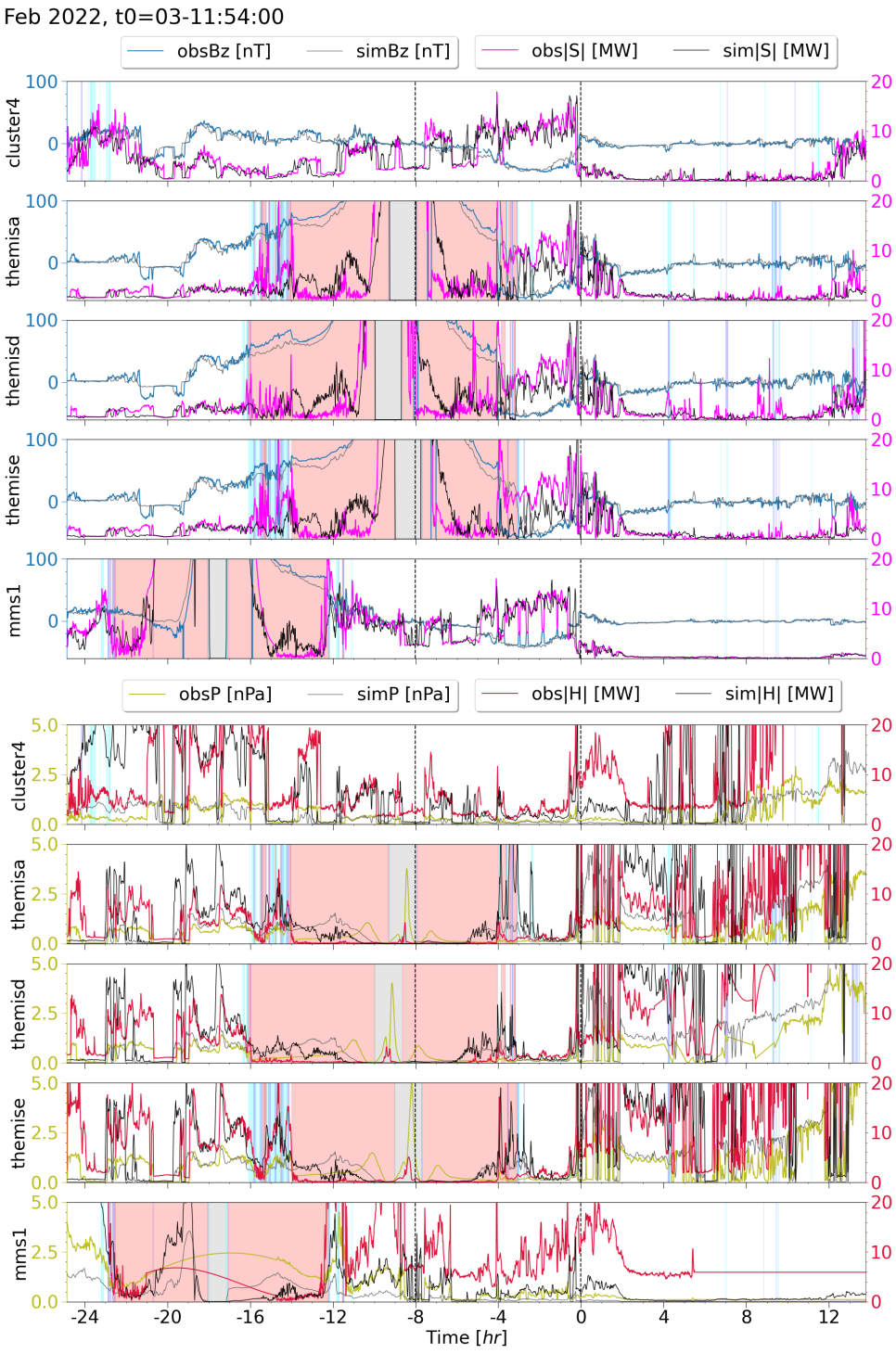

Figure 4.6: Real and virtual satellite traces showing B_z (top 5 panels) and P (bottom 5 panels) on the left axes for model validation. Right axes show derived energy flux values of $|S|$ (top 5 panels) and $|H|$ (bottom 5 panels) to compare the energy transport magnitudes. Shading indicates magnetic topology of the virtual satellite white: open-open, red: closed-closed, blue: open-north open-south. Vertical dashed lines indicate the event main phase.

ing locations and magnitude of energy transport at those crossings. The IMF Bz component is a good proxy for magnetic energy density inside the magnetosphere while the sign change gives a clear indication of magnetopause crossing location on the dayside during southward IMF. For the cluster spacecraft (top panel) there are no magnetic topology changes after the first few hours of the simulation, other than a few sparse points during the recovery phase of the storm as the spacecraft is heading back toward Earth. During the main phase of the storm all four curves Bz, $|S|$, P, and $|H|$ have strong agreement between simulation and observation, which tells us that the simulation was representing the upstream solar wind ahead of the magnetosphere well. This agreement diminishes for the hydrodynamic flux magnitude after the end of main phase with the simulation falling below the observed values.

For the three THEMIS probes there are clear topology changes before the main phase (-16:00 to -13:30) and during the main phase period (-04:00 to -02:30), in each case the magnetopause boundary moves back and forth across the three spacecraft. For the first series of crossings all three virtual craft slightly underpredict the Bz magnitude. For probes A and E that experience more crossings the observed Poynting flux magnitude spikes to much larger values (magenta curves) than the observed counterparts (black curves). At the same time probe D that is a short distance away experiences higher pressures and hydrodynamic flux magnitudes during the same period of time. Later during the main phase all three virtual satellites show an abundance of hydrodynamic flux magnitude and lack of Poynting flux. This mismatch in the type of energy (too much thermal and kinetic, not enough magnetic) at the dayside magnetopause suggests that the simulation is experiencing higher rates of magnetic reconnection than what was observed.

Finally, for the MMS1 spacecraft there are magnetopause crossings early on (-23:00) and later four hours before the main phase begins (-12:00); in each interval the Bz and $|S|$ values match very well. For the second interval near -12:00 as the

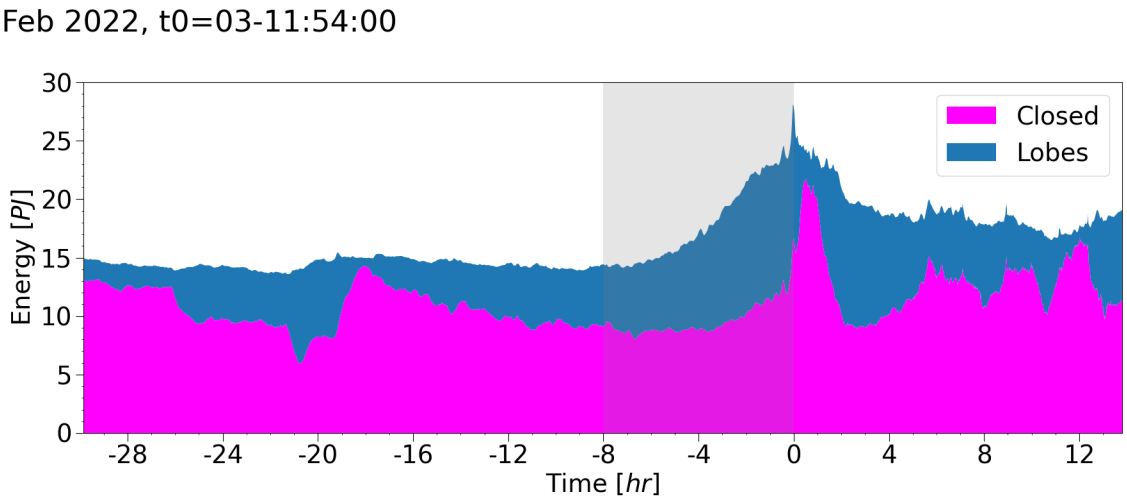

Figure 4.7: Time series of volume integrated energy stacked by region. Shading indicates main phase.

spacecraft exits the magnetosphere there is a significant lack of hydrodynamic energy flux that then persists for the rest of the event. During the main phase the virtual space craft is out of the magnetosphere but there are sudden enhancements in the observed Bz that are not picked up by the virtual spacecraft. These enhancements could be smaller scale transient solar wind features not captured in the solar wind input conditions or magnetosheath effects that the ideal MHD model failed to capture.

4.6 Results

4.6.1 Volume Integrated Energy

Figure 4.7 shows the results of the volume integrated energy within the magnetosphere stacked by the two regions (lobes and closed region), with the main phase highlighted in grey (-08:00 to 00:00) showing an increase in total energy. The shape of the total energy time series for the magnetosphere is very similar to the negative of the simulated SYM-H profile. Chapter VI features more discussion about the connection between magnetosphere energy content and magnetic perturbation.

At several places in the time series there are shifts in the relative contributions

of the two regions with a smaller change in the total energy. This effect indicates an internal reconfiguration of energy between closed field and open field regions. In order to understand this reconfiguration we look at energy flux at the interfaces.

4.6.2 External Surface Integrated Energy Flux

In order to contextualize the integrated energy flux through the magnetopause surface let's look at a back of the envelope calculation of what the input energy flux would be of an unblocked solar wind passing through the projected area of the magnetopause. For this example we consider main phase like conditions similar to 04:00 of this event: $B = 16\,[nT]$, $u = -525\,[km/s]$, $n = 2.5\,[\#/cc]$, $P_{th} = 6.5 \times 10^{-3}\,[nPa]$, and an effectively circular projected area with radius $R = 18\,[R_E]$. These conditions would yield hydrodynamic and magnetic pressures of $1.16\,[nPa]$ and $0.2037\,[nPa]$. Converting from pressure units to energy density per R_E^3 this yields $P_{hydro} = 0.3\,[TJ/R_E^3]$, $P_{mag} = 0.0527\,[TJ/R_E^3]$. Taking these energy densities combined with the projected area ($18R_E^2\pi\,[R_E^2]$) and a solar wind velocity of $0.0824\,[R_E/s]$ we can obtain the unblocked solar wind hydrodynamic, Poynting, and total integrated energy fluxes.

$$\int dA \cdot H_{solarwind} = 0.3\left[TJ/R_E^3\right] * 18^2\pi\left[R_E^2\right] * 0.0824\,[R_E/s] = \boxed{25\,[TW]} \quad (4.2)$$

$$\int dA \cdot S_{solarwind} = 0.0527\left[TJ/R_E^3\right] * 18^2\pi\left[R_E^2\right] * 0.0824\,[R_E/s] = \boxed{4.4\,[TW]} \quad (4.3)$$

From this example calculation it is clear that most of the unblocked solar wind energy would be in the form of hydrodynamic flux with a total power of near $30\,[TW]$.

With this value in mind we see that indeed the magnetosphere does block much of the solar wind incoming energy, figure 4.8 shows the integrated energy flux values for all the external interfaces of the simulated magnetosphere. The extreme energy flux values occur for all three energy types at the end of main phase with total energy

injection being over 12 $[TW]$, still only a fraction of a nominal unblocked solar wind input.

Looking at the first panel of figure 4.8 the closed region-sheath interface (5) is dominating the integrated hydrodynamic energy flux for most of the event, especially during main phase. This is a similar result to the energy flux integrated over the dayside sector of the magnetopause found in chapter III, but now the division is not a fixed $X = 0$ plane, but the magnetic topology of closed-closed. As the main phase comes to an end we see closed region-sheath interface (5) become balanced by injection contributions (negative values) from the closed region - inner boundary interface (7). This interface represents hydrodynamic energy flux outflow from the inner boundary out into the magnetosphere. Around the end of main phase (00:00) there is also a sharp injection of hydrodynamic flux through the lobe-sheath interface (1), which otherwise remains small.

Moving to the second panel looking at integrated Poynting flux, the lobe-sheath interface (1) experiences magnetic energy injection in the same way the closed-sheath interface (5) experiences hydrodynamic energy escape, while the inner boundary interfaces (3,7) develop an interesting flux pattern. Shortly into the main phase (-06:30) there becomes a pair of nearly balanced contributions in the form of energy injection (negative) from the lobes-inner boundary interface (3) and energy escape (positive) from the closed region - inner boundary interface (7). Interestingly late into the main phase (-02:00 to 00:00) the closed region - inner boundary interface (7) experiences simultaneous hydrodynamic energy injection and Poynting flux escape. The combined effect of this simultaneous transport is shown in the third panel with integrated total energy flux; the closed region - inner boundary (7) surface has total energy flux escape until the end of main phase when the integrated value decreases and eventually changes sign.

Both for the lobe - sheath interface (1) and the closed region - inner boundary

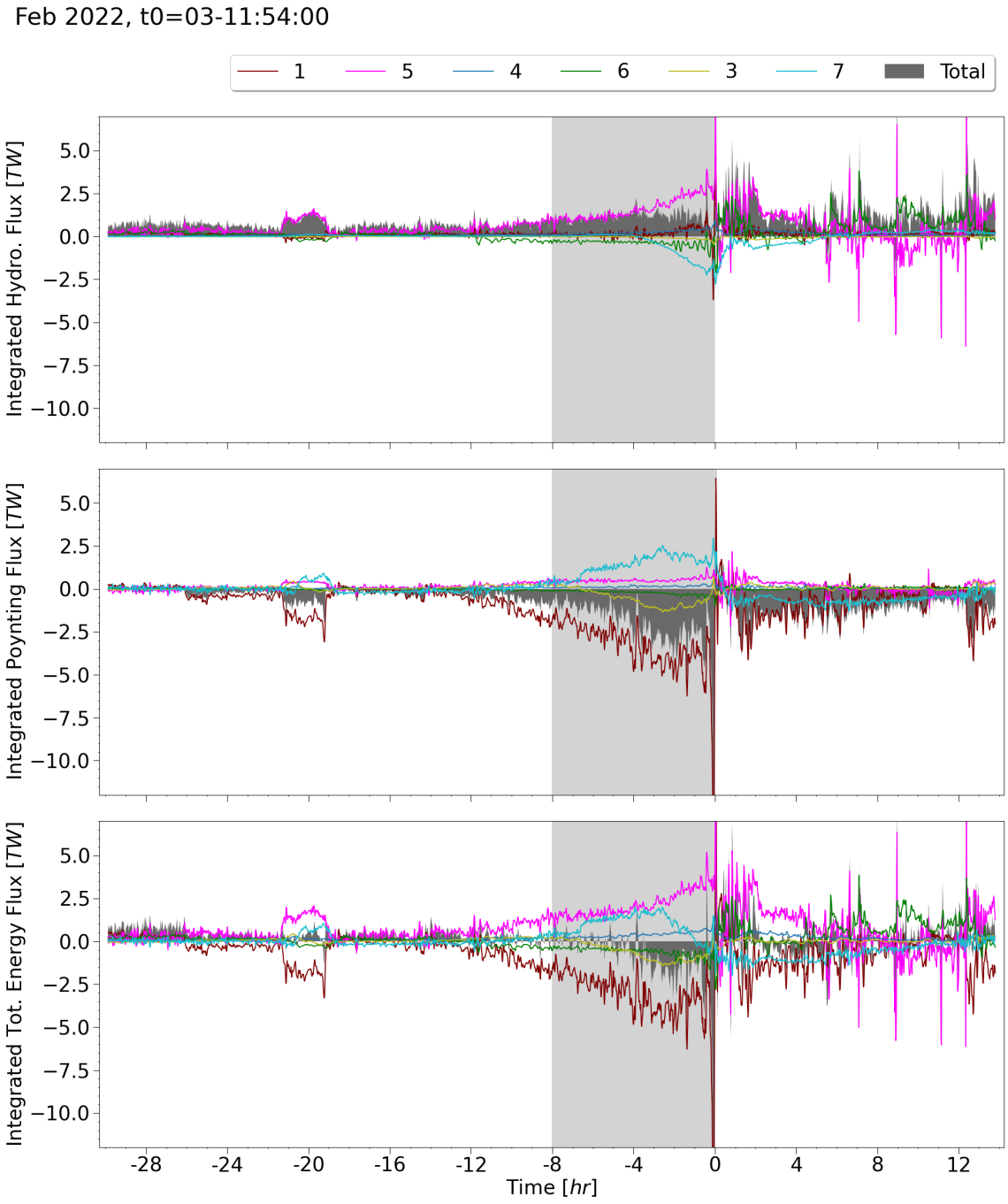

Figure 4.8: Time series of surface integrated energy flux for the interfaces in 4.2. 1: lobe-sheath, 3: lobe-inner boundary, 4: lobe-tail cutoff, 5: closed-sheath, 6: closed-tail cutoff, 7: closed-inner boundary. Top panel shows integrated hydrodynamic flux, middle panel Poynting flux, and bottom panel total energy flux.

surface (7) there are periods in which one type of integrated energy flux (hydrodynamic or Poynting) is injecting while the other is escaping; this can be explained by looking at the energy transport equation. In the ideal MHD limit the hydrodynamic flux is always in the direction of the plasma bulk flow $\left(\frac{1}{2}\rho u^2 + \frac{\gamma}{\gamma-1}P_{th}\right)\mathbf{u}$, while the Poynting flux has a contribution in the direction of the plasma bulk flow as well as a contribution opposite the magnetic field direction $\left(\frac{B^2}{\mu_0}\right)\mathbf{u} - \left(\frac{\mathbf{B}\cdot\mathbf{u}}{\mu_0}\right)\mathbf{B}$. This second term in the ideal MHD Poynting flux vector allows for the two types of energy flux to take opposite sign, especially when the magnetic field is normal to the interface surface. This is precisely the situation for both the lobe-sheath interface (1) where $\mathbf{B}$ points out toward the sheath and the closed region - inner boundary interface (7) $\mathbf{B}$ points mostly with the interface normal in the northern hemisphere and the opposite direction in the southern.

Consider a small amount of radial outflow from the inner boundary into the magnetosphere. From the hydrodynamic perspective this is energy flux injection into the system. In the northern hemisphere $\mathbf{B}\cdot\mathbf{u}$ is negative and $\mathbf{B}$ points into the $-\mathbf{r}$ direction yielding $-(-Bu)-\hat{\mathbf{r}}$ or energy in the $-\hat{\mathbf{r}}$ direction. This direction is considered energy escape for the magnetosphere and opposite the hydrodynamic flux direction. In the southern hemisphere the same condition appears, where now $\mathbf{B}\cdot\mathbf{u}$ is positive and $\mathbf{B}$ has a component in the $+\hat{\mathbf{r}}$ direction, so $-(+Bu)+\hat{\mathbf{r}}$ is again in the $-\hat{\mathbf{r}}$ direction, opposite the hydrodynamic flux.

4.6.3 Internal Surface Integrated Energy Flux

Next we look at the internal interfaces in the magnetosphere along the interfaces that divide up the magnetosphere volume; the dayside mapped closed region - lobes interface (2a) represents the cusp while the nightside mapped closed region - lobes interface (2b) represents the plasma sheet boundary layer in the tail. Figure 4.9 shows the three types of integrated energy flux for each interface and the fourth panel shows

the integrated energy flux for the intersection of the closed region volume with the X=0 plane.

The first panel reveals very little integrated hydrodynamic energy flux through either interface with a clear bias to the cusp interface (2a) at almost all times; the reverse is true for both the direction and magnitude of the integrated Poynting flux results (second panel). With large magnitudes of integrated Poynting flux through both interfaces and directions that balance, magnetic energy moves from the closed region to the lobes through the cusp (+ values for 2a) and from the lobes to the closed region going into the tail (- values for 2b).

Even before the main phase begins there is an increase in the integrated Poynting flux values and an imbalance in favor of the tail transport, and the magnitudes also begin to decrease approaching the end of the main phase. This pattern seems to indicate a sensitivity of the internal energy flux to the negative IMF B_z component that also changes in this way.

The internal transport within the closed region shown in the bottom panel indicates a symmetric transport with dawn and dusk contributions moving from the nightside to dayside throughout the main phase. In this case both integrated hydrodynamic flux and Poynting flux have the same sign, with slightly higher Poynting flux values, which makes sense given the high magnetic field strengths near the inner edge of the closed region volume. The internal transport through the closed region supports both the external and internal interface results, in which energy must get to the dayside closed region to escape to the sheath (+ values interface 5) and move back to the lobes (+ values interface 2a). The sunward direction of this internal energy flux also matches the ideal equatorial ion plasma convection shown in figure 1.6.

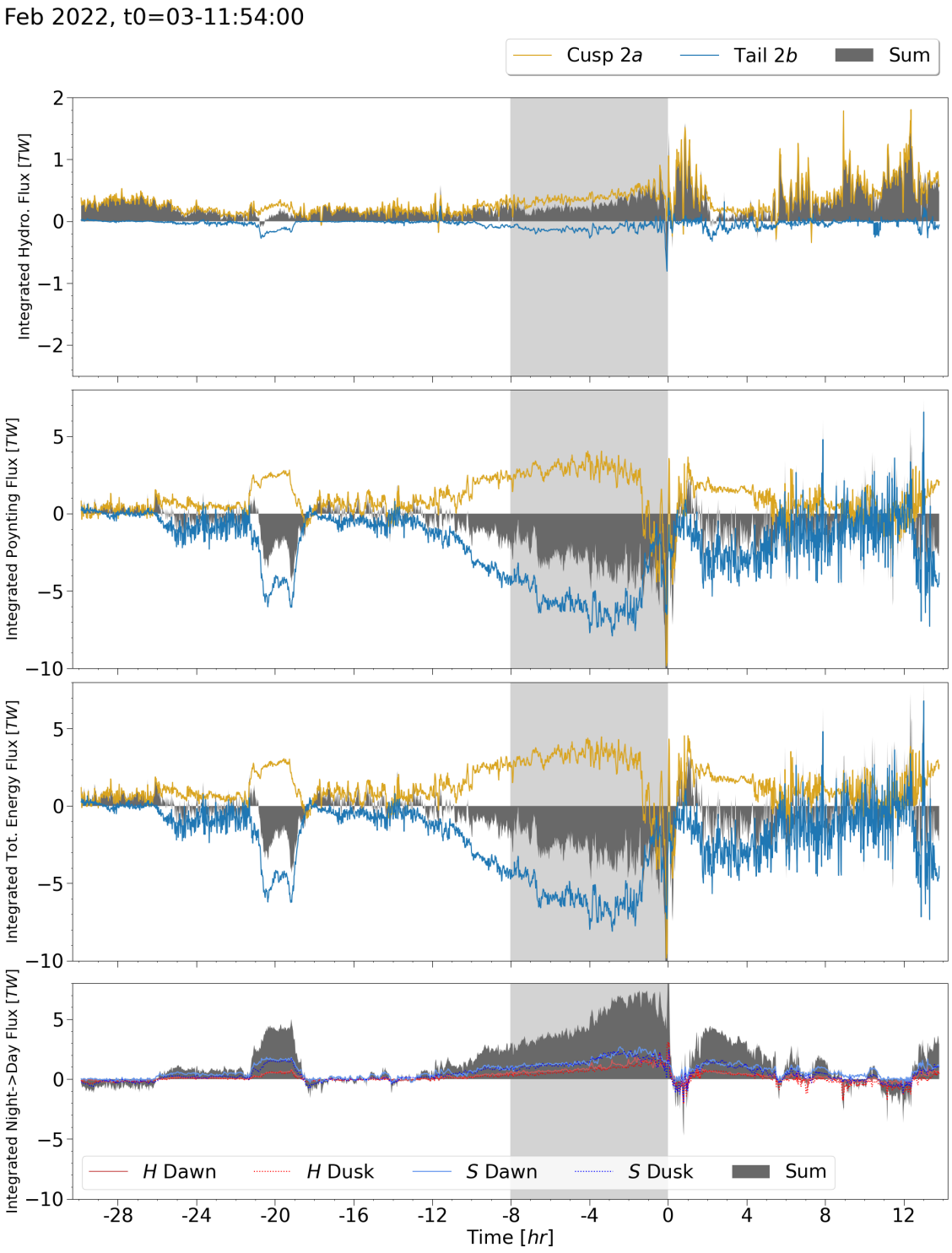

Figure 4.9: Time series of surface integrated energy flux for the interfaces labeled in figure 4.2. 2a: daymapped lobe-closed (cusp), 2b: nightmapped lobe-closed (tail). Top panel shows integrated hydrodynamic flux, middle panel Poynting flux, and third panel total energy flux. Bottom panel shows integrated Poynting and hydrodynamic flux across the $X = 0$ plane intersection with the closed region volume, split by dawn $(-Y)$ and dusk $(+Y)$ sectors.

Table 4.1: Time integrals over the storm main phase of the hydrodynamic energy flux, Poynting flux, and total energy flux.

	Energy $[PJ]$	$\int Hdt$	$\int Sdt$	$\int Kdt$
1	Lobes→Sheath	+4.67	–97.28	–92.61
2a	Closed→Lobes (day)	+11.20	+58.82	+70.01
2b	Closed→Lobes (night)	–3.45	–153.12	–156.56
3	Lobes→Inner	–1.72	–15.34	–17.06
4	Lobes→TailCut	+7.01	+3.94	+10.96
5	Closed→Sheath	+46.62	+14.57	+61.19
6	Closed→TailCut	–10.57	–6.21	–16.79
7	Closed→Inner	–12.69	+40.48	+27.80

4.6.4 Main Phase Time-Integrated Energy Transport

In order to compare the amount of energy transported through the various interfaces we integrate the already spatially integrated surface flux values now in time for the main phase interval (-08:00 to 00:00) for each energy type shown in table 4.1. Considering the nominal unshielded solar wind total energy flux value from earlier of $30\,[TW]$ the time integrated energy injected from the solar wind for this interval of time would amount to $864\,[PJ]$. Clearly much of this solar wind energy is indeed being blocked, as the maximum injected energy to the simulated magnetosphere comes through the lobes sheath interface (1) with only $93\,[PJ]$.

Using the tabulated values we can clearly see the recirculation effect of the cusp and tail internal interfaces (2a and 2b). From the lobes perspective it received $93\,[PJ]$ of energy from outside but was able to give $156\,[PJ]$ of energy to the closed region through the 2b interface. This is only possible when considering it received another $70\,[PJ]$ of energy that almost balances the deficit ($163\,[PJ]$). In other words the internal cusp and tail interfaces (2a and 2b) recirculated large amounts of magnetic energy throughout this main phase.

4.6.5 Four Field Junctions and Magnetic Topology

In order to explore the magnetic reconnection that leads to magnetic topology change in the magnetosphere, we employ the four field junction technique developed by *Laitinen et al.*(*Laitinen et al.*, 2007) that finds locations in the MHD simulation domain where the four types of magnetic topology are adjacent (open-open, closed-closed, open-north, closed-south).

The topology variable is a discrete state variable that contains one unique value for each type of topology, in order to capture the four field junctions this topology variable is vectorized into four variables each containing either 1 or 0 for each possible topology. Then a linear interpolation is done that smooths the discrete data at the point located positions yielding cell centered values that can range between 0 and 1 for each cell. Note that the cells in this cell-centered location are not the simulation finite volume cells, but the dual grid cells used in the output of the data only. These cell-centered results from the interpolation are then linearly interpolated a second time back to the point location, thus spreading the discrete values to neighborhoods of points that surround them. Each point that contains a value of > 0.1 for all four of the twice interpolated vectorized topology variables is counted as a four field junction neighborhood. This approach is easily implemented entirely in post processing on the dual grid using any 3D analysis software and makes an efficient way to quickly visualize the four field junction patterns without any modification to the simulation setup.

Figure 4.10 shows snapshots of the magnetopause from two viewing angles during the interval just after the main phase for 30 minutes in 10 minute increments; revealing the dynamic change in the magnetic topology that occurs. The contour on the magnetopause surface is the magnetic topology with white representing closed, orange open-north, and red open-south. From the two perspectives you can see the northern and southern cusp as the dividing line between the closed and open topologies.

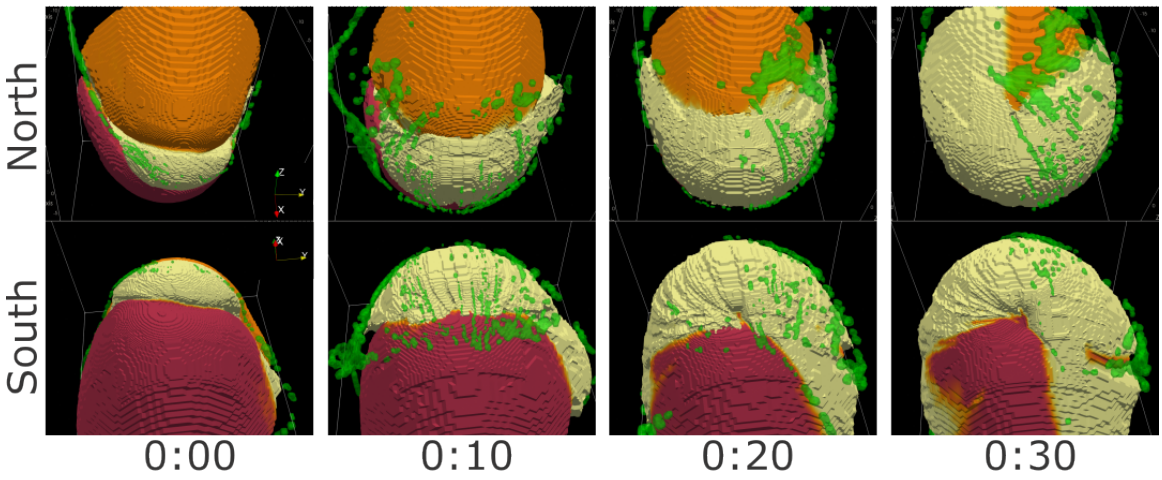

Figure 4.10: Snapshots of the magnetopause surface from two camera angles (top looking down from above, bottom looking up from below) just after the main phase end spaced 10 minutes apart. Contour shows magnetic topology (yellow- closed, orange- open north, maroon- open south) and green isosurfaces shown four field junction neighborhoods where all four magnetic topologies are adjacent.

The four field junction neighborhoods are shown in green isosurface, at 00:00 there is a single clean separator line revealed by the four field junctions going across the closed region. Just 10 minutes later there are many vertically oriented separator lines that are rapidly advecting away from where they initially form; as time progresses both the open-north and open-south topology begin to convert to closed topology as reconnection occurs in both north and south lobes simultaneously.

I encourage you to check out the video of this process (found in the supplementary info of the published paper), which better captures the explosive nature of this topology change process.

4.6.6 Interpretation

From these results we see two clear energy pathways emerge. The first is the external pathway in which magnetic energy is injected from the sheath into the magnetosphere through the lobes (interface 1), and balanced by hydrodynamic energy escape through the closed region (interface 5). This is exactly in line with results

obtained in the previous study from chapter III, but now rather than looking at fixed spatial distributions of energy flux on the magnetopause surface we split the surface according to the magnetic topology. With this split it is more clear that the closed topology is indeed where hydrodynamic energy flux is escaping.

The second pathway is an internal recirculation of magnetic energy from the closed region through the cusp (2a) back to the lobes and down again to the closed region through the internal tail interface (2b). This recirculation explains how the lobes are able to contain such large quantities of energy at any moment in time without the magnetic topology that enforces a magnetic bottle to trap plasma. In the volume integrated results from figure 4.7 the shift in the contribution between lobes and closed region (00:00 to 02:00) corresponds exactly with the decay and reversal of the internal energy pathway (2a and 2b integrated fluxes).

The two energy pathways are summarized in figure 4.11.

Zooming into the time just after the end of the storm main phase (00:00) we can put several results together to gain a better understanding. First the volume energy results reveal simultaneously a sharp increase in total energy and a transfer from energy in the lobes to the closed region. As mentioned, at the same time there is a reversal in the internal energy circulation with Poynting flux reversing direction moving from the lobes to the closed region through the cusp (- flux in 2a). In the external results we see a sharp injection of hydrodynamic flux through the lobes (- flux in 1), and in the four field junction results we see the topology change from open to closed in each lobe. All of this together tells us that simultaneous lobe reconnection reverses the flux transport at the cusp and brings net energy into the system while evacuating the lobes.

During this brief interval the total energy in the lobes falls from around $20\,[PJ]$ to less tha $5\,[PJ]$ in under 60 minutes (00:00 to 01:00), and recovers just as quickly (01:30 to 02:30). The total energy peaks at the start of this process gaining about

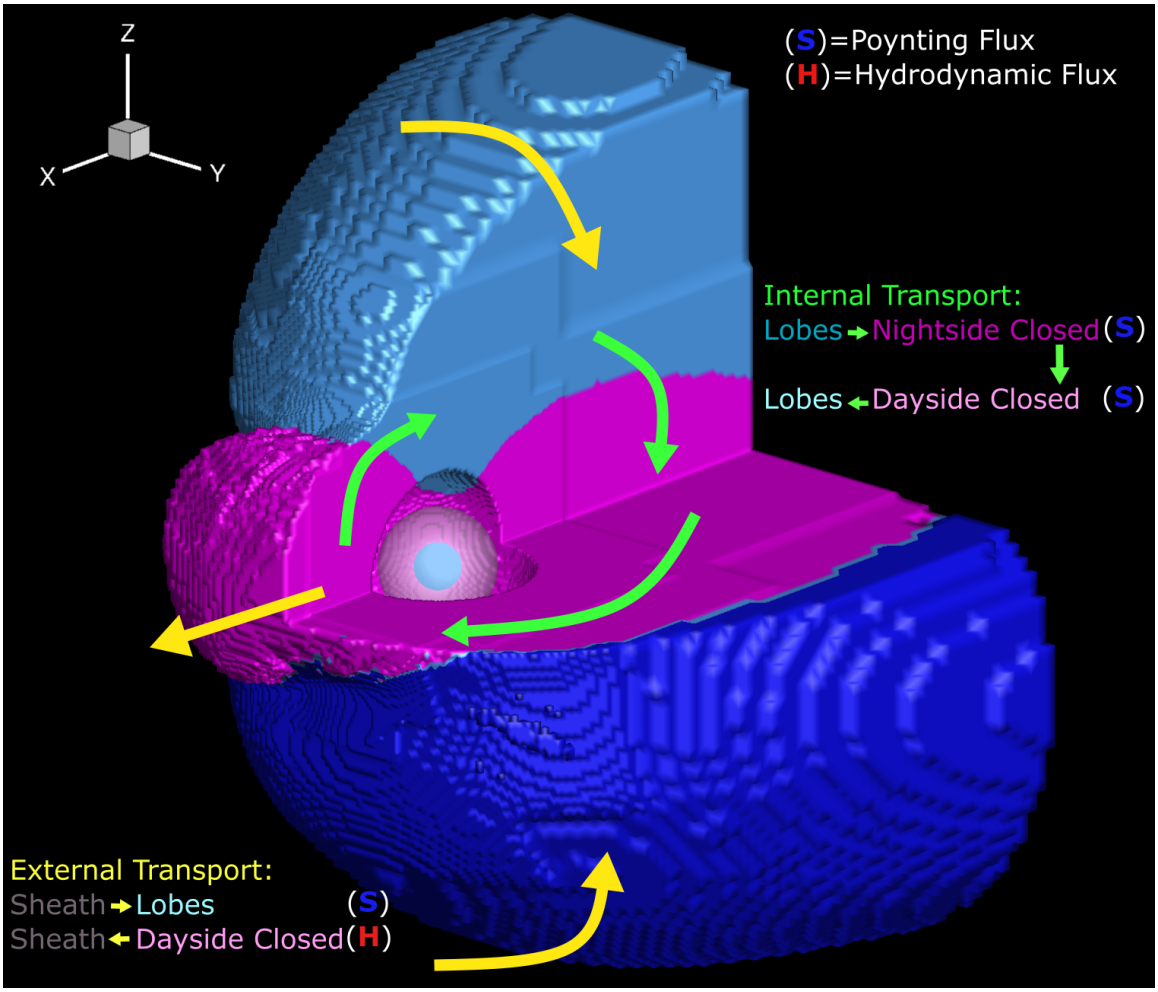

Figure 4.11: Summary of external (yellow arrows) and internal (green arrows) energy transport throughout the magnetosphere. The type of energy primarily transported is labeled next to each flux text description.

$+3\,[PJ]$ corresponding with a drop in the simulated SYM-H of about $15\,[nT]$. This SYM-H drop is not observed and in fact responds to the dynamic pressure pulse instead, experiencing a positive rise in magnetic perturbation.

Unfortunately the spacecraft that have data available were not well positioned during this short interval at the end of main phase, but based on comparisons made at other interface crossings throughout the event it appears as though the simulation overpredicts the amount of magnetic reconnection that occurs. This effect is common for ideal MHD simulations, in which reconnection physics is not controlled explicitly but rather by proxy via the grid resolution and choice of flux limiter, that controls the amount of numerical diffusion within each cell. This over abundance of reconnection could be why there was not an influx of energy and resulting drop in the observed SYM-H at 00:00.

Looking closer at the connection between the solar wind driving and the integrated energy fluxes it is clear that the IMF impacts both the external and internal energy transport. For the external transport the net injection of energy corresponds very well with the main phase window that also starts and stops with changes in the IMF clock angle (B_z and B_y components). In contrast the internal energy flux seems to get an early start and decay with respect to the main phase window that corresponds more closely with the IMF B_z component alone.

4.7 Discussion

In this study another real event was simulated and the energy analysis was expanded from the magnetopause surface to the whole magnetosphere. By dissecting the magnetosphere the Dungey cycle-like energy transport was revealed in and quantified.

For the energy external pathway reconnection on the dayside causes simultaneous hydrodynamic energy flux escape from the closed region into the sheath (5) and

Poynting flux injection through the lobes (1) as newly opened flux is whisked downstream and adds to the total volume of the lobes. This difference is maintained by the internal transport of energy from the nightside closed region to the dayside across both the dawn and dusk portions of the X=0 plane.

This dayside reconnection and sunward motion of energy also necessitates energy exchange between the lobes and closed region. In the tail the magnetic energy injection from the sheath (1) moves directly down into the closed region (2b), but the tabulated transport values make it clear that in addition to the external energy passed there is also recirculated energy passed through the dayside closed region to the lobes (2a) that combines with the external injection (1+2a=2b).

As the IMF turns northward for this event, the simulated magnetosphere undergoes simultaneous lobe reconnection that moves the reconnection location to higher latitude relative to the cusp and reverses the energy flux between the lobes and closed region at the cusp (2a) while temporarily bringing in net energy. This reversal is consistent with the 2D reversal of plasma flow shown in 4.1. This cusp energy flux reversal breaks the internal circulation loop and quickly drains the lobes pouring most of its energy back to the closed field.

There are many new simulation outputs demonstrated with these results that can help us better understand the solar wind magnetosphere coupling process, and the comparison with observations for this event exemplify why getting reconnection physics correct in the simulation is so important. In the next study we will explore ideal cases to better probe the connection between the solar wind conditions, the internal state of the magnetosphere, and the amount of energy transported at these various magnetospheric interfaces.

CHAPTER V

Parameters of the Solar Wind: Curse of the Energy Coupling Function

5.1 Introduction

In this chapter we return from real storm conditions to idealized solar wind inputs in order to study the relationship between the external and internal energy transport pathways identified in chapter IV with basic input solar wind properties and the state of the magnetosphere.

The linkage between the solar wind and energy transport was identified immediately, but the first model that quantified the process was not developed until 1978 with the ϵ parameter (*Perreault and Akasofu*, 1978). The purpose of a coupling function model is to express the amount of energy (sometimes magnetic flux) that enters into the magnetosphere as a function of the solar wind conditions. The ϵ (5.1) parameter was based on a geometric argument in which magnetic reconnection would open the magnetosphere according to some length l_0 modified by the IMF clock angle θ' and the solar wind passing across this length would be proportional to the energy that enters the magnetosphere.

$$\epsilon(t) = \frac{|E(t)||B(t)|}{4\pi}\left(l_0 \sin^2\frac{\theta'(t)}{2}\right)^2 = 10^7 v B^2 \sin^4(\theta/2) \tag{5.1}$$

Name	Functional Form	Reference
B_z	B_z	(*Dungey*, 1961)
Velocity	v	(*Crooker et al.*, 1977)
Density	n	
p	$nv^2/2$	(*S. Chapman et al.*, 1930)
B_s	$B_z(B_z < 0); 0(B_z > 0)$	
Half-wave rect.	vB_s	(*Burton et al.*, 1975)
ϵ	$vB^2 sin^4(\theta_c/2)$	(*Perreault and Akasofu*, 1978)
ϵ_2	$vB_T^2 sin^4(\theta_c/2)$	Variant on ϵ
ϵ_3	$vBsin^4(\theta_c/2)$	Variant on ϵ
S.W. E-field	vB_T	
E_{KL}	$vB_T sin^2(\theta_c/2)$	(*Kan and Lee*, 1979)
$E_{KL}^{1/2}$	$\left[vB_T sin^2(\theta_c/2)\right]^{1/2}$	Kan-Lee Variant
E_{KLV}	$v^{4/3}B_T sin^2(\theta_c/2)p^{1/6}$	(*Vasyliunas et al.*, 1982)
E_{WAV}	$vB_T sin^4(\theta_c/2)$	(*Wygant et al.*, 1983)
E_{WAV2}	$\left[vB_T sin^4(\theta_c/2)\right]^2$	Variant on EWAV
$E_{WAV}^{1/2}$	$\left[vB_T sin^4(\theta_c/2)\right]^{1/2}$	Variant on EWAV
E_{WV}	$v^{4/3}B_T sin^4(\theta_c/2)p^{1/6}$	(*Vasyliunas et al.*, 1982)
E_{SR}	$vB_T sin^4(\theta_c/2)p^{1/2}$	(*Scurry and Russell*, 1991)
E_{TL}	$n^{1/2}v^2 B_T sin^6(\theta_c/2)$	(*Temerin and Li*, 2006)
$d\Phi_{MP}/dt$	$v^{4/3}B_T^{2/3} sin^{8/3}(\theta_c/2)$	(*Newell et al.*, 2007)
E_{in}	$n_{\rm sw}^{0.24}V_{\rm sw}^{1.47}B_T^{0.86}\left[\sin^{2.7}(\theta_c/2) + 0.25\right]$	(*Wang et al.*, 2014)
P_{storm}	$\frac{B_T^2 V_x}{\mu_0} M_A \sin^4(\theta/2) \frac{135 \pm 9}{5\times 10^{22}\lvert B_z\rvert^3 + 1} R_E^2$	(*Tenfjord and Østgaard*, 2013)

Table 5.1: Table adapted from *Newell et al.* (2007), several functional forms for solar wind magnetosphere coupling.

Several other coupling functions have been proposed with at variety of functional forms; table 5.1 reproduced from *Newell et al.* (2007) lists many of them with the associated references.

Several of the coupling functions listed follow from the more general functional form outlined in *Vasyliunas et al.* (1982) that used a dimensional argument to define the possible combinations of solar wind variables that would yield units of power. This general functional form was even used with MHD results to fit to energy injection through the magnetopause (*Wang et al.*, 2014). The magnetopause was identified in that work using an adapted version of the flow-field traced method described by *Palmroth et al.* (*Palmroth et al.*, 2003). Chapter II describes the key differences between the magnetopause used in this work and the flow-field traced methods.

	$n\,[\#/cc]$	$u_x\,[km/s]$	$T\,[K]$
LOW n LOW u	5	-400	300000
HIGH n HIGH u	20	-800	300000
LOW n HIGH u	5	-400	300000
HIGH n LOW u	20	-400	300000

Table 5.2: Test matrix conditions for solar wind plasma parameters.

One challenge to using simulation results to compare with these coupling functions is that the magnetosphere is never actually a steady system. Because Earth's dipole axis is offset from the planets axis of rotation, the effective angle between the solar wind and the dipole field experiences daily variation even if the solar wind inputs are steady. Furthermore, ultra low frequency (ULF) fluctuations on the order of minutes to hours can exist in the magnetosphere, which lead to oscillations in the system state.

Putting aside the fundamental unsteady properties of the magnetosphere, the energy coupling process itself causes the magnetosphere energy state to change, which in turn changes the volume and geometry of the system, leading to internally initiated dynamics. This can be clearly seen in the integrated magnetosphere volume results shown in chapter III figure 3.10 when under steady solar wind conditions the magnetosphere volume experiences large oscillations over several hours.

5.2 Methodology

To determine the effect of the input solar wind properties on energy transport we construct a test matrix with $4 \times 24 = 96$ conditions, where each of the 3 sets of 24 test points only varies the IMF conditions of the solar wind. The IMF conditions for the 24 test points along with the preconditioning conditions are shown in the first panel figure 5.1. For the other solar wind properties that were held steady, the conditions are listed in table 5.2.

This test matrix is constrained in several important ways. First the IMF B_x

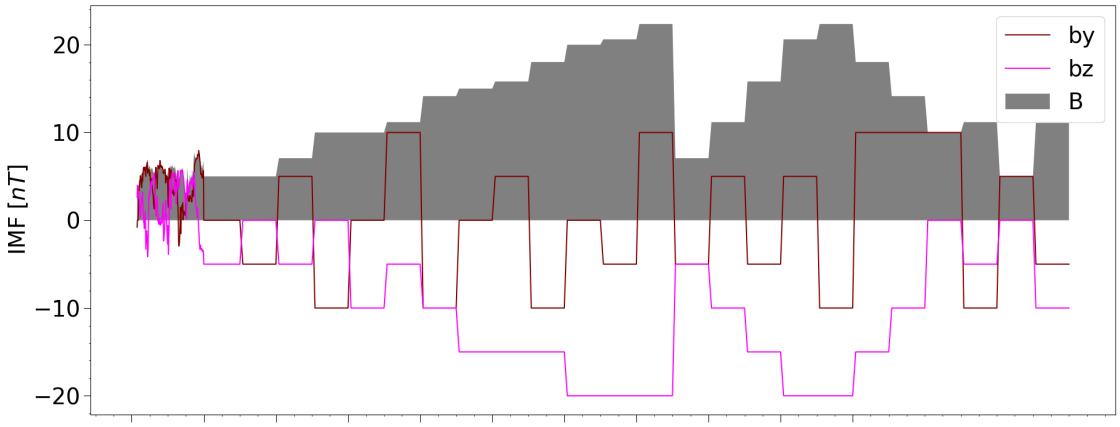

Figure 5.1: IMF conditions for each matrix pass of 24 conditions. All runs are preconditioned with the same preconditioning conditions (3 hours of solar wind taken from real event in May of 2019).

component is set to 0 because it is often omitted from the coupling functions that will be used for comparison. Second, the IMF B_z component is always ≤ 0 to constrain our analysis to only typical storm main phase like conditions. Thirdly, the conditions are held steady in two hour increments but the system is not reset after each two hour period. This allows for any transition effects to pass through the system, while also fostering a larger range of total energy content in the magnetosphere. Finally, only the IMF conditions are changed in one pass to minimize the dynamic pressure pulses that may cause magnetopause compression and oscillations.

Table 5.3 lists the ranges of derived parameters and magnetospheric energy levels observed from this test matrix. The goal is to provide large coverage of the potential storm-like solar wind conditions that could be experienced during a main phase.

The energy analysis is performed in the same was as chapter IV section 3.2, and each test point is isolated. Then two different comparison techniques are employed. The first simply takes the mean of the values over the second hour of each interval. This should avoid condition transition effects while providing a large enough sample to characterize average behavior. Second the same approach is taken, but with the median instead of the mean. This reduces the influence of any outliers in the hour

Parameter	Range (min, max)
$P_{dyn}\,[nPa]$	(1.33, 21.41)
β	(0.05, 6.83)
β^*	(3.42, 1080)
M_A	(1.83, 32.8)
$B_T\,[nT]$	(1.50, 22.4)
$E_{in}\,[TW]$	(0.19, 24.5)
$P_{storm}\,[TW]$	(-19.1, 0)
$R_{0,Shue98}\,[R_e]$	(5.63, 10.90)
Integrated $U\,[PJ]$	(7.41, 31.0)

Table 5.3: Ranges of derived solar wind parameters and integrated magnetosphere energy U.

long interval results.

5.3 Preliminary Results

The results for this work are still being processed, but the preliminary outputs are promising. Figure 5.2 shows the time series of the integrated magnetosphere energy density U for each case. The steady intervals are indicated by the vertical dashed lines. Clearly there are many internal magnetosphere dynamics at play, as was expected, as evident by the high variability in the magnetosphere energy. The high density, high velocity case has the most energy across the intervals and also experiences the most dramatic changes in energy.

Because the energy content changes rapidly within a single interval, it necessarily means that the energy flux terms do as well. To work around this, these preliminary results have been averaged over the second hour of each interval.

Figures 5.3 and 5.4 compare the total energy flux into the magnetosphere (sum of external magnetopause and inner boundary fluxes) to two separate coupling functions for energy input.

The first comparison is with the P_{storm} parameter from *Tenfjord and Østgaard* (2013), which uses observational data to identify the parameters in the scaling ar-

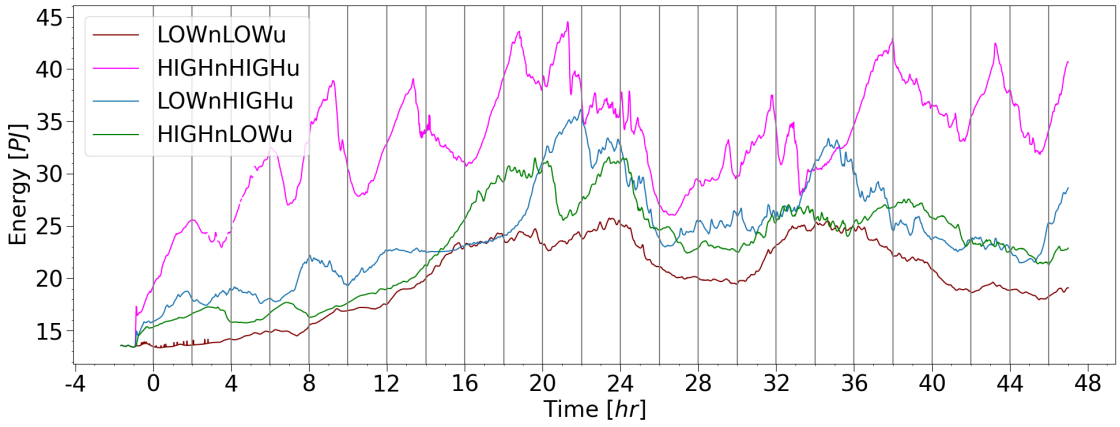

Figure 5.2: Time series of integrated magnetosphere energy density U for each matrix case. Steady solar wind conditions are maintained between vertical dashed lines.

gument coupling functional form. The dashed 1-1 line reveals several data points at low coupling values that have the higher energy transport, and the reversed for higher coupling values. There are also values for the averaged net energy flux when the magnetosphere energy is decreasing, and the P_{storm} function cannot be negative.

comparison with two energy input coupling functions that each use the Vasyliunas formation (*Vasyliunas et al.*, 1982), one with data and the other with and MHD model using different methods

Next is the comparison with the E_{in} coupling function (*Wang et al.*, 2014), the results of this comparison appear much more linear albeit with a different slope. Across the range of coupling values the averaged integrated total energy flux had lower values. Similar to the P_{storm} comparisons when the averaged values show net energy decrease in the magnetosphere there is a large departure from the coupling function value.

From the results shown in chapter IV we saw how the change and reversal of internal energy flux at the closed region-lobe interface on the dayside cusp can signify a major reconfiguration in the energy content in the magnetosphere. In order to see what solar wind conditions might lead to differences in this internal energy pathway we

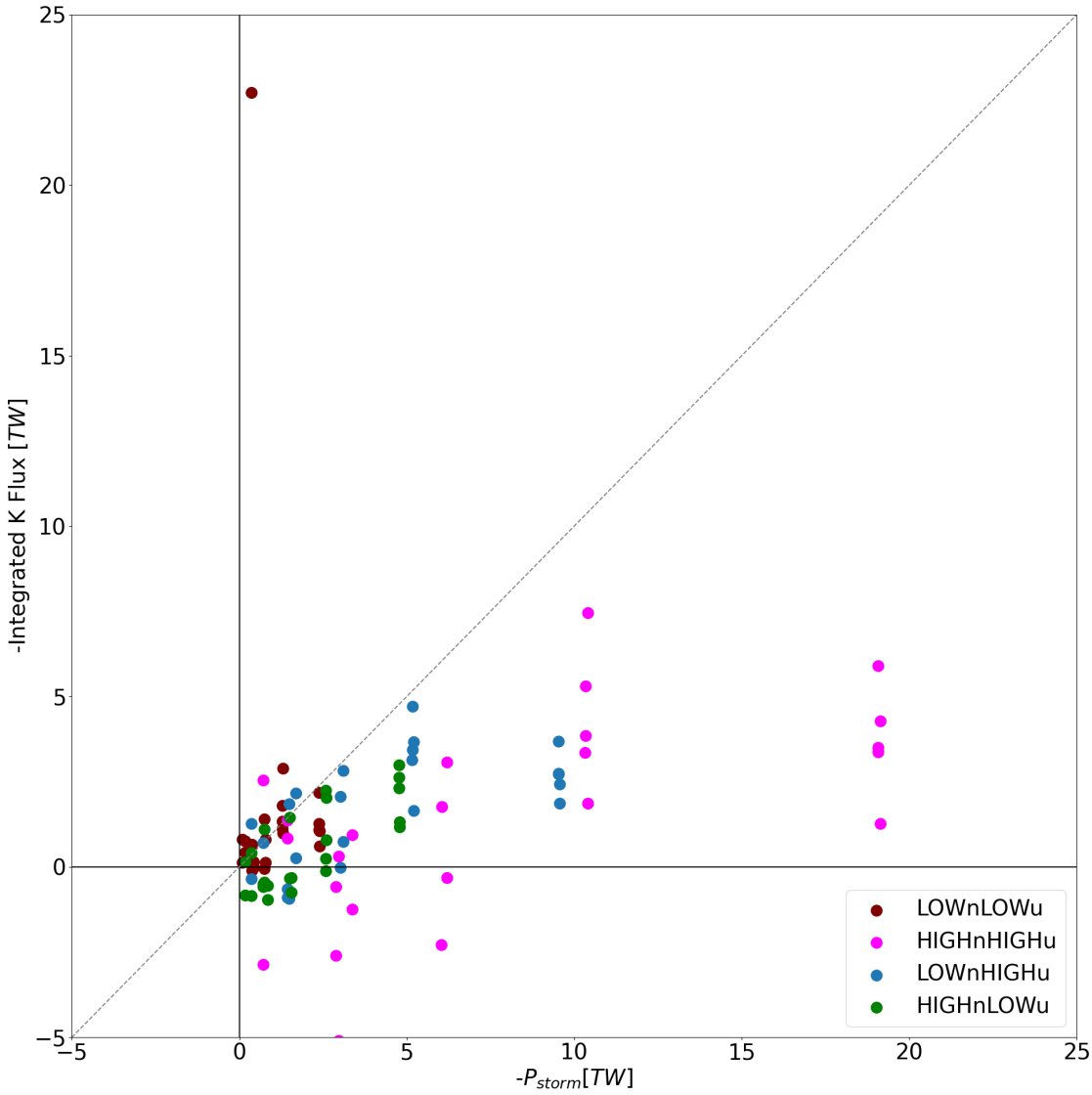

Figure 5.3: Comparison of P_{storm} from *Tenfjord and Østgaard* (2013) and integrated total energy flux K from external and internal boundaries. Dashed line indicates exact correlation.

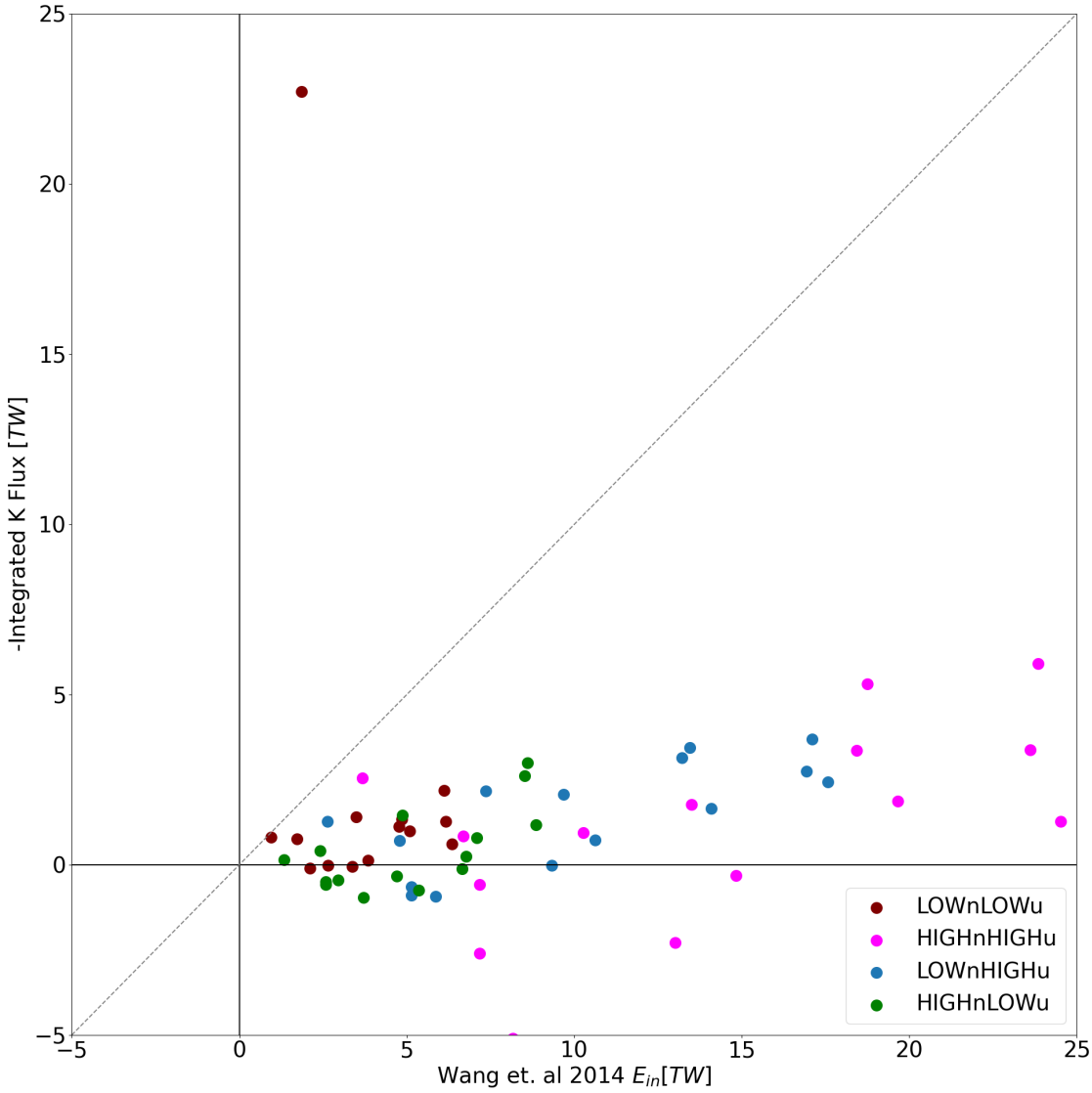

Figure 5.4: Comparison of E_{in} from *Wang et al.* (2014) and integrated total energy flux K from external and internal boundaries. Dashed line indicates exact correlation.

plot the averaged quantities of the integrated energy density U against the integrated energy flux across the internal cusp interface (K_{2a}).

The results shown in 5.5 show large variability in the potential averaged cusp values with increasing energy content. When the integrated flux is positive, this is consistent with the storm event findings. When the energy recirculating is present and energy is passed from the closed region to the lobes, the lobes increase in energy. With more total energy in the system it is expected that some of that energy will reside in the lobes and therefore the internal energy flux will also be increased.

Interestingly, we see that the lower averaged integrated cusp flux values and the cases that have reversed transport occur at both high energy (x axis), high dynamic pressure (X and triangle cases with high velocity), and increased IMF B magnitude (color bar).

Moving to investigate the inner boundary flux, another comparison is made between the magnetosphere energy and the inner boundary lobe flux (K_3) in 5.6. From these results there appears to be a strong bimodal patter. With increasing energy there is both increasing positive and negative averaged integrated inner boundary lobe flux values. When there is more energy in the magnetosphere, the inner boundary lobe flux is enhanced in whichever direction the flux is pointing.

The same comparison is then made with the inner boundary closed region interface (K_5). For negative flux values a similar trend with increasing energy is see, but the correlation is weaker, and non-existent for positive flux values.

5.4 Discussion and Future Direction

Looking at the energy density time series, the internal triggers for energy change during the steady 2 hour solar wind intervals need to be studied more. Comparing the high density, high velocity case with the low density, high velocity case it seems that for some intervals rapid energy change occurs at the same time for both cases

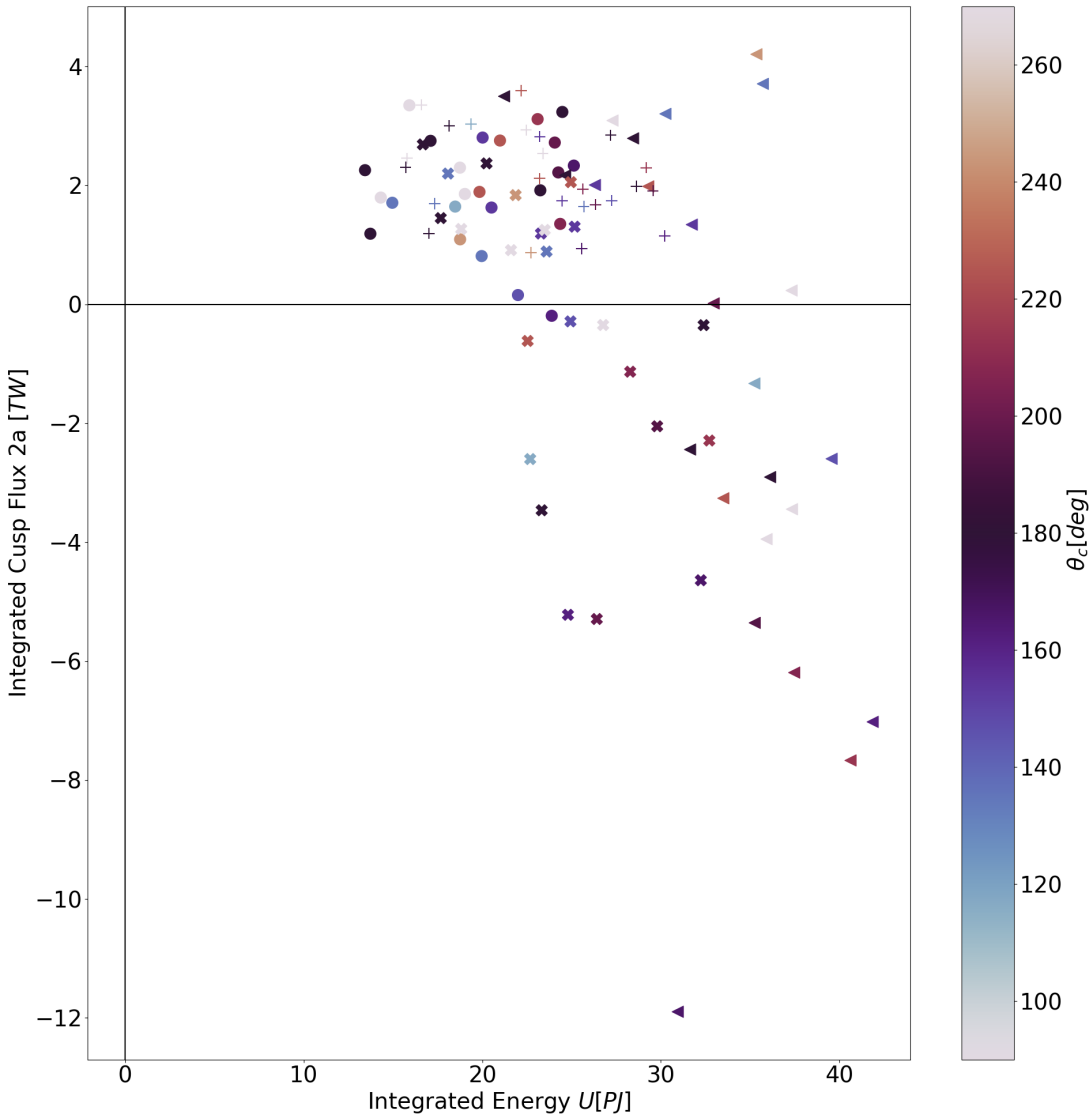

Figure 5.5: Integrated energy density U vs integrated internal cusp flux K_{2a} . Values averaged over the second hour of each interval to obtain single values for each case.

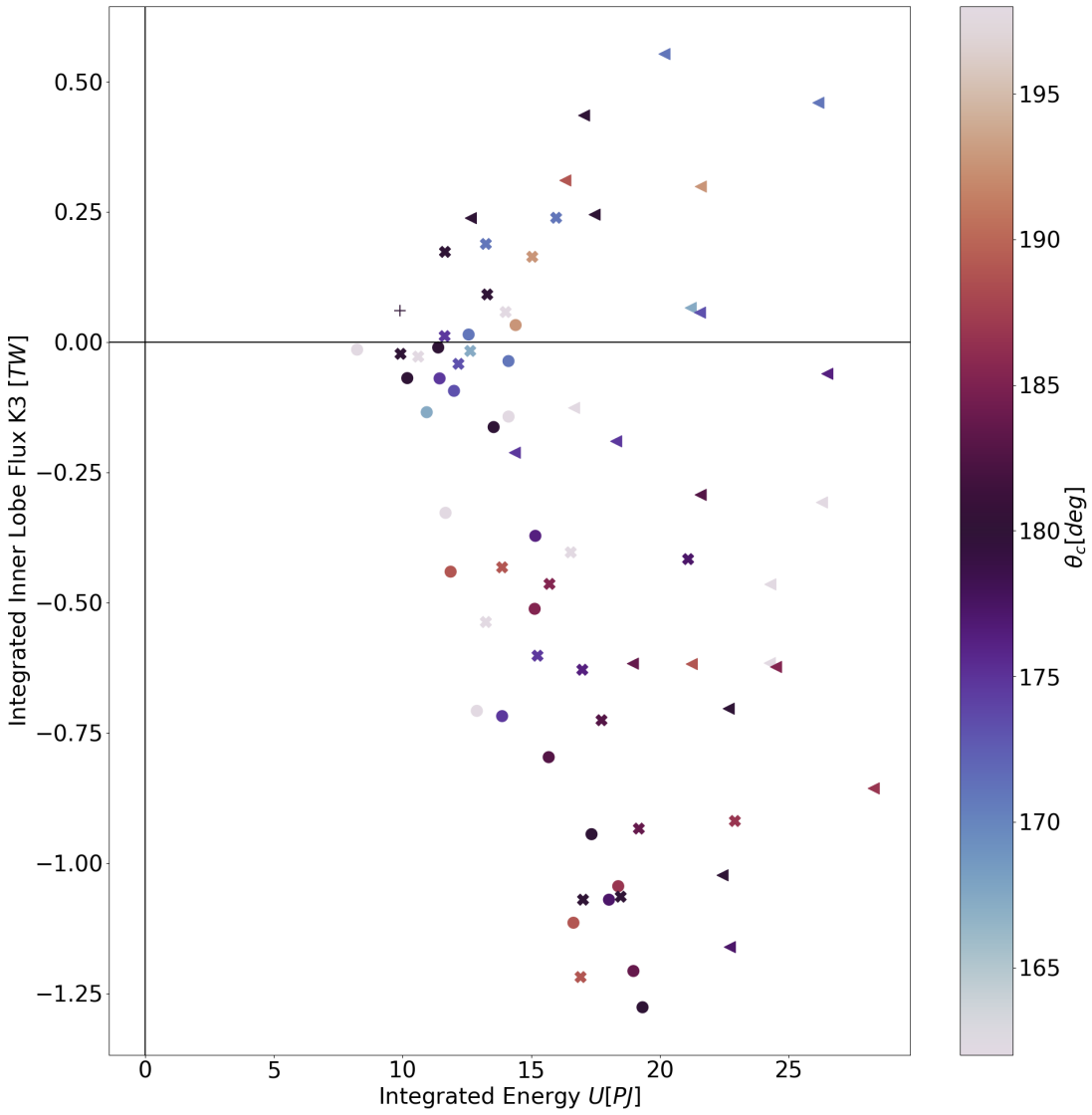

Figure 5.6: Integrated energy density U vs integrated inner lobe boundary flux K_3 . Values averaged over the second hour of each interval to obtain single values for each case.

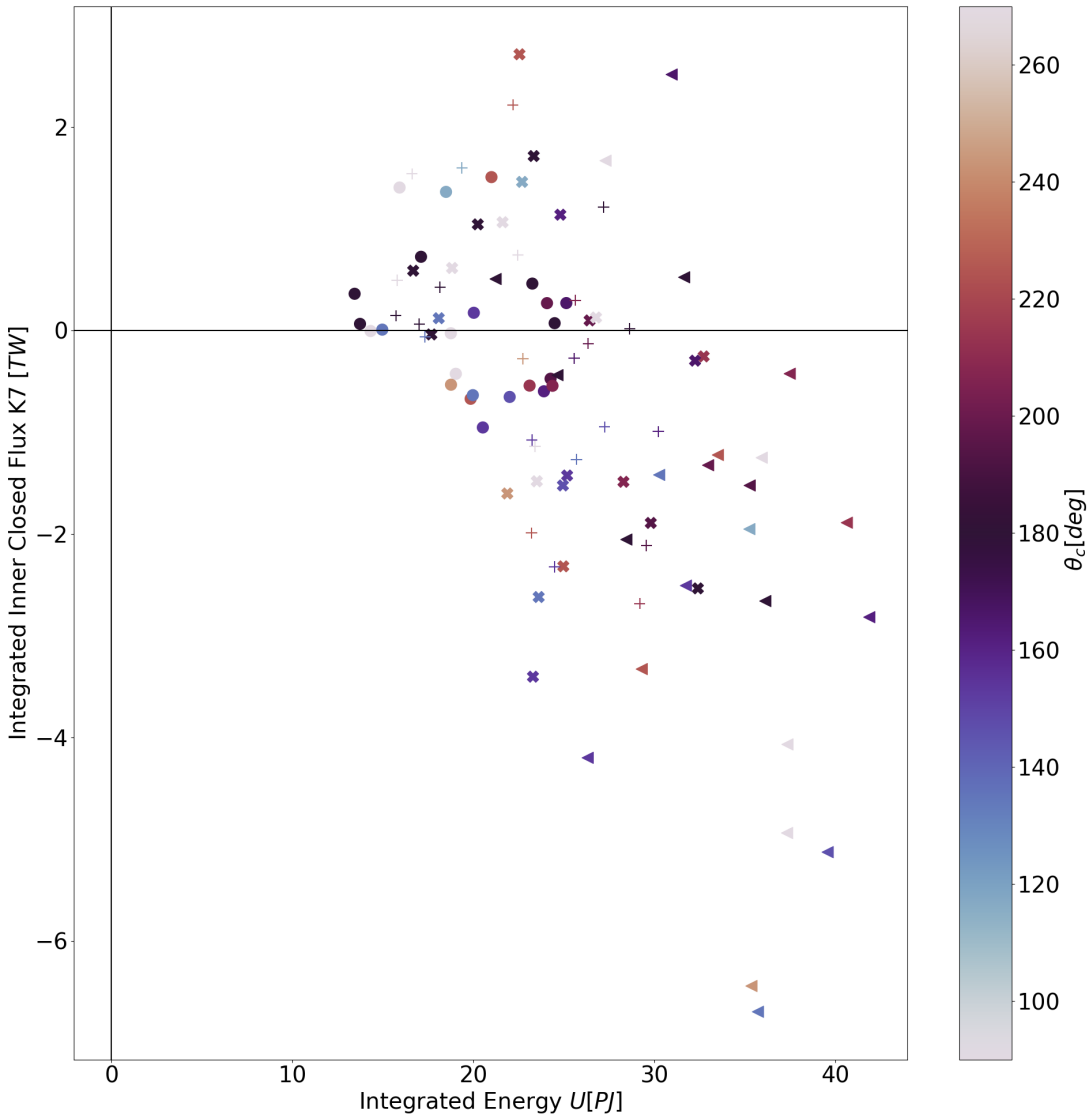

Figure 5.7: Integrated energy density U vs integrated inner closed region flux K_7 . Values averaged over the second hour of each interval to obtain single values for each case.

despite being at different energy levels. By digging deeper into a select number of these cases we may be able to find what conditions are being satisfied that allows the magnetosphere energy to change so drastically under steady driving conditions.

The high variability of the energy content and corresponding energy flux values within a single interval presents a challenge for definitively drawing conclusions about the relationships between the driving conditions, flux values, and internal energy state. As mentioned in the methodology, perhaps including the median results in addition to the mean, or otherwise altering the way each interval distribution is sampled could disentangle the high highly variable results.

When comparing the energy transport results following the methodology from chapter IV with coupling functions for energy input, it can be unclear which fluxes make the fairest comparison. For the E_{in} value, which also uses a magnetopause, it may seem that using the projected area magnetopause surfaces (K1 lobe sheath and K5 closed region sheath) would be the best choice, however the magnetopause defined by the flow-field technique is much longer in X_{gsm} extent. This means that more energy will be transported through the lobe sheath interface (or most equivalent section of the flow-field defined surface).

The additional energy input for a longer magnetopause should be captured by the tail cutoff energy flux. From the internal energy circulation pathway we've seen how energy that enters the lobes from the sheath falls into the closed field region and then convects sunward through closed region. If the tail cutoff plane intersects the closed region, then there would be energy flux injection that should contain all this additional energy. Future work will be to adjust the downstream distance of the magnetopause and carefully treat the comparisons between the flow-field traced and isosurface magnetopause in order to make more effective comparison.

In some of the averaged integrated cusp energy flux conditions reversed energy transport was found (from lobes to closed region), despite there being no cases with

positive IMF B_z or B_x to help facilitate lobe reconnection. These cases need to be further analyzed individually, and additional cases need to be run to understand what mechanism is causing the reversed energy flux transport. Without the change in the reconnection position, one possible explanation is that enhanced inner boundary injection into the magnetosphere is altering the internal energy flux transport.

While there is much analysis left to conduct with these results, the initial results indicate some interesting findings, especially about the internal energy dynamics of the magnetosphere.

CHAPTER VI

Conclusions and Future Work

6.1 Summary of Findings

In this dissertation work we developed new analysis and methods and used those methods to study energy transport in Earth's magnetosphere. The major questions that were the focus of this work were as follows:

1. How does energy couple from the solar wind to the magnetopause (injection and escape)

2. How is energy transported within the magnetosphere system

3. How does the solar wind and internal magnetospheric state impact the energy dynamics of Earth's Magnetosphere

In regards to 1, it was found that the energy transport between the solar wind and magnetosphere is not one way from solar wind into magnetosphere, but in fact a balance with energy being injected and escaping the magnetsophere system at all times. The spatial variation of this energy flux pattern was investigated and it was found that the sign of energy flux closely followed the local magnetic topology for southward IMF energy transport. This finding was distance from previous work, as the magnetopause definition used was able to distinguish between the open and closed magnetic topology and more closely follow the true magnetopause surface contour.

In addition it was found that the net energy transport is affected significantly by the magnetopause boundary motion. This will be important to consider as this analysis is replicated and extended; the volume integration approximation of the motional energy transport is sensitive to the output time step and so care will need to be taken when applying these techniques to new environments.

To address the second question, the magnetosphere was dissected to measure the internal energy flux at the inner boundary of the magnetosphere volume, and at the open-closed magnetic topology interface. It was found that significant magnetic energy is transported between open and closed topology regions of the magnetosphere that is able to inflate the magnetosphere lobes with large amounts of energy, despite lacking a mechanism to trap plasma particles. This recirculation was found to be sensitive to the IMF conditions in a slightly different way than the external interface energy flux.

And finally, to address 3 we ran over 70 ideal solar wind conditions in a steady profile for two hours, it was found that the internal dynamics of the magnetosphere are persistent even with two hours of steady solar wind. This presents challenges to the concept of a steady input output coupling function like relationship between the solar wind and magnetosphere, but it also presents an opportunity to study the internal mechanisms and develop new empirical models.

6.2 Discussion

The implications of energy flux as a balance through the magnetopause have two important consequences that make modeling the solar wind magnetosphere interaction more difficult. The first is that simply increasing the solar wind energy density does not increase the amount of net solar wind energy that enters the system. This effect has already been identified in coupling functions such as Newell, that have fractional exponent relations on the effective coupling, but now we understand that part

of the challenge is is that changing solar wind conditions affects both the injection and escape. Perhaps shifting the way we think about solar wind magnetosphere interaction in this way, we can conceptualize a new version of an empirical coupling function.

The second important consequence was the clear sign that reconnection physics does significantly change the energy transport dynamics. This was evident in the Starlink event study, where dual lobe reconnection was occurring in the simulation, but not in the observations. It will be critical to better understand how much fidelity in the reconnection physics are sufficient to achieve an accurate representation of the magnetosphere system in simulation.

The internal recirculation of energy in the magnetosphere revealed in this work explains how the lobes can contribute a significant amount to the total magnetospheric energy. In the single fluid MHD limit this region contains plasma that is dominated by the effective outflow from the inner boundary. Expanding beyond the single fluid limit, there may be multiple plasma populations that counter stream through this region and could significantly change the magnitude and dynamics of this internal circulation, and therefore the energy makeup of the magnetosphere.

6.3 Major Contributions

One contribution of this work is the methodology used to analyze energy transport in simulation output results. It was demonstrated that the definition of the magnetopause surface is critical to the results obtained for integrated energy flux. The magnetopause definition and the internal magnetospheric boundaries described here set robust and reproducible criteria that can be used with any simulation output regardless of the particular model or model settings.

Scientific contributions of this work quantify and expand our understanding of the relationship between the solar wind and Earth's magnetosphere. The magne-

topause energy flux results of a real storm event provide new insight into realistic energy coupling dynamics. By focusing on real event conditions and improving the magnetopause definition the full system perspective was able to be gained.

In terms of solar wind magnetosphere coupling this work sheds new light on the coupling function analysis by providing a new set of simulation results that are used to construct a coupling function fit. In addition, the energy transport pattern was investigated in detail with consideration for the magnetospheric state, which could lead to new concepts for a coupling function-like model (perhaps one that includes energy injection, energy escape, and magnetosphere energy content effects explicitly).

The International Solar-Terrestrial Physics program from 1995 set out to address the question of mass, momentum, and energy transport in Earth's magnetosphere; 28 years later this dissertation work takes a significant step forward towards this goal and provides an enabling capability to continue to pursue this objective. The energy transport analysis methods have already begun to be used with other simulation tools, such as with the Vlasiator code (*Ala-Lahti et al.*, 2022). Additionally, upcoming missions like the Solar wind Magnetosphere Ionosphere Link Explorer (SMILE) will hopefully be able to provide direct data model comparison opportunities for some of the global features like the magnetopause location that will further improve the usefulness of this work.

By better understanding global energy transport in Earth's magnetosphere we can better understand the potential for space weather hazards.

6.4 Ongoing and Future Work

Now, in no particular order, I will cover some of the ongoing and future projects that stem from this thesis work. Some projects have had significant progress, and others are only notional ideas.

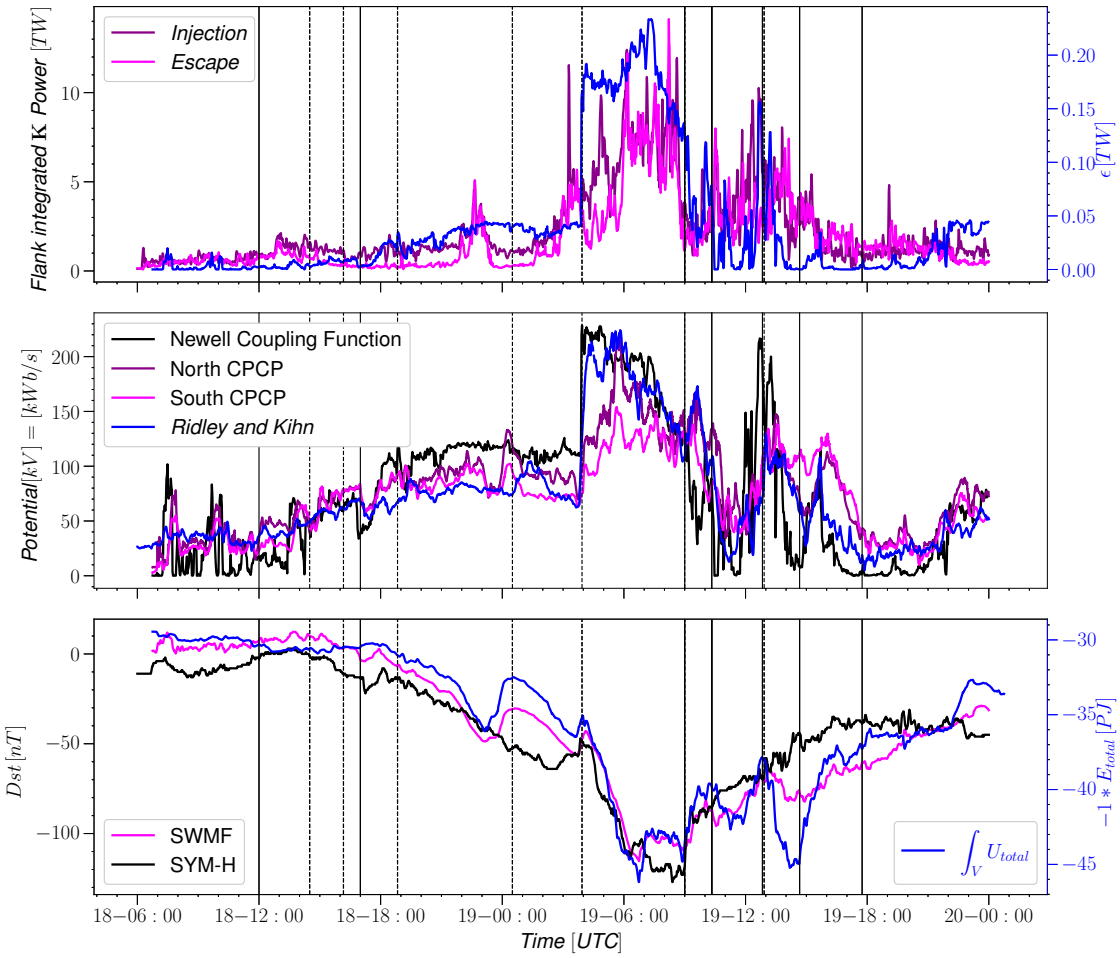

Figure 6.1: Caption

6.4.1 Virial Theorem

A finding that was not emphasized in chapter III discussion (it is featured in the published paper) is that of the connection between the Feb2014 storm SYM-H index results and the volume integrated energy in the volume enclosed by the magnetopause. Taking a close look we see a great correlation coefficient. The relationship between energy and magnetic perturbation has been studied historically for quite some time; the first formulation focused on energetic particles in the ring current known as the Dessler-Parker-Sckopke formula (*Dessler and Parker*, 1959), (*Sckopke*, 1966). This formula assumed particle drifts that depend on energy and yield predictable orbits to

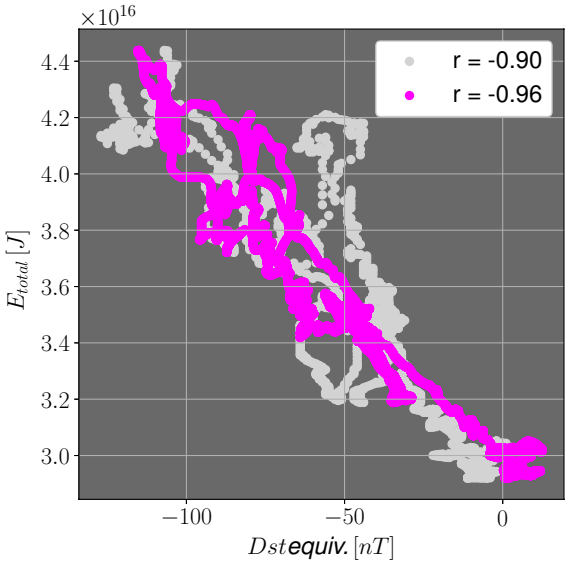

Figure 6.2: Caption

construct a relationship between the total magnetic perturbation of the dipole field ΔB (referred to as b) to the sum of all ring current particle energies.

Modifications and expansions were made since the original formula that are covered in a review paper by *Carovillano et al.* in 1973 (*Carovillano et al.*, 1973), and to generalize the relationship between magnetosphere energy and dipole magnetic perturbation the virial theorem was employed. Simply put, the virial theorem is a modification to the conservation of momentum equation that changes the force terms (momentum flux) into energy units. Later in 2006, *Vasyliūnas* derived the connection between the DPS equation and the virial theorem explicitly and explored some theoretical limits of ionospheric contributions (*Vasyliūnas*, 2006).

Using the simulation data, one could calculate the global magnetic perturbation using the virial theorem construction, but why do this when the Biot-Savart law integration can already quickly obtain an accurate answer?

The limitations of the Biot-Savart law integration comes in interpreting the perturbation results, while it is straight forward to identify which region of space is contributing to the magnetic perturbation, there is no conservation law that can be

used to track the evolution of current density. In the ideal MHD limit current density is solved using the ideal Ohms law using the magnetic field and bulk velocity $\frac{\partial \mathbf{B}}{\partial t} + \nabla \cdot (\mathbf{uB} - \mathbf{Bu}) = 0$ then the current density is recovered as the curl of $\mathbf{B}$, $\mathbf{j} = \frac{1}{\mu_0} \nabla \times \mathbf{B}$, but this relationship does not yield a direct transport equation for $\mathbf{j}$; the current density simply arises due to the evolution of the magnetic field. (This determination is made based on the form of equations given here, it may be possible to manipulate the equations in such a way to construct a transport of $\mathbf{j}$, which is another possible avenue for this investigation).

Alternatively, the virial theorem construction relates the magnetic perturbation to surface stress terms and volume energy terms; these terms are easily fed into the same analysis tools that have been developed. In this way it should be possible to track the contribution of magnetic perturbation via the transport of energy and boundary stresses, and explain how the magnetospheric processes directly participate in the magnetic perturbation signal. This would link the individual phenomena (reconnection, convection, ring current formation, substorm energy conversion, etc.) with the global consequence of magnetic perturbation.

I will now briefly step through a derivation of the virial theorem analysis with an eye for what the ideal MHD models can easily measure (the derivation is shown schematically in figure 6.3), then I will present the preliminary results of the virial calculation of b using simulation output compared with the traditional Biot-Savart law integration.

Start with the ideal MHD momentum equation.

$$\frac{\partial(\rho \mathbf{u})}{\partial t} + \nabla \cdot \left(\rho \mathbf{uu} + p\overline{I} + \frac{B^2}{2\mu_0}\overline{I} - \frac{\mathbf{BB}}{\mu_o} \right) = 0 \tag{6.1}$$

Then take the dot product of each side with the radial position vector $\mathbf{r}$ and integrate

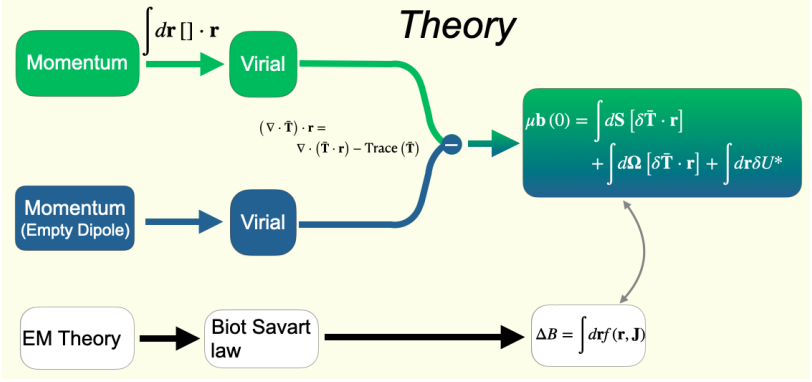

Figure 6.3: Schematic of the virial theorem derivation, ideal MHD momentum is transformed into a virial equation and combined with the results of an ideal dipole to obtain magnetic perturbation on one side and a collection of terms on the other.

the result over the volume (this is the virial part). The right hand side remains 0.

$$\int d\mathbf{r}\left[\frac{\partial(\rho\mathbf{u})}{\partial t} + \nabla\cdot\left(\rho\mathbf{u}\mathbf{u} + p\bar{I} + \frac{B^2}{2\mu_0}\bar{I} - \frac{\mathbf{B}\mathbf{B}}{\mu_o}\right)\right]\cdot\mathbf{r} = 0 \tag{6.2}$$

Then use the vector algebra identity $\left(\nabla\cdot\bar{\mathbf{T}}\right)\cdot\mathbf{r} = \nabla\cdot\left(\bar{\mathbf{T}}\cdot\mathbf{r}\right) - \mathrm{Trace}\left(\bar{\mathbf{T}}\right)$ and recognize a couple things. The first term on the right hand of this identity when combined with the divergence theorem allows rewriting the volume integrals into surface integrals. The second term with the trace is then equal to the volume integral of the energy density that has two components: $2U_H$ and U_B, twice the hydrodynamic energy and the magnetic energy. The capital U will now represent the volume integrated energy density with units of energy. Lastly for the time derivative term we can bring the radial dot product into the derivative and numerically evaluate as a central difference before integrating over the volume. This leads to the term $\frac{\delta(r\rho u_r)}{\delta t}$.

Moving the volume integrated terms to the right hand side we have the following:

$$\int d\mathbf{r}\frac{\delta\left(r\rho u_r\right)}{\delta t} + \int d\mathbf{S}\bar{\mathbf{T}}\cdot\mathbf{r} = 2U_k + U_B \tag{6.3}$$

The volume and surface integrals here are referring to the magnetosphere volume and the surface of the magnetopause that encloses that volume. This is an issue

because our simulation results stop at an inner radial distance. To work around this we consider an inner boundary with spherical geometry and repeat the same steps. In this case the volume is just enclosing the Earth (or a sphere at the inner boundary of our simulation domain), and the surface is a spherical surface referred to here as Ω . For this inner boundary we assume the magnetic components of the stress tensor $\bar{\mathbf{T}}$ dominate the surface integrals. Then by taking the difference between the whole magnetosphere (including Earth) and the Earth centered sphere, we can now consider the volume to be the space between the sphere and the magnetopause (we have 100% coverage of in our simulation output), and the surface integrals have a component on the magnetopause as well as the inner sphere boundary.

Lastly we repeat this construction a third time, now for an ideal empty dipole within the same spatial limits (between the spherical inner bound and magnetopause), then by subtracting the result of the empty dipole from the real magnetosphere and rearranging terms we get the full virial theorem magnetic perturbation equation that is given by 6.4. $\mathbf{B}$ is the full magnetic field and $\mathbf{B_d}$ is the dipole field. U_b refers to the magnetic perturbation energy $U_b = \left(\mathbf{B} - \mathbf{B_d}\right)^2 / 2\mu_0 = U_B - U_{B_d}$.

$$\begin{aligned}
\mu \cdot \mathbf{b}\left(0\right) = & -\int d\mathbf{r} \frac{\delta\left(r\rho u_r\right)}{\delta t} \\
& -\int d\mathbf{S} \cdot \left[\rho \mathbf{u}\mathbf{u} \cdot \mathbf{r} + \mathbf{r} P_{th}\right] \\
& -\int d\mathbf{S} \cdot \left[\mathbf{r}\frac{B^2}{2\mu_0} - \mathbf{r}\frac{B^2}{2\mu_0} + \mathbf{B}\mathbf{B_d} \cdot \mathbf{r} - \mathbf{B}\mathbf{B} \cdot \mathbf{r}\right] \\
& -\int d\mathbf{\Omega} \cdot \left[\rho \mathbf{u}\left(\mathbf{u} \cdot \mathbf{r}\right) + \mathbf{r} P_{th} + \mathbf{r}\frac{b^2}{\mu_0}\right] \\
& + 2U_H + U_b + U_G
\end{aligned} \tag{6.4}$$

We compare the virial results to the magnetic perturbation calculated using the

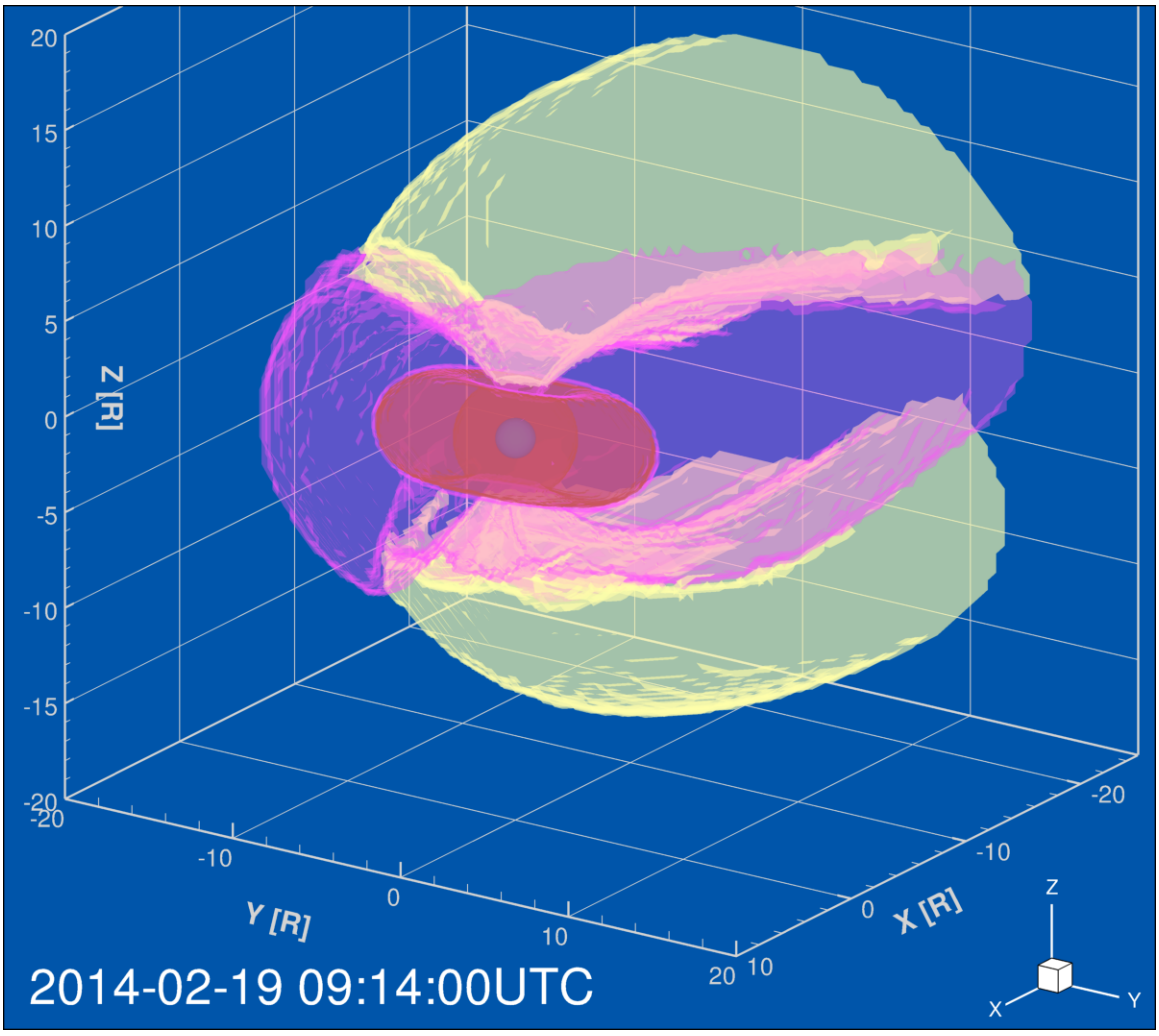

Figure 6.4: Magnetosphere (translucent) volumetric regions colored by region. Vanilla: lobes, strawberry: outer-closed region ($L > 7$), chocolate: ring current region ($L < 7$).

Biot-Savart law given in 6.5.

$$\mathbf{B}(\mathbf{r}) = \frac{\mu_0}{4\pi} \iiint_{\mathcal{V}} \frac{(\mathbf{J} d\mathcal{V}) \times \mathbf{r}'}{|\mathbf{r}'|^3} \tag{6.5}$$

The surface and volume integrations were performed on the same magnetopause/magnetosphere as defined in chapter IV, with the split of the closed region into an outer closed region and ring current region defined by fixed L shell $L < 7$. The same Feb 2014 study from III is used, a snapshot of the magnetosphere is shown in figure 6.4. The prelim-

inary results are shown in figure 6.5, while there are similarities between the virial and Biot-Savart derived magnetic perturbations they differ quite significantly during the recovery phase. By repeating this analysis for the Starlink event and the ideal runs from V we can determine if the discrepancies are due to specific solar wind conditions, and can assist identifying any potential errors in virial theorem calculation. The next steps for this work is to review the analysis steps and validate the integration techniques while expanding to more events. When the methods are finalized we can address whether the virial theorem magnetic perturbation yields as consistent results as the Biot-Savart calculation, and if it can be used to link energy transport to magnetic perturbation consequences.

6.4.2 Parameter Study Continuation

Another area for future work is the continuation of chapter V, expanding the analysis to broader range of inputs as well as modifying the underlying simulation settings.

Magnetic reconnection in ideal MHD simulation is affected by the numerical resistivity that is partially a function of the local grid resolution, by changing the grid resolution we can determine if the results from chapter V are sensitive to this parameter. This will tell us how generalizable the results from that study are. Figure 6.6 provides an example of 1/16th R_e grid resolution on the magnetopause boundary using the Adaptive Mesh Refinement technique. The boundary waves are clearly much more defined and the four field junctions (green isosurface) reveals finer structure to the separator line that could affect the magnetopause energy transport. For simulation inputs, more extreme solar wind conditions can be run to explore the upper limits of the energy transport process, as well as time varying signals with to explore whether resonant solar wind driving can further change the solar wind magnetosphere coupling process.

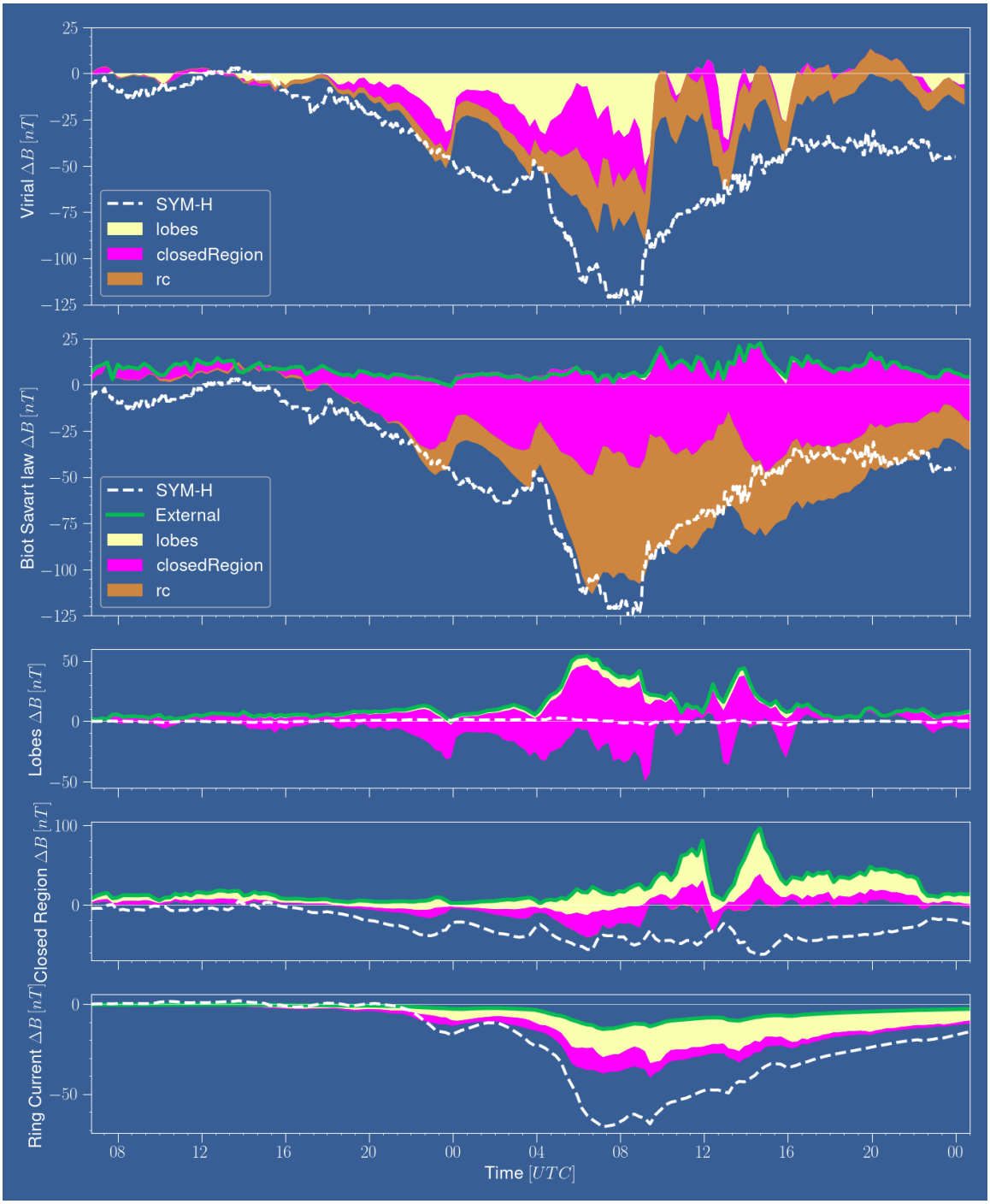

Figure 6.5: Time series of magnetic perturbation $b = \Delta B$ calculated using the virial theorem (top panel) and the Biot-Savart law (second panel) stacked by the regional contribution. Bottom three panels show the regional results of the virial calculation stacked starting with the green curve (boundary stresses) then adding hydrodynamic energy (vanilla), magnetic perturbation energy (strawberry), and distance weighted momentum (chocolate). For details of the simulation setup and solar wind conditions see chapter III, section 3.4.

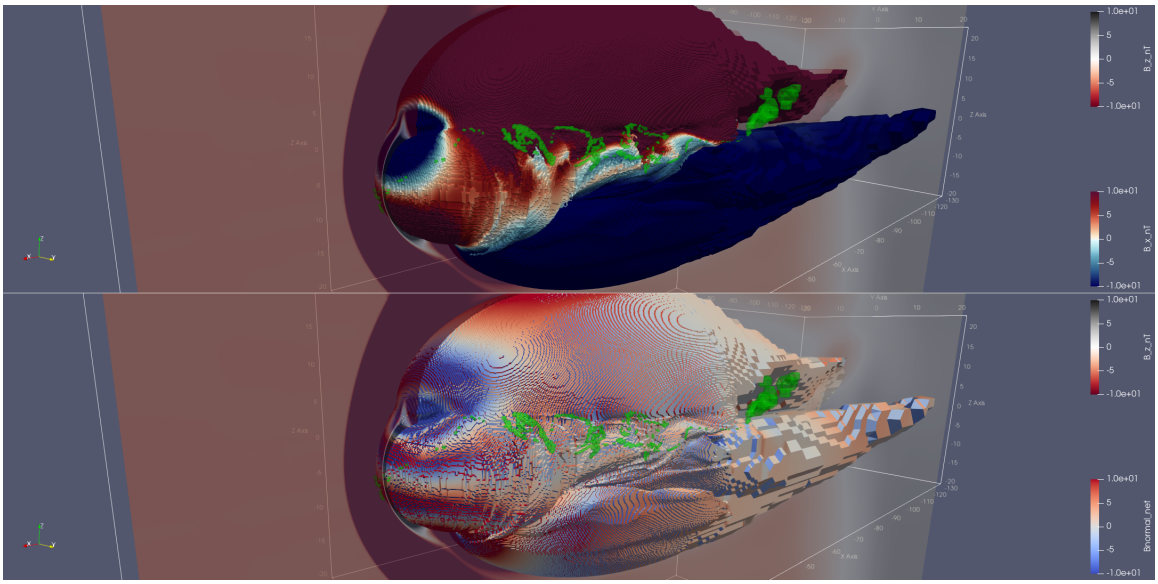

Figure 6.6: Output of BATS-R-US ideal MHD simulation with Adaptive Mesh Refinement (AMR) to a resolution of 1/16th R_e. Magnetopause shown in with contours of B_x (top panel) and $\mathbf{B} \cdot \mathbf{n}$ magnetic field normal to the surface. Green isosurface shows the four field junction pattern.

6.4.3 Multifluid MHD and Polar Wind Transport

It was found that significant energy injection occurred from the inner boundary during storm time, which was due to the effective plasma outflow from the inner boundary of the simulation. This effect should be studied in more detail by coupling SWMF to the Polar Wind Outflow Model (PWOM) (*Glocer et al.*, 2009b). By changing the outflow characteristics, there should be direct changes to the energy recirculation between the lobes and closed region that would directly affect the magnetosphere system size and energy escape.

Another way to study the effect of the plasma outflow from the inner boundary would be to use multi-fluid MHD with either additional ion species, even with the same composition, to allow for counter streaming effects. Counter streaming populations could affect the internal recirculation of energy in the magnetosphere, which would modify the overall solar wind magnetosphere coupling values.

6.4.4 Ionosphere Polar Cap Flux Connection to Energy Transport

The ionosphere is tightly coupled to the magnetosphere, but was not the focus of this dissertation work. Future work should be to explicitly explore the ionospheric dynamics that occur in conjunction with the magnetosphere energy transport.

Specifically during solar wind magnetosphere coupling the polar cap area and magnetic flux changes, as the topology of the magnetosphere changes. By measuring the polar cap flux in the dayside and nightside portions, and accounting for the transport across the dipole terminator dividing line, the total dayside and nightside reconnection rate can be measured. Figure 6.7 shows how the polar cap can be split up in order to construct the dayside and nightside global reconnection rate values. Figure 6.8 shows and example of the magnetic flux crossing the dipole terminator during single cell ionospheric convection.

In addition to global reconnection rate, the ionosphere solution provides information about the plasma convection pattern and field aligned currents that can directly control magnetosphere processes.

6.4.5 Reconnection Impact on the Transport Patterns

As previously mentioned the reconnection physics play an important role in the energy transport processes studied in this work, in order to understand in more detail exactly how they affect the global pattern the reconnection physics can be treated more explicitly. By adding finite resistivity to the model, known as resisitive MHD (as opposed to ideal MHD) we can study the impact of resistivity on the solar wind magnetosphere energy injection and escape results.

Another way to treat the reconnection physics is with kinetic techniques like the embedded particle in cell method (*Chen et al.*, 2017). This approach has the benefit of being self consistent, though requires more computational resources.

Even using ideal MHD as this work does, future improvements could include

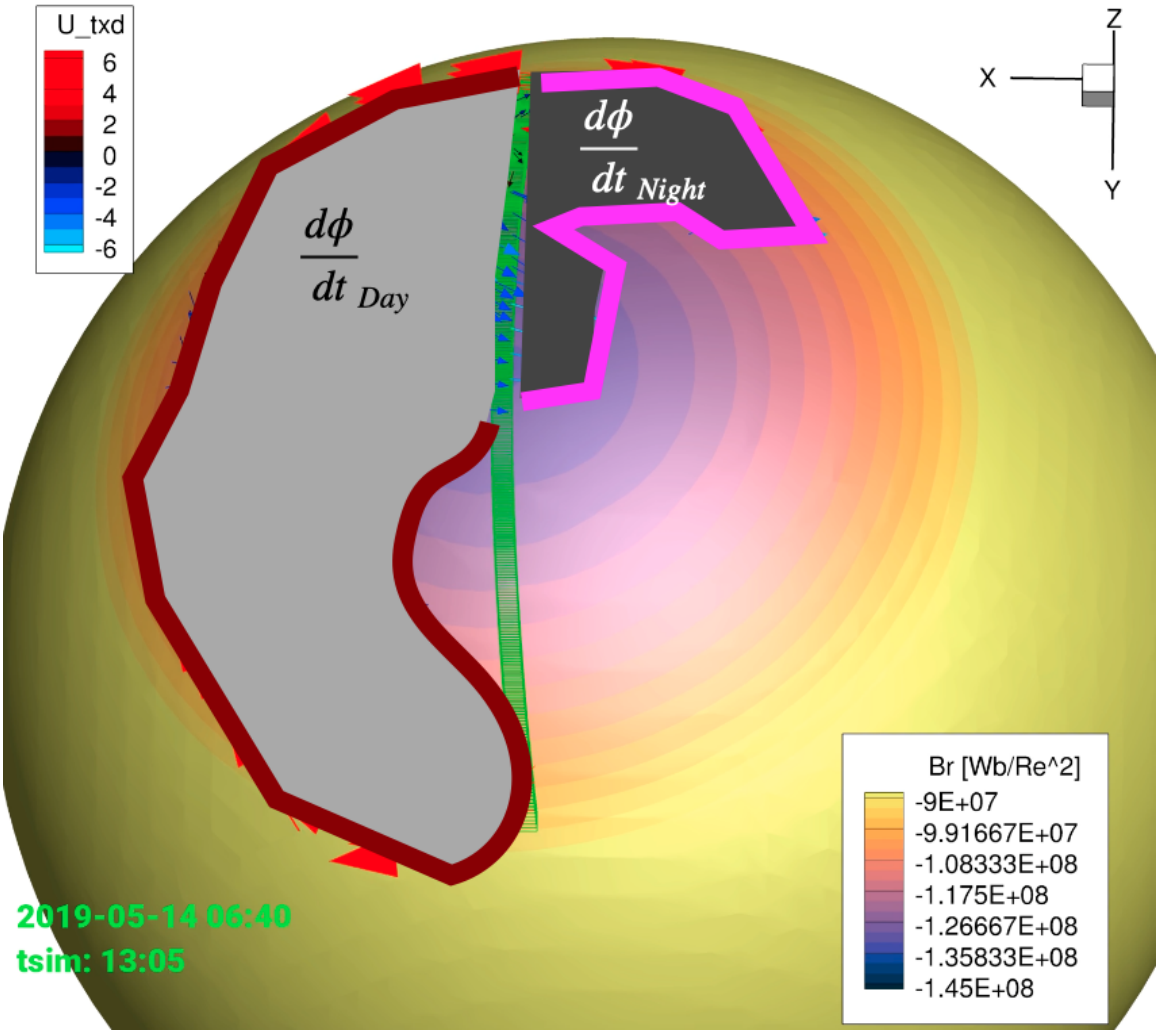

Figure 6.7: Ionosphere polar cap visualized with dayside (light grey) and nightside (dark grey) outlined. The dayside global reconnection rate is how much flux crosses the red outline, and the nightside reconnection rate is what crosses the magenta line. By measuring the change in the dayside and nightside area and accounting for transport across the dipole terminator in green, these reconnection rates can be quantified.

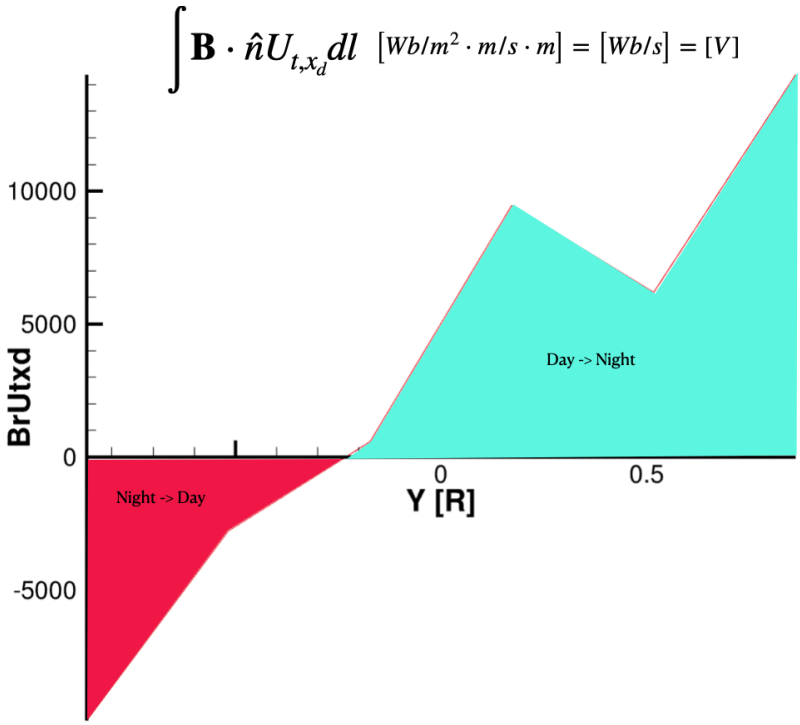

Figure 6.8: Results from one time step of the magnetic flux across the dipole terminator during single cell ionospheric convection.

explicitly measuring the local effective numerical resistivity in each cell. A preliminary attempt was made to estimate the resistivity by using just the output variables, but it was found that information from the limiters during the finite volume solution step is required, so modifications to the source could will be necessary. By having the numerical resistivity value, the same comparisons between resistivity and the energy transport rate can be made and the effects of grid resolution and limiters can be seen more clearly.

6.4.6 Community Dissemination of Energetics Tools

One of the great aspects of working in the field of space science is the spirit open collaboration and community focused collective efforts. One of the ways this takes place with simulation tools is through the Community Coordinated Modeling Center (CCMC) that hosts a variety of simulation, analysis, and visualization tools that are

publicly available and can even be run on request.

An important future step for the tools developed in this dissertation is to integrate them with CCMC, either directly through the CCMC website or at least make them available in an open source package that can be used in conjunction with CCMC tools. The primary challenge to this will be to make the 3D software (Tecplot, Paraview) available and robust so that minimal effort is required to perform the analysis calculations with SWMF output. Currently only a specific Paraview version (5.11) can be used and must be modified to link python packages that do not ship with the official build in order to perform the calculations. Tecplot is even worse as it is licensed software that cannot be publicly distributed.

Another important realization that came from this work is the steep learning curve involved with using Tecplot and Paraview tools. Future work could involve hosting workshops and creating tutorial information that allows future users to use these tools more effectively with less start up time.

6.4.7 Flux Transfer Event Significance for Energy Transport

Another element to energy transport not covered in this work is the interaction of the magnetosphere with flux rope like structures called Flux Transfer Events (FTE's). Future work could include studying the energy transport process on the magnetopause with and without various types of FTE structures present to better understand how these features affect the transport of energy.

Paul et al. has developed an FTE detection algorithm using simulation output data (*Paul et al.*, 2022), and an initial case study was performed using ideal SWMF simulation data. For this demo ideal MHD SWMF was run with 1/16th AMR grid, then an FTE structure was identified from the simulation output. Once the FTE cells are identified the information is fed back to the SWMF output and the magnetopause and FTE structures can be analyzed together. Figure 6.9 shows a snapshot from the

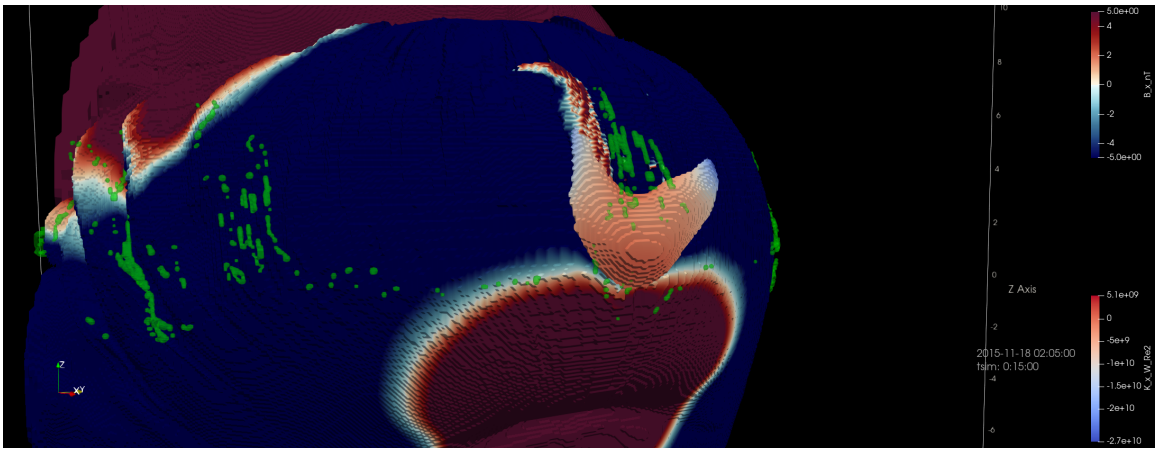

Figure 6.9: identified FTE on the magnetopause surface. Magnetopause contoured by magnetic field B_x, FTE contoured by total energy flux in the X direction K_x.

simulation showing the magentopause surface and an isosurface of the FTE structure.

Future work will involve developing this analysis further so that FTE evolution can be studied and FTE effect on energy transport can be investigated.

6.4.8 Bow Shock and Sheath Modulation of Energy Transport

The starting point for the energy analysis in this work was the magnetopause surface, but important energy conversion processes occur upstream as the solar wind flow is processed by the bow shock and travels through the magnetosheath. Future work could study these effects by using similar analysis methods of calculating integrated energy flux, but applied to the magnetosheath as a volume, in order to understand how energy conversion occurs. Figures 6.10 and 6.11 shows how this analysis might be preformed, with the magnetosheath defined as the region between the bow shock and magnetopause.

Because the flow is sub-magnetosonic as it crosses the bow shock, the perturbations caused by energy escape from the dayside closed region magnetosphere can propagate back through the sheath region. This means that the characteristics of the magnetosheath are affected from both the upstream solar wind and the magnetopause boundary.

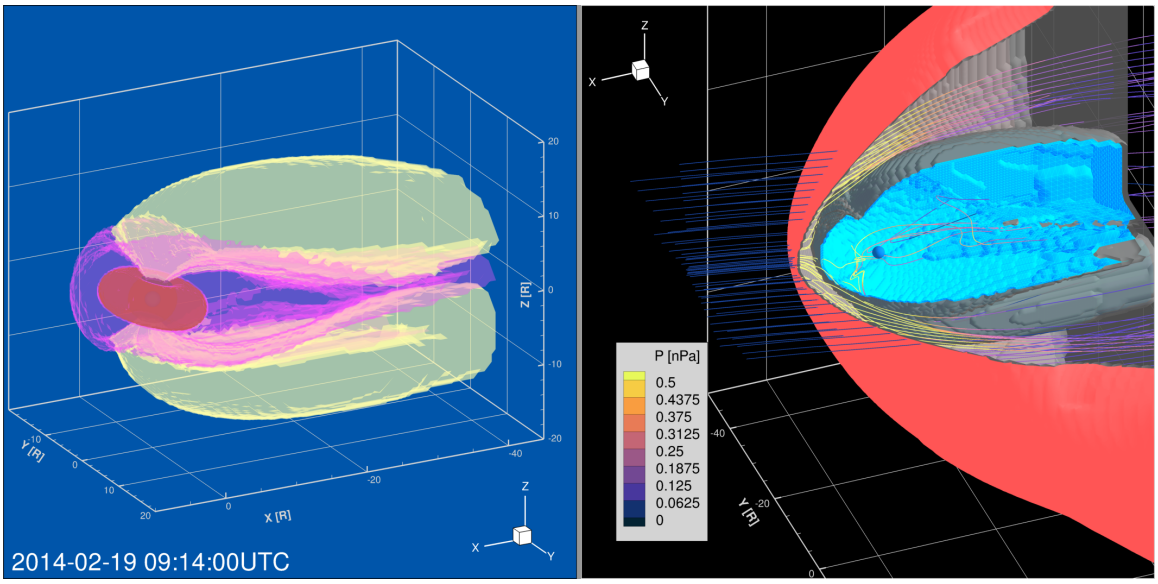

Figure 6.10: Magnetosphere regions (left) along side quarter cut of magnetosphere with the bow shock identified (right), traces show ideal MHD flow field **u**, contoured by thermal pressure P_{th} showing pressure increase as plasma crosses the bow shock.

Studying the magnetosheath at Earth is also important because of the similarities to the sheath regions of ICME. By learning more about ICME sheaths we can better understand events that may cause significant geomagnetic storms. figure showing the total energy flux traces with increased energy density within the magnetosheath.

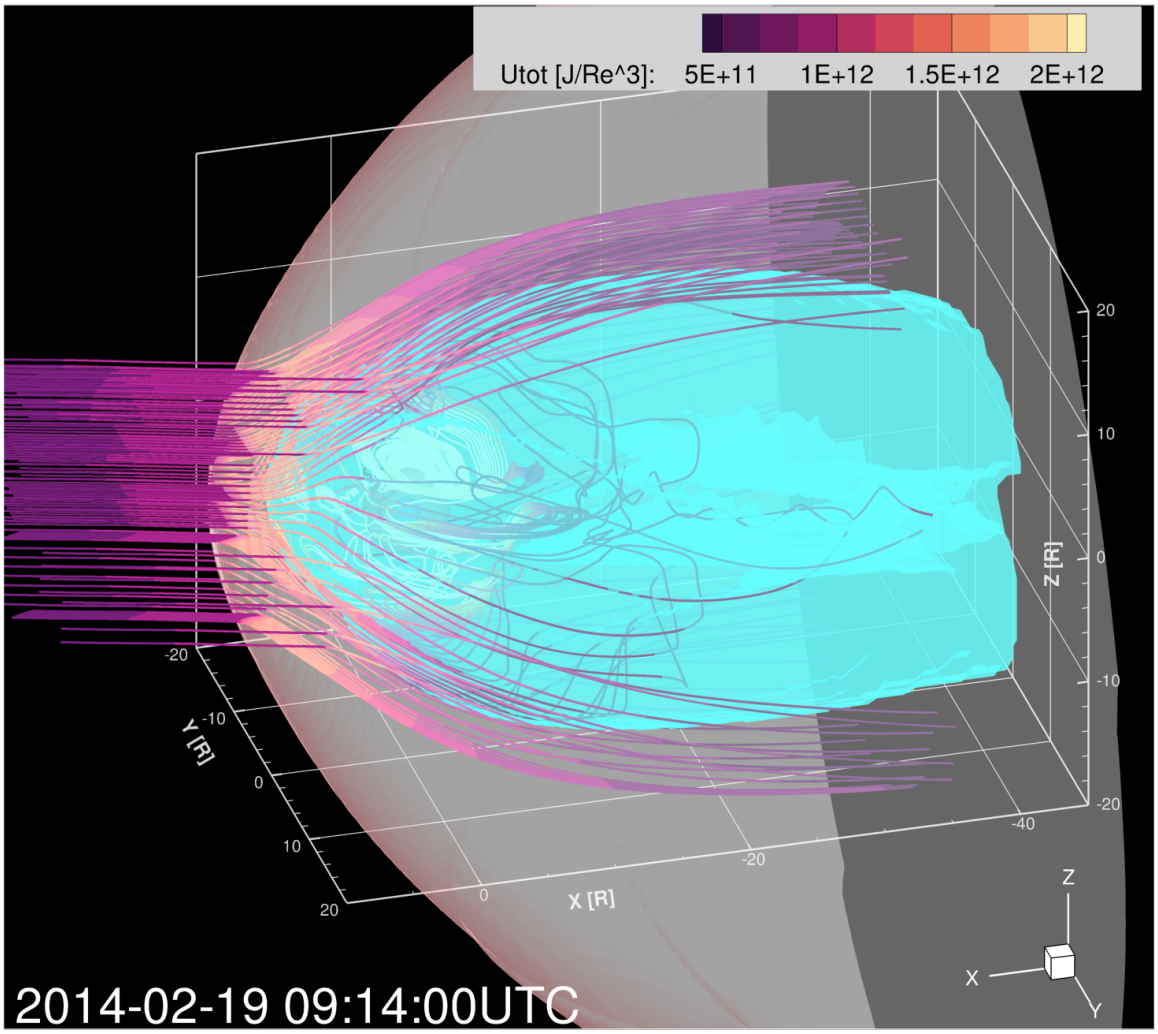

Figure 6.11: Bow shock and magnetopause shown with total energy flux **K** traced from the solar wind through the sheath and into the magnetosphere, contoured by total energy density U.

APPENDIX

APPENDIX A

Error in Divergence Theorem Calculation

The divergence theorem states that the volume integral of the divergence of some vector field $\mathbf{F}$ can be calculated by taking the surface integral of the normal component of the vector field along the boundary: $\int_{dV} \nabla \cdot \mathbf{F} = \int_{dS} \mathbf{F} \cdot \mathbf{n}$. This in combination with our conservation law for some quantity $\frac{dU}{dt} = \nabla \cdot \mathbf{F}$ means that by integrating the fluxes on all bounding surfaces of some volume we can directly obtain the rate of change of that quantity within the volume. Adding up the original values from table A.1 we clearly show a massive over-prediction of all types of energy flux through the surface. For the whole magnetosphere the energy flux integrated in time = 37PJ, whereas the actual change = 13PJ. This is an error of nearly 200%. Figure A.1 shows this final error value accumulate by plotting the actual volume energy along side the predicted volume energy given by simply the change in energy flux.

Looking at the instantaneous flux values as a time series (Figure A.2)it seems the over prediction is consistent with errors that mostly stay between $0 - 2TW$ in the negative direction (too much flux into the volume), which can be over half of the total, individual contributions to flux (not the net but the pieces) are larger still $\sim 4TW$ so really error could be a smaller fraction of any number of partial surface fluxes and compounded by the summing operation.

To rule out the dynamic surface motion let us consider a set of motionless concentric spheres as a simplified magnetosphere with one at 3Re (inner) and one at 10Re (outer). Using this geometry with the same flow field solution we still see bias during main phase albeit with more consistent steady error values, again on the order of $\sim 2TW$.

Because this steady object also exhibits error in this calculation maybe the issue lies with the surface quality (non-smoothness). It turns out that the discretization of the state variable (1==in and 0==out) leads to more blocky isosurface representation (see another Appendix). To compare the discretized and non-discretized states, let's repeat the concentric spheres analysis using the continuous value of R with an iso value of 3 and 10, rather than defining a state with iso value 1. The resulting concentric spheres are now visually much smoother (Figure A.4) and the area comparison to the analytic area error was reduced from $\sim 10Re^2$ to $0.01Re^2$.

Surprisingly, as Figure A.3 shows, the improvement of the quality of the isosurface still does not make any appreciable improvement in the surface flux vs central difference comparison of total energy transport.

If the surface and geometry are not the issue then it must be the flow field (the only other quantity in our calculation). Using the same geometry from the blocky concentric spheres test we now shift the geometry to not surround the origin but instead out in the solar wind flow region of the simulation, $[XYZ{:}10, 20, 20]$, here the grid resolution is still reasonable ($1R_e$ spacing). As shown in Figure A.7 the difference between integrated surface flux and central difference volume flux become much smaller $< 0.1TW$. It would seem that the issue is not with the entire real flow field, but perhaps just with the flow field in the domain that contains the inner boundary.

Maybe because the isosurface is using the point values from the dual grid, while the volume integrals are including the volume in the whole cells using the original

grid cell centers, there could be small errors in the fact that the whole cell is assumed to have the same state value. In fact this could lead to an error in the volume energy density for the innermost cells where the magnetic field strength becomes very large.

To test this hypothesis let's run a few more cases with only the inner boundary shifted. The geometry is now adapted so that the inner boundary sphere is pushed out from $3R_e$ to 3.5, 4, 4.5, and $5R_e$, now zooming in on a portion of the main phase that consistently exhibits biased flux errors. The half values are omitted for clarity but fall between the integers. Figure A.7 shows the results, indicating that the error first decreases in magnitude then returns with the apparent optimum value near $4R_e$. A brief binary search to a resolution of $1/8R_e$ showed only marginal improvements with a best value of $3.875R_e$ so $4R_e$ was left as the new selection.

Now repeating the actual magnetosphere analysis with the inner (analysis) boundary set to $4R_e$ we see that indeed the instantaneous and cumulative errors are reduced. Figures A.1 show the new results using the updated inner boundary.

Since the errors in both the concentric spheres and the real magnetosphere didn't become as small as the solar wind sphere test, there seems to be some other effect at play. If we look at two final tests with the same block concentric sphere geometry located now directly in the tail (XYZ:$-18, 0, 0$), and another mostly in the open flux lobes (XYZ: $-18, 0, 14$) we see that the errors reduce towards the solar wind levels as we move away from the inner boundary and further as we move away from closed field lines. From these additional tests we conclude that the inner boundary plays the most important role, but simply being in the magnetosphere with these simulation settings yields an overestimation of the energy flux magnitudes.

It may seem to the reader that the error values are still quite substantial with a resulting accumulation value of $-12PJ$, which is nearly 100%. Framing this error in another way, however, the situation looks much less dire. Figure A.1 shows the results of the actual volume integrated energy, the demonstrated time integrated

approximate derivative, and a 1 minute prediction using the integrated flux values. In this formulation rather than accumulating the error we see that surface flux values are simply small deviations in the slope of the curve.

But the question remains, how much energy IS actually passing through each surface throughout the whole main phase. We've seen that the inner boundary might be a sensitive spot compared with other boundaries, so perhaps the error is not evenly distributed, but even if it were these results indicate that there is no preferential treatment something like a dayside or nightside mapped surface. Or an open-closed boundary, since the concentric sphere test changed the relative areas of each of those splits with no change in the direction of bias. While the question of error in the divergence theorem calculation should receive more detailed study for now it would seem the results of the table A.1 stand, insofar as the relative magnitudes between the values, if not the values themselves.

Considering what might be causing the flux integration bias the reader might be tempted to consider the numerical scheme an couplings between the GM and IM modules. In both open and closed magnetosphere regions the non-conservative criteria is used where the momentum conservation equation is used along with a pressure floor condition at the expense of energy conservation. And in the closed field lines there is coupling to the Inner Magnetosphere module that adjusts the plasma pressure in the Global Magnetosphere module. Both of these effects, however, would act to increase the internal energy of the magnetosphere directly. This would have the opposite biased effect and so it cannot be the answer. Since what we see is too much flux flowing into the volume, and not enough energy actually being there, we can be confident in saying these effects are not the cause of the bias.

The next steps to close out this line of study is to employ analytic flow field functions and extremely high time resolution output of a real flow field to get to the bottom of where and why the divergence theorem exhibits this bias. It may be the

Table A.1: Time integrals over the storm main phase of the hydrodynamic energy flux, Poynting flux, and total energy flux. Modified from publication results of 2022-02-02 storm (inner analysis boundary at $3R_e$.

	Energy $[PJ]$	$\int Hdt$	$\int Sdt$	$\int Kdt$
1	Lobes→Sheath	+5.14	–97.05	–91.91
2a	Closed→Lobes (day)	+11.59	+130.70	+142.29
2b	Closed→Lobes (night)	–2.98	–215.83	–218.81
3	Lobes→Inner	–0.43	–24.32	–24.75
4	Lobes→TailCut	+7.01	+3.94	+10.96
5	Closed→Sheath	+46.68	+14.59	+61.27
6	Closed→TailCut	–10.57	–6.21	–16.79
7	Closed→Inner	+2.77	+20.17	+22.94

case that the time step output of one minute is too short to resolve an oscillatory energy flux pattern at the inner boundary where the waves speeds are high, which results in an aliased signal. By having an analytic solution to compare to we can directly see what kinds of signals might cause the divergence theorem calculation to break down for a given time resolution, and even provide guidance for a minimum output cadence given simulation settings and output plasma parameters.

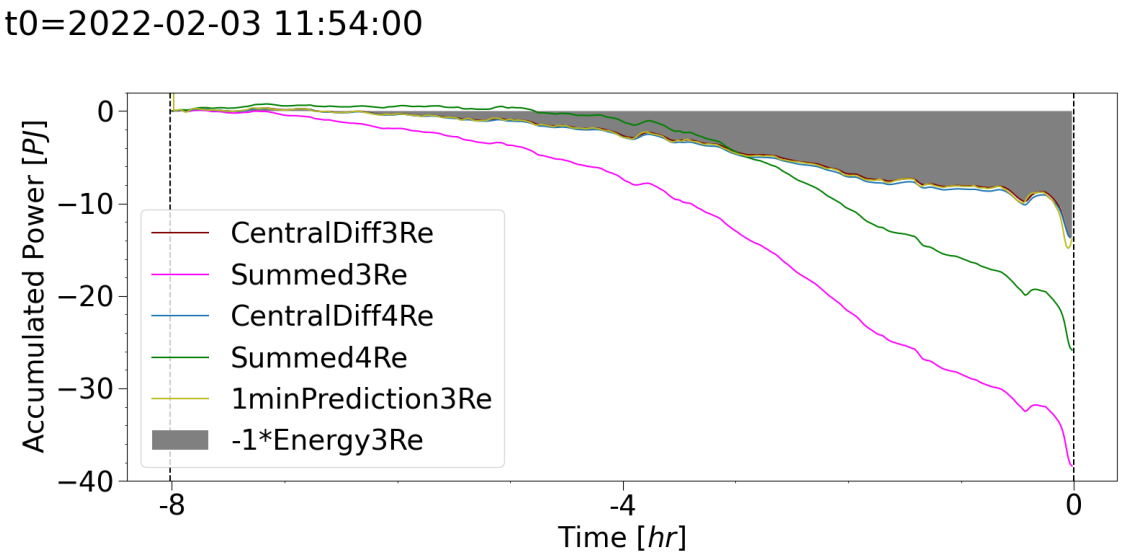

Figure A.1: Time series of main phase of storm showing the accumulation of error values when integrating surface flux results forward in time. The external surface flux terms (static and motional) are combined and integrated forward in time and compared to the actual change in the volume. To demonstrate that it is not simply a time integration issue, a central difference of the volume energy is taken as an approximate flux transport and that approximate value is also integrated forward in time. Clearly the net flux transport is biased in the over prediction direction for the main phase of this event. Moving the inner boundary to $4R_e$ cuts the accumulated error by about half. Finally an alternative formulation is plotted that takes the previous energy state value and plots the predicted energy given the previous energy flux values.

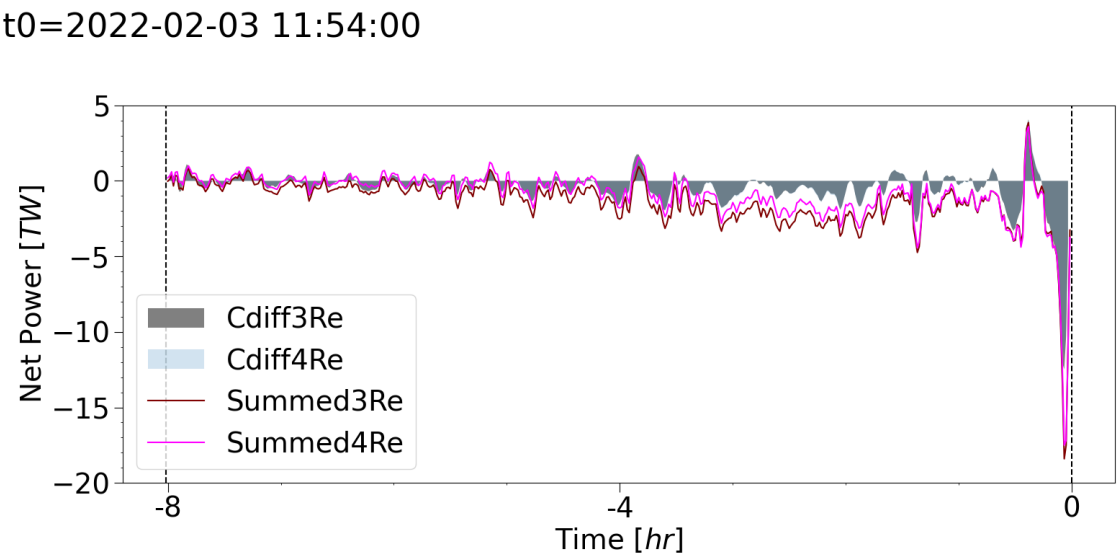

Figure A.2: Time series of main phase of storm showing the instantaneous error values of the external net energy flux. The external surface flux terms (static and motional) are combined and compared to a central difference approximation of energy flux using the volume integrated energy of the whole magnetosphere. Clearly the net flux transport is biased in the over prediction direction for the main phase of this event.

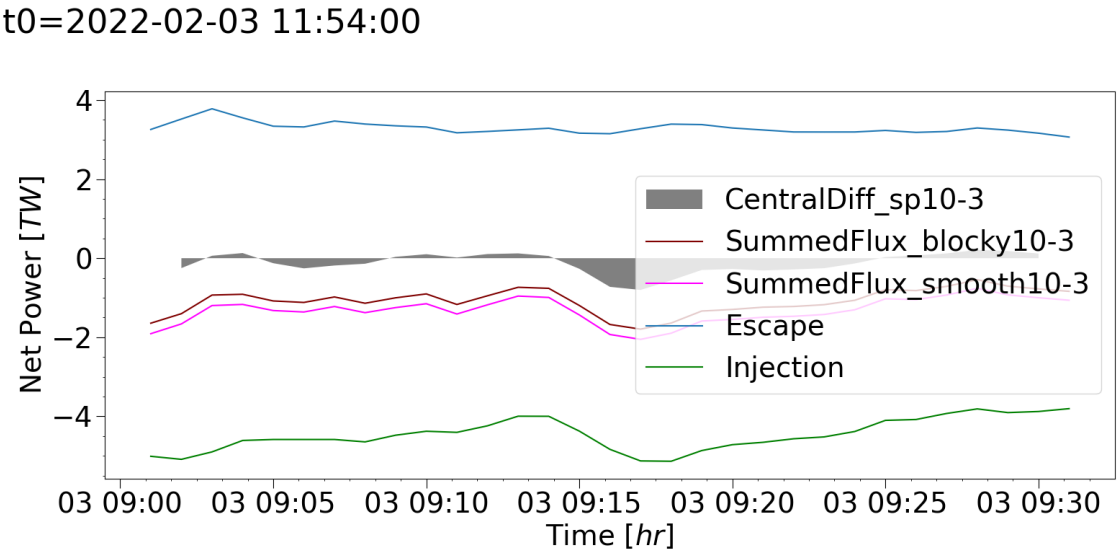

Figure A.3: Initial test with static concentric spheres at $3R_e$ and $10R_e$ creating simplified magnetosphere. Volume integrated energy derivative is approximated with central difference to find error between surface flux estimated energy change and actual energy change. Injection and escape also shown to indicate that both the net values and the error is much smaller than the amount of energy exchanged in either direction.

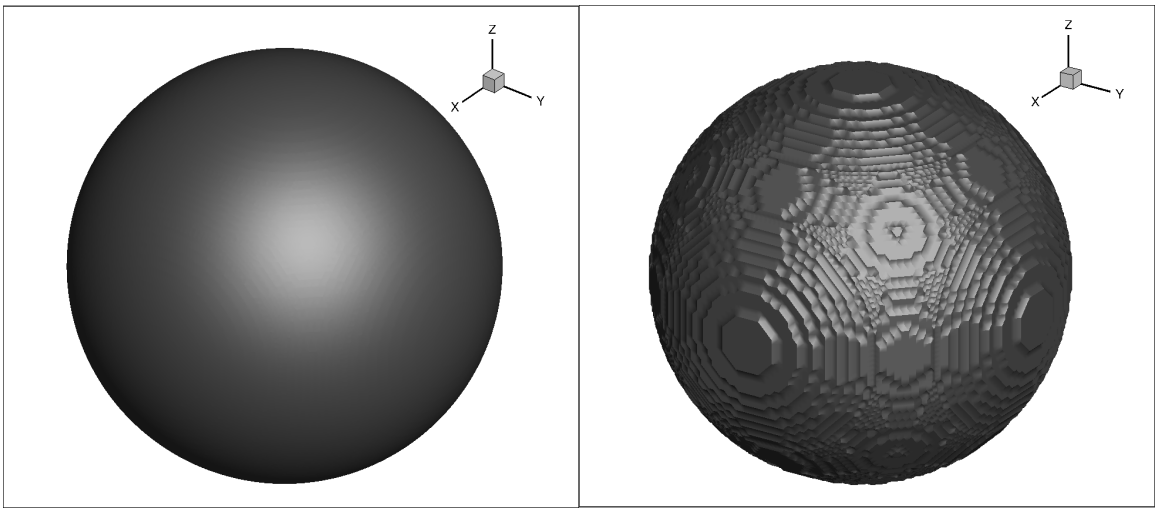

Figure A.4: Smooth vs blocky

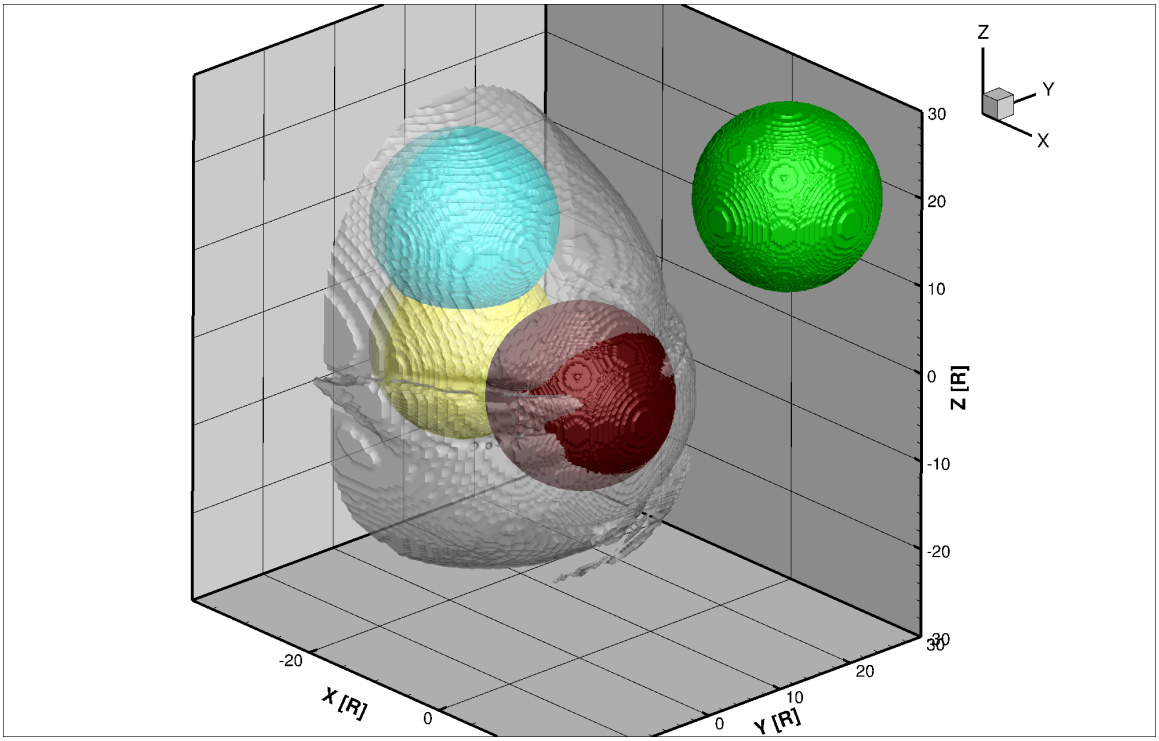

Figure A.5: Positions

Figure A.6: Concentric sphere setup: A.4 shows smooth vs blocky sphere. A.5 shows positions of spheres with Maroon:origin, Green:exterior, Yellow:tail,Cyan:lobe

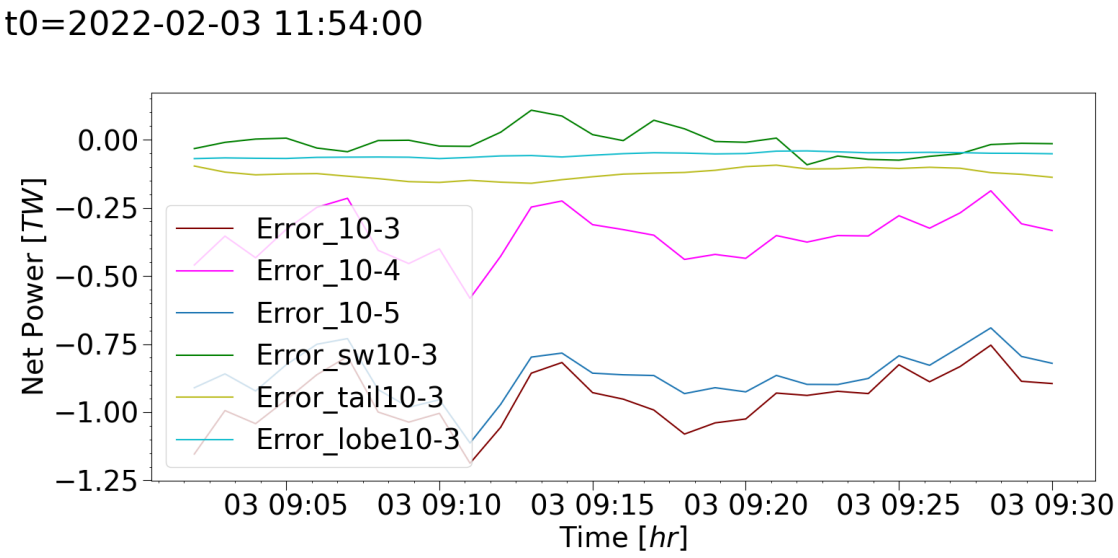

Figure A.7: Errors calculated for concentric sphere tests calculated as $dU/dt_{\text{flux}} - dU/dt_{\text{cDiff}}$. All errors have a negative bias indicating an over prediction except for the solar wind case that changes sign.

BIBLIOGRAPHY

BIBLIOGRAPHY

Akasofu, S.-I. (1981), Energy coupling between the solar wind and the magnetosphere, *Space Science Reviews*, *28*(2), 121–190, doi:10.1007/bf00218810.

Ala-Lahti, M., T. Pulkkinen, Y. Pfau-Kempf, M. Grandin, and M. Palmroth (2022), Energy flux through the magnetopause during flux transfer events in hybrid-Vlasov 2D simulations, *Geophysical Research Letters*, doi:10.1029/2022gl100079.

Axford, W. I., and C. O. Hines (1961), A UNIFYING THEORY OF HIGH-LATITUDE GEOPHYSICAL PHENOMENA AND GEOMAGNETIC STORMS, *Canadian Journal of Physics*, *39*(10), 936–967, doi:10.1139/p61-172.

Boardsen, S. A., T. E. Eastman, T. E. Eastman, T. Sotirelis, T. Sotirelis, J. C. James, and J. L. Green (2000), An empirical model of the high-latitude magnetopause, *Journal of Geophysical Research*, *105*, 23,193–23,219, doi:10.1029/1998ja000143.

Brenner, A., T. I. Pulkkinen, Q. Shidi, and G. Toth (2023), Dissecting Earth's Magnetosphere: 3D Energy Transport in a Simulation of a Real Storm Event.

Burton, R. K., R. L. McPherron, and C. T. Russell (1975), An empirical relationship between interplanetary conditions and Dst, *Journal of Geophysical Research*, *80*(31), 4204–4214, doi:10.1029/ja080i031p04204.

Carovillano, R. L., G. L. Siscoe, and G. Siscoe (1973), Energy and momentum theorems in magnetospheric processes, *Reviews of Geophysics*, *11*(2), 289–353, doi:10.1029/rg011i002p00289.

Carter, J. A., S. Milan, S. E. Milan, J. C. Coxon, M.-T. Walach, M. Walach, and B. J. Anderson (2016), Average field-aligned current configuration parameterized by solar wind conditions, *Journal of Geophysical Research*, *121*(2), 1294–1307, doi:10.1002/2015ja021567.

Chen, Y., et al. (2017), global three dimensional simulation of earth s dayside reconnection using a two way coupled magnetohydrodynamics with embedded particle in cell model initial results 3 d mhd epic simulation of magnetosphere, *Journal of Geophysical Research*, doi:10.1002/2017ja024186.

C.J. Pollock, et al. (), The Role and Contributions of Energetic Neutral Atom (ENA) Imaging in Magnetospheric Substorm Research, doi:10.1007/978-94-010-0027-7_8.

Crooker, N. U., N. U. Crooker, N. U. Crooker, J. Feynman, J. Feynman, and J. T. Gosling (1977), On the high correlation between long-term averages of solar wind speed and geomagnetic activity, *Journal of Geophysical Research*, *82*(13), 1933–1937, doi:10.1029/ja082i013p01933.

De Zeeuw, D. L., Darren L. De Zeeuw, S. Sazykin, R. A. Wolf, T. I. Gombosi, A. J. Ridley, and G. Toth (2004), Coupling of a global MHD code and an inner magnetospheric model: Initial results, *Journal of Geophysical Research*, *109*, doi:10.1029/2003ja010366.

Dessler, A. J., and E. N. Parker (1959), Hydromagnetic theory of geomagnetic storms, *Journal of Geophysical Research*, *64*(12), 2239–2252, doi:10.1029/jz064i012p02239.

Donald H. Fairfield, and D. H. Fairfield (1971), Average and unusual locations of the Earth's magnetopause and bow shock, *Journal of Geophysical Research*, *76*(28), 6700–6716, doi:10.1029/ja076i028p06700.

Dungey, J. W. (1961), Interplanetary Magnetic Field and the Auroral Zones, *Physical Review Letters*, *6*(2), 47–48, doi:10.1103/physrevlett.6.47.

Escoubet, C., J.M Bosqued, and J.-M. Bosqued (1989), The influence of IMF-Bz and/or AE on the polar cusp: An overview of observations from the AUREOL-3 satellite, *Planetary and Space Science*, *37*(5), 609–626, doi:10.1016/0032-0633(89)90100-1.

F. A. Staples, et al. (2020), Do statistical models capture the dynamics of the magnetopause during sudden magnetospheric compressions, *Journal of Geophysical Research*, *125*(4), doi:10.1029/2019ja027289.

FEMA (2019), 2019 National Threat and Hazard Identification and Risk Assessment (THIRA), *Tech. Rep. FEMA-2019-508c*, Federal Emergency Management Administration, Washington, DC.

Gjerloev, J. (2012), The SuperMAG data processing technique, *Journal of Geophysical Research*, *117*, doi:10.1029/2012ja017683.

Glocer, A., G. Toth, M.-C. Fok, T. I. Gombosi, and M. W. Liemohn (2009a), Integration of the radiation belt environment model into the space weather modeling framework, *Journal of Atmospheric and Solar-Terrestrial Physics*, *71*(16), 1653–1663, doi:10.1016/j.jastp.2009.01.003.

Glocer, A., G. Toth, Y. Ma, T. I. Gombosi, J. Zhang, and L. M. Kistler (2009b), Multifluid Block-Adaptive-Tree Solar Wind Roe-Type Upwind Scheme: Magnetospheric Composition and Dynamics During Geomagnetic Storms-Initial Results, *Journal of Geophysical Research*, *114*(12), doi:10.1029/2009ja014418.

Glocer, A., et al. (2020), A Case Study on the Origin of Near-Earth Plasma, *Journal of Geophysical Research*, *125*(11), doi:10.1029/2020ja028205.

Gombosi, T. I. (1998), *Physics of the Space Environment*, Cambridge University Press, Cabridge, UK.

Gombosi, T. I., et al. (2021), What sustained multi-disciplinary research can achieve: The space weather modeling framework, *Journal of Space Weather and Space Climate*, *11*, 42, doi:10.1051/swsc/2021020.

H. Zhang, J. Lu, and M. Wang (2023), Energy transfer across magnetopause under dawn–dusk IMFs, *Scientific Reports*, doi:10.1038/s41598-023-34082-2.

Hoilijoki, S., V. M. Souza, B. Walsh, P. Janhunen, and M. Palmroth (2014), Magnetopause reconnection and energy conversion as influenced by the dipole tilt and the IMF Bx, *Journal of Geophysical Research*, *119*(6), 4484–4494, doi:10.1002/2013ja019693.

J.-H. Shue, et al. (1998), Magnetopause location under extreme solar wind conditions, *Journal of Geophysical Research*, *103*, 17,691–17,700, doi:10.1029/98ja01103.

Kan, J. R., and L.-C. Lee (1979), Energy coupling function and solar wind-magnetosphere dynamo, *Geophysical Research Letters*, *6*(7), 577–580, doi:10.1029/gl006i007p00577.

Kovalick, T. (2023), Models and Regions of Geospace in the Satellite Situation Center Software, V. 2.2 (Hitchhiker's Guide to the SSC Geospace).

Kuznetsov, S. N., S. N. Kuznetsov, S. N. Kuznetsov, S. N. Kuznetsov, A. Suvorova, A. V. Suvorova, A. V. Suvorova, and A. V. Suvorova (1998), An Empirical Model of the Magnetopause for Broad Ranges of Solar Wind Pressure and BZ IMF, pp. 51–61, doi:10.1007/978-94-011-5214-3_5.

Laitinen, T. V., M. Palmroth, T. Pulkkinen, P. Janhunen, and H. Koskinen (2007), Continuous reconnection line and pressure-dependent energy conversion on the magnetopause in a global MHD model, *Journal of Geophysical Research*, *112*, doi:10.1029/2007ja012352.

Lavraud, B., B. Lavraud, and P. J. Cargill (2005a), Cluster reveals the magnetospheric cusps, *Astronomy & Geophysics*, *46*(1), doi:10.1046/j.1468-4004.2003.46132.x.

Lavraud, B., et al. (2005b), High-altitude cusp flow dependence on IMF orientation: A 3-year Cluster statistical study, *Journal of Geophysical Research*, *110*, doi:10.1029/2004ja010804.

Lin, R., et al. (2010), A three-dimensional asymmetric magnetopause model, *Journal of Geophysical Research*, *115*, doi:10.1029/2009ja014235.

Lorensen, W. E., and H. E. Cline (1987), Marching cubes: A high resolution 3D surface construction algorithm, *International Conference on Computer Graphics and Interactive Techniques*, *21*(4), 163–169, doi:10.1145/37401.37422.

Lu, J., H. X. Zhang, M. Wang, K. Kabin, Y. Zhou, and J. Y. Li (2021), Energy Transfer Across the Magnetopause Under Radial IMF Conditions, *The Astrophysical Journal*, *920*(1), 52, doi:10.3847/1538-4357/ac15f4.

Milan, S., et al. (2020), Dual-Lobe Reconnection and Horse-Collar Auroras, *Journal of Geophysical Research*, *125*(10), doi:10.1029/2020ja028567.

Mish, W. H., J. C. James, J. L. Green, M. G. Reph, M. Peredo, and M. Peredo (1995), ISTP science data systems and products, *Space Science Reviews*, *71*(1), 815–877, doi:10.1007/bf00751352.

Mukhopadhyay, A., D. T. Welling, M. W. Liemohn, A. J. Ridley, S. Chakraborty, and B. J. Anderson (2020), conductance model for extreme events impact of auroral conductance on space weather forecasts, *Social Work*, doi:10.1002/essoar.10503207.1.

Newell, P. T., T. Sotirelis, T. Sotirelis, K. Liou, C.-I. Meng, F. J. Rich, and F. J. Rich (2007), A nearly universal solar wind-magnetosphere coupling function inferred from 10 magnetospheric state variables, *Journal of Geophysical Research*, *112*, doi:10.1029/2006ja012015.

Palmroth, M., T. Pulkkinen, P. Janhunen, and C.-C. Wu (2003), Stormtime energy transfer in global MHD simulation, *Journal of Geophysical Research*, *108*, 1048, doi:10.1029/2002ja009446.

Palmroth, M., H. Koskinen, T. Pulkkinen, C.R. Anekallu, C. Anekallu, T. V. Laitinen, E. A. Lucek, and I. Dandouras (2011), Quantifying Energy Transfer at the Magnetopause, *3*, 29–37, doi:10.1007/978-94-007-0501-2_2.

Paul, A., B. Vaidya, and S. Strugarek (2022), A Volumetric Study of Flux Transfer Events at the Dayside Magnetopause, *The Astrophysical Journal*, *938*(2), 130–130, doi:10.3847/1538-4357/ac8eb5.

Perreault, P., and S.-I. Akasofu (1978), A study of geomagnetic storms, *Geophysical Journal International*, *54*(3), 547–573, doi:10.1111/j.1365-246x.1978.tb05494.x.

Petrinec, S. M., and C. T. Russell (1996), Near-Earth magnetotail shape and size as determined from the magnetopause flaring angle, *Journal of Geophysical Research*, *101*, 137–152, doi:10.1029/95ja02834.

Pitout, F., F. Pitout, Y. Bogdanova, and Y.V. Bogdanova (2021), The polar cusp seen by Cluster, *Journal of Geophysical Research*, *126*(9), doi:10.1029/2021ja029582.

Pudovkin, M. I., Bruno P. Besser, B. P. Besser, and S. A. Zaitseva (1998), Magnetopause stand-off distance in dependence on the magnetosheath and solar wind parameters, *Annales Geophysicae*, *16*(4), 388–396, doi:10.1007/s00585-998-0388-z.

Pulkkinen, A., et al. (2013), Community-wide validation of geospace model ground magnetic field perturbation predictions to support model transition to operations, *Space Weather-the International Journal of Research and Applications*, *11*(6), 369–385, doi:10.1002/swe.20056.

Pulkkinen, T., M. Palmroth, and T. V. Laitinen (2008), Energy as a tracer of magnetospheric processes: GUMICS-4 global MHD results and observations compared, *Journal of Atmospheric and Solar-Terrestrial Physics*, *70*(5), 687–707, doi:10.1016/j.jastp.2007.10.011.

Ridley, A. J., T. I. Gombosi, and D. L. DeZeeuw (2004), Ionospheric control of the magnetosphere: conductance, *Annales Geophysicae*, *22*(2), 567–584, doi:10.5194/angeo-22-567-2004.

Roelof, E. C., and D. G. Sibeck (1993), Magnetopause shape as a bivariate function of interplanetary magnetic field Bz and solar wind dynamic pressure, *Journal of Geophysical Research*, *98*, 21,421–21,450, doi:10.1029/93ja02362.

S. Chapman, S. Chapman, S. Chapman, and V. C. A. Ferraro (1930), A New Theory of Magnetic Storms, *Nature*, *126*(3169), 129–130, doi:10.1038/126129a0.

Samsonov, A., et al. (2016), Do we know the actual magnetopause position for typical solar wind conditions, *Journal of Geophysical Research*, *121*(7), 6493–6508, doi:10.1002/2016ja022471.

Sckopke, N. (1966), A general relation between the energy of trapped particles and the disturbance field near the Earth, *Journal of Geophysical Research*, *71*(13), 3125–3130, doi:10.1029/jz071i013p03125.

Scurry, L., and C. T. Russell (1991), Proxy studies of energy transfer to the magnetosphere, *Journal of Geophysical Research*, *96*(6), 9541–9548, doi:10.1029/91ja00569.

Shukhtina, M. A., and E. Gordeev (2015), In situ magnetotail magnetic flux calculation, *Annales Geophysicae*, *33*(6), 769–781, doi:10.5194/angeo-33-769-2015.

Stern, D. P. (1975), The motion of a proton in the equatorial magnetosphere, *Journal of Geophysical Research*, *80*(4), 595–599, doi:10.1029/ja080i004p00595.

Temerin, M. A., and X. Li (2006), Dst model for 1995–2002, *Journal of Geophysical Research*, *111*, doi:10.1029/2005ja011257.

Tenfjord, P., and N. Østgaard (2013), Energy Transfer and Flow in the Solar Wind-Magnetosphere-Ionosphere System: A New Coupling Function, doi:10.1002/jgra.50545.

Toffoletto, F., R. W. Spiro, R. A. Wolf, M. Hesse, and J. Birn (1996), Self-consistent modeling of inner magnetospheric convection.

Toth, G., et al. (2005), Space Weather Modeling Framework: A new tool for the space science community, *Journal of Geophysical Research*, *110*, doi:10.1029/2005ja011126.

Toth, G., et al. (2012), Adaptive numerical algorithms in space weather modeling, *Journal of Computational Physics*, *231*(3), 870–903, doi:10.1016/j.jcp.2011.02.006.

Vasyliunas, V. M., J. R. Kan, G. L. Siscoe, and S.-I. Akasofu (1982), Scaling relations governing magnetospheric energy transfer, *Planetary and Space Science*, *30*(4), 359–365, doi:10.1016/0032-0633(82)90041-1.

Vasyliūnas, V. M. (2006), Ionospheric and boundary contributions to the Dessler-Parker-Sckopke formula for Dst, *Annales Geophysicae*, *24*(3), 1085–1097, doi:10.5194/angeo-24-1085-2006.

Volland, H. (1973), A semiempirical model of large-scale magnetospheric electric fields, *Journal of Geophysical Research*, *78*(1), 171–180, doi:10.1029/ja078i001p00171.

Wang, C., J. Han, R. Schlickeiser, H. Li, Z. Peng, Z. Peng, and J. D. Richardson (2014), Solar wind-magnetosphere energy coupling function fitting: Results from a global MHD simulation, *Journal of Geophysical Research*, *119*(8), 6199–6212, doi:10.1002/2014ja019834.

Wang, Y., et al. (2013), A new three-dimensional magnetopause model with a support vector regression machine and a large database of multiple spacecraft observations, *Journal of Geophysical Research*, *118*(5), 2173–2184, doi:10.1002/jgra.50226.

Welling, D. T., and M. W. Liemohn (2014), Outflow in global magnetohydrodynamics as a function of a passive inner boundary source, *Journal of Geophysical Research*, *119*(4), 2691–2705, doi:10.1002/2013ja019374.

Wygant, J. R., R. B. Torbert, and F. S. Mozer (1983), Comparison of S3-3 polar cap potential drops with the interplanetary magnetic field and models of magnetopause reconnection, *Journal of Geophysical Research*, *88*, 5727–5735, doi:10.1029/ja088ia07p05727.

Xu, S., M. W. Liemohn, C. Dong, D. L. Mitchell, S. W. Bougher, and Y. Ma (2016), Pressure and ion composition boundaries at Mars, *Journal of Geophysical Research*, *121*(7), 6417–6429, doi:10.1002/2016ja022644.

Zhang, Y., L. J. Paxton, R. K. Schaefer, and W. H. Swartz (2022), Thermospheric Conditions Associated With the Loss of 40 Starlink Satellites, *Space Weather-the International Journal of Research and Applications*, *20*(10), doi:10.1029/2022sw003168.